Ab initio investigation of structural and electronic properties on 1D and 2D nanomaterials

Wenwen Cui

▶ **To cite this version:**

Wenwen Cui. Ab initio investigation of structural and electronic properties on 1D and 2D nanomaterials. Material chemistry. Université de Lyon, 2017. English. NNT : 2017LYSE1111 . tel-01592819

HAL Id: tel-01592819
https://theses.hal.science/tel-01592819

Submitted on 25 Sep 2017

HAL is a multi-disciplinary open access archive for the deposit and dissemination of scientific research documents, whether they are published or not. The documents may come from teaching and research institutions in France or abroad, or from public or private research centers.

L'archive ouverte pluridisciplinaire **HAL**, est destinée au dépôt et à la diffusion de documents scientifiques de niveau recherche, publiés ou non, émanant des établissements d'enseignement et de recherche français ou étrangers, des laboratoires publics ou privés.

N° d'ordre NNT : 2017LYSE1111

THÈSE DE DOCTORAT DE L'UNIVERSITÉ DE LYON
opérée au sein de
l'Université Claude Bernard Lyon 1

École Doctorale ED52
Physique et d'Astrophysique de Lyon

Spécialité de doctorat :
Discipline : Physique

Soutenue publiquement le 07/07/2017, par :
Wenwen CUI

Ab initio investigation of structural and electronic properties on 1D and 2D nanomaterials

---

Devant le jury composé de :

JOURNET-GAUTIER Catherine, Professeur, Université Claude Bernard Lyon 1	Présidente
DAPPE Yannick, CR CNRS HDR, Service de Physique de l'Etat Condense	Rapporteur
RADESCU Silvana, Professeur, Universidad de la Laguna	Rapporteure
BOTTI Silvana, Professeur, Friedrich-Schiller University of Jena	Examinatrice
NIQUET Yann-Michel, Chercheur HDR, Commissariat d'Energie Atomique	Examinateur
JOLY Laurent, Maître de Conférences HDR, Université Claude Bernard Lyon 1	Examinateur
MARQUES Miguel, Professeur, Martin-Luther-Universität	Co-directeur de thèse
SAN MIGUEL Alfonso, Professeur, Université Claude Bernard Lyon 1	Directeur de thèse

Abstract

In this thesis we mainly use the density functional tight-binding method (DFTB) to investigate the effect of high pressure on carbon nanotubes (CNTs). We start by investigating the collapse behavior of individualized CNTs, either empty or filled with water and carbon dioxide molecules. Then we study the collapse process of bundled few-wall (double, triple wall) carbon nanotues as the function of pressure, combining theoretical and experimental studies. Afterwards, we investigate the electronic and magnetic properties of a monolayer MoS_2 on the Ni(111) surface accounting for van der Waals interactions in the frame work of the density functional theory (DFT). The manuscript is structured in 7 chapters and the following paragraphs summarize the content by chapter of this document.

Chapter 1 is our introduction of this thesis, including the motivation and background of our topic as well as our important findings and results.

Chapter 2 introduces the main concepts and definitions of CNTs. Then we describe the electronic properties of CNTs as well graphene as a comparison. We also present a brief bibliographic review over high pressure physics applied to CNTs.

Chapter 3 consists of the theoretical framework used for our study. Firstly, a short introduction of Density Functional Theory (DFT) is presented. Next we list two mainly used exchange-correlation functions in DFT, then followed by an overview of van der waals functions which normal DFT cannot account for. Finally, we briefly introduces the Density Functional Tight-Binding method (DFTB) which we use for our CNTs modeling simulation.

In chapter 4, we present simulations of the collapse under hydrostatic pressure of carbon nanotubes containing either water or carbon dioxide. We show that the molecules inside the tube alter the dynamics of the collapse process, providing either mechanical support and increasing the collapse pressure, or reducing mechanical stability. At the same time the nanotube acts as a nanoanvil, and the confinement leads to the nanostructuring of the molecules inside the collapsed tube. In this way, depending on the pressure and on the concentration of water or carbon dioxide inside the nanotube, we observe the formation of 1D molecular chains, 2D nanoribbons, and even molecular single and multi-wall nanotubes. The structure of the encapsulated molecules correlates with the mechanical response of the nanotube, opening opportunities for the development of new devices or composite materials.

Our analysis is quite general and it can be extended to other molecules in carbon nanotube nanoanvils, providing a strategy to obtain a variety of nano-objects with controlled features cells. For the perfect empty CNTs, collapse behavior theoretically is barely affected by the pressure transmitting medium (PTM) environment under high pressure but only mainly is determined by the CNTs diameter. Our simulation using DFTB method gives good agreement both for the d dependence predicted by continuum mechanics models and for the deviation at small d which is at least partly due to the atomistic nature of the carbon nanotubes. The bending stiffness D of graphene sheet is determined to be $D = 1.7 \pm 0.1$ eV.

In chapter 5, we present a theoretical study of the collapse process of single-, double- and triple-wall CNTs as a function of pressure. Our theoretical simulations were performed using DFTB for inner tube diameters ranging from 0.6 nm to 3.3 nm. When the walls are separated by the graphitic distance, we show that the radial collapse pressure, P_c, is mainly determined by the diameter of the innermost tube, d_{in} and that its value significantly deviates from the usual $P_c \propto d_{\text{in}}^{-3}$ Lévy-Carrier law. A modified expression, $P_c d_{\text{in}}^3 = \alpha(1 - \beta^2/d_{\text{in}}^2)$ with α and β numerical parameters, which reduces the collapse pressure for low diameters is proposed. For $d_{\text{in}} \gtrsim 1.5$ nm a further enhanced stability is found which may be assigned to the intertube interactions of deformed tubes. If the inner and outer tubes are separated by a larger distance, the collapse process is more complex, exhibiting different regimes as a function of pressure.

In chapter 6 we investigate the electronic and magnetic properties of a monolayer of MoS_2 deposited on a Ni(111) surface using DFT method. Accounting for van der Waals interactions is found to be essential to stabilize the chemisorbed MoS_2 monolayer. The interface is metallic due to Mo d states positioned at the Fermi energy, with a Schottky barrier of 0.3 eV and a high tunneling probability for electrons. Small magnetic moments are induced on Mo and S atoms, while we measure a significant demagnetization of the Ni layer at the interface.

Finally the last chapter synthesizes the main results of this work presenting also some perspectives.

Résumé

Le sujet principal de cette thèse est l'utilisation de la Théorie Fonctionnelle de la Densité dans sa variante à liaisons fortes (DFTB) pour l'étude de l'effet de la pression sur des nanotubes de carbone. Nous commençons par étudier l'effondrement radial sous l'effet de la pression de nanotubes de carbone (CNTs) individualisés, soit dans leur forme originale (vides), soit remplis avec des molécules d'eau ou de dioxyde de carbone. Nous étudions à continuation le processus d'effondrement radial de fagots de nanotubes de carbone a faible nombre de parois (double ou triple-parois) en fonction de la pression combinant modélisations et études expérimentales. Finalement nous présentons une étude sur les propriétés électroniques et magnétiques d'une monocouche de MoS_2 déposée sur une surface de Ni (111) dans le cadre de la Théorie Fonctionnelle de la Densité incluant des interactions de van der Waals. Le manuscrit est structuré en 7 chapitres. Les paragraphes qui suivent résument le contenu de chacun d'entre eux.

Le chapitre 1 est notre introduction à cette thèse, incluant les motivations, les connaissances préalables sur nos sujets que nous intéressent ici, ainsi que notre contribution et principaux résultats.

Le chapitre 2 présente les principaux éléments et définitions sur les CNTs. Nous décrivons ensuite les propriétés électroniques des CNTs et celles du graphène qui constitue un système de référence. Nous présentons également une brève revue bibliographique sur la physique à haute pression des nanotubes de carbone.

Le chapitre 3 contient les éléments théoriques de notre étude. D'abord nous faisons une courte introduction à la Théorie Fonctionnelle de la Densité (DFT). Ensuite nous présentons deux des fonctions d'échange-corrélation les plus utilisées, suivi d'une revue sur les fonctions de van der Waals dont la DFT ordinaire ne peut rendre compte. Finalement, nous faisons une brève introduction à la méthode DFTB que nous utilisons dans nos modélisations des CNTs.

Dans le chapitre 4 nous présentons nos modélisations sur l'effondrement radial sous pression hydrostatique de nanotubes de carbone contenant soit de l'eau doit du dioxyde de carbone. Nous montrons que la présence de ces molécules à l'intérieur des tubes modifie la dynamique du processus d'effondrement radial, donnant lieu soit à un support mécanique et repoussant la pression d'effondrement radial soit réduisant leur stabilité mécanique. Au

même temps, le nanotube agit comme une nano-enclume et le confinement conduit à une nanostructuration des molécules à l'intérieur du tube effondré. De cette manière, suivant la pression appliquée et la concentration à l'intérieur du tube d'eau ou de dioxyde de carbone, nous observons la formation de chaines moléculaires 1D, des rubans 2D et même des nanotubes moléculaires mono- ou multi-parois. La structure des systèmes moléculaires encapsulés est corrélée avec la réponse mécanique des nanotubes de carbone, ouvrant des opportunités de développement des nouveaux composants ou des matériaux composites à base de nanotubes de carbone.

Notre analyse est générale et peut être étendue à d'autres molécules encapsulées dans des nano-enclumes à base de nanotubes de carbone ouvrant la possibilité au développement d'une stratégie pour l'obtention d'une variété de nouveaux nano-objets avec des cellules caractéristiques contrôlées. Pour les CNTs vides, l'effondrement radial est très peu affecté par la nature du milieu transmetteur de pression, mais déterminé par le diamètre des nanotubes de carbone. Nos modélisations avec la méthode DFTB sont en excellent accord avec les modèles de milieux continues sur la dépendance de la pression d'effondrement radial avec le diamètre du tube, d, mais montrent également une déviation de ce modèle pour les petites valeurs de d, ce qui est dû au moins en partie à la nature atomistique des nanotubes de carbone. Nous avons obtenu une valeur du module de flexion du graphène, D, de $D = 1.7 \pm 0.1$ eV .

Dans le chapitre 5, nous présentons une étude théorique de l'effondrement radial en fonction de la pression pour des nanotubes de carbone à parois simple, double et triple. Nos modélisations sont réalisées par DFTB pour des diamètres internes allant de 0.6 à 3.3 nm. Quand les parois sont séparées par la distance graphitique, nous montrons que la pression d'effondrement radial, P_c, est déterminé par le diamètre du tube interne, d_{in}, mais avec un important écart par rapport à une loi à la Lévy-Carrier, $P_c \propto d_{\mathrm{in}}^{-3}$. Nous proposons une expression modifiée, $P_c d_{\mathrm{in}}^3 = \alpha(1-\beta^2/d_{\mathrm{in}}^2)$ où α et β sont des paramètres numériques. Cette expression modifiée donne lieu à une réduction de la pression d'effondrement radiale pour les petits diamètres. Pour din supérieurs à environ 1.5 nm, un effet de stabilisation structural supplémentaire est obtenu qui peut être attribué à l'interaction entre nanotubes déformés. Si les nanotubes interne et externe sont séparés par une distance plus importante, le processus d'effondrement radial est plus complexe, présentant différent régimes en fonction de la pression.

Dans le chapitre 6 nous étudions par DFT les propriétés électroniques et magnétiques d'une monocouche de MoS_2 déposée sur une surface de Ni (111). La prise en compte des interactions de van der Waals s'est avérée essentielle afin de stabiliser la monocouche de MoS_2. L'interface est métallique en raison de la présence sur le niveau de Fermi d'états d du Mo. Elle présente une barrière Schottky de 0.3 eV et une probabilité tunnel pour les électrons

élevée. Des faibles moments magnétiques sont introduits sur les atomes de molybdène et de soufre, tandis que nous observons une démagnétisation significative sur la couche de nickel à l'interface.

Enfin le dernier chapitre constitue une synthèse des derniers résultats et la présentation de quelques perspectives.

Contents

Chapter 1

Introduction

Carbon has many allotropes due to its ability to form *sp*-, sp^2- and sp^3- hybridized bonds. It can either form soft opaque graphite or hard transparent diamond. In addition to these and other "macro"-scopic carbon materials, several "nano"-carbon materials have been discovered in the past few decades, opening new paths for novel materials exploration. It all started with C_{60} molecule (fullerene), which was synthesized for the first time in 1985 by Richard Smalley [1], followed by the observation of carbon nanotubes (CNTs) by Iijima in 1991 [2], and two-dimensional graphene by Geim and Novoslov [3] in 2004. Among the three types of nanocarbon materials, CNTs attract great attention from both industry and academia. One of the reasons why CNTs are so popular is due to their excellent mechanical properties. They are considered the strongest and stiffest material on earth. For example, the Young's modulus of CNTs is estimated in the terapascal range [4] along the axial direction, however CNTs are also known to have a remarkable flexibility in their radial direction. These properties offer high potential for many kinds of applications, such as reinforcement of composite materials, fabrication of nano-optomechanical systems and so on. It has been widely accepted that the mechanical deformation of CNTs can lead to considerable changes in electric, optical, and chemical properties. Nevertheless, a complete understanding of their mechanical behavior is still lacking, limiting the design and application of CNT-enhanced materials [5].

Another important application of CNTs is to use them as host vessels for biology and chemistry to achieve nano-confinement, thanks to their hollow and cylindrical structure at the nanoscale. The application of CNTs for nano-confinement creates possibilities for new devices, including membranes [6], nanofludic [7] and thermophoretic channels [8]. Filler inside CNTs can be for instance argon [9], polyiodides [10], C_{70} (peapods) [11], C_{60} [12–14], water [15–17], or even other nanotubes [18, 19]. Generally, the filling effect is two-fold: On the one hand, behavior and properties of guest compounds can differ significantly from bulk

matter [20–22] due to strong nano-confinement effect. On the other hand, guest molecules can also influence the electronic and mechanical properties [14, 15, 23].

It is well known that pressure can significantly influence the properties and stability of materials. Specifically, pressure can drive CNTs to undergo radial transformation from circular to ovalization, and even collapse (the ultimate configuration) [24]. Furthermore, this kind of structural deformation is thought to narrow the band gap, leading to nanotubes that behave as metals or semimetals [25]. Thus, one of the goals for this thesis is to investigate the high pressure effect on the stability of single wall carbon nanotubes (SWCNTs) in different hydrostatic pressure transmitting medium (PTM). At the same time, the nano-confinement effect is also studied when the PTM enters the CNTs as a "foreigner molecule". For this purpose, SWCNTs, either empty or filled with water, carbon dioxide and argon, were used to investigate the role of filling and environment on the pressure stability. Double wall carbon nanotubes (DWCNTs) viewed as a SWCNT filled with another single-wall tube were also prepared and simulated, to compare the results with those of the SWCNTs.

Besides the above mentioned one dimensional nanostructures, two dimensional (2D) layered materials also ignited intensive interest, as well as prospects for technological breakthroughs in many diverse applications since the observation of graphene in 2004 [3]. These emerging 2D materials and their heterostructures offer tremendous opportunities in the exploration of fundamental condensed matter phenomena and the development of novel technologies [26]. Especially, the past few years have seen the rapid development of 2D materials research focusing on the family of transition metal dichalcogenides (TMDs), such as MoS_2 [27, 28]. The weak van der Waals interactions between neighboring layers allow much more flexible integration of different materials without the limitation of lattice matching, and facilitate the isolation of individual layers by exfoliation or vapor deposition methods [29, 30]. The isolation of a monolayer (ML) causes dramatic changes in material properties compared with those of the bulk counterpart, due to the confinement of charge carriers in two dimensions (x- and y- directions) and the absence of interaction in the z- direction. For example, the bulk indirect bandgap of MoS_2 ($\sim$1.2 eV) can be tuned into the monolayer direct bandgap after isolation. Moreover, compared with zero-bandgap graphene and the large indirect bandgap hexagonal BN sheet ($\sim$ 6 eV), ML MoS_2 nanosheets are more promising candidates for applications in various domains, such as electronics, photonics or spintronic devices, due to their direct bandgap of around 1.9 eV [27], their high quantum efficiency [28] and good electron mobilities [31]. In a real device, semiconducting 2D MoS_2 needs a contact with metal electrodes, and a Schottky barrier is often formed on semiconductor-metal interfaces, hindering the transport of charge and spin carrier. Thus another goal of this thesis is to find low-resistance metal contacts with MoS_2, which can have at the same time a potential for

spintronic applications. In this context, Ni, a room-temperature ferromagnetic metal was chosen as the most promising candidate for high-temperature spintronics devices made of TMD. This thesis, with the above discussed goals, is organized as follows:

Chapter 2 presents basic concepts on CNTs, including the electronic properties of graphene and how it relates to the electronic properties of CNTs. It also presents a bibliographic review on high pressure physics applied to carbon nanotubes. The third chapter gives an introduction to the theoretical framework used for the present study. DFT method is firstly described, then followed by an overview of van der Waals functionals in DFT. Finally, we discuss the Density Functional Tight-Binding method (DFTB), which we mainly used for CNTs theoretical simulations. Chapter 4 analyzes and discusses in detail the important findings of the present work on the effect of the inner filler on the mechanical stability of SWCNTs under pressure. Combining experimental and theoretical results, the radial stability of double and triple wall CNTs under pressure is presented in chapter 5. Chapter 6 presents the magnetism and contact properties of ML MoS_2 deposited on a Ni(111) surface. Finally, Chapter 7 gives a brief summary of the most import findings of this thesis and a perspective on future work.

Chapter 2

Carbon nanotubes under high-pressure

This chapter mainly introduces some historical background and the physics of carbon nanotubes (CNTs) under pressure. It also presents how to calculate the electronic properties of CNTs using a tight binding approach.

2.1 Carbon nanotubes

CNTs are unique nanostructures characterized by a cylindrical geometry with a nanoscale diameter. They can be viewed as rolled graphene sheets. They can also be assimilated as elements of the fullerene structure family: in fact, CNTs are also called cylindrical fullerenes. While the fullerene molecule, buckminsterfullerene C_{60} (Fig. 2.1 (a)) was first discovered by Richard Smalley in 1985 [1], the first observation of multi-wall CNTs was reported by Sumio Iijima in 1991 [2] (Fig. 2.1 (b)). Two years later, his group [32] discovered experimentally also the important single wall carbon nanotube structure (SWCNT), which opened the way to extensive theoretical and experimental studies. Theory predicted [33, 34] that CNTs can be metallic or semiconducting depending on the details of the tube structure, characterized by its chirality. In 1998 this prediction was finally confirmed by experiments [35, 36].

In the following, we will provide a brief introduction to the structural and electrical properties of CNTs.

From the early study with transmission electron microscopy (TEM) and scanning tunneling microscopy (STM) techniques [37], CNTs were viewed as the result of rolling up a single honeycomb layer of crystalline graphite, i.e. a graphene sheet (Fig. 2.3 (c)). Graphene is a two-dimensional carbon structure, where carbon atoms are arranged on a honeycomb network (Fig. 2.3 (a)). Fig. 2.2 (a) shows the Bravais lattice of graphene which is spanned by the two lattice vectors, $\mathbf{a}_1$ and $\mathbf{a}_2$, with a basis of two atoms per unit cell. The basis vectors ($\mathbf{a}_1$, $\mathbf{a}_2$) (see Fig. 2.2) have the same length $a_0 = \sqrt{3}b$, where b is the carbon-carbon bond

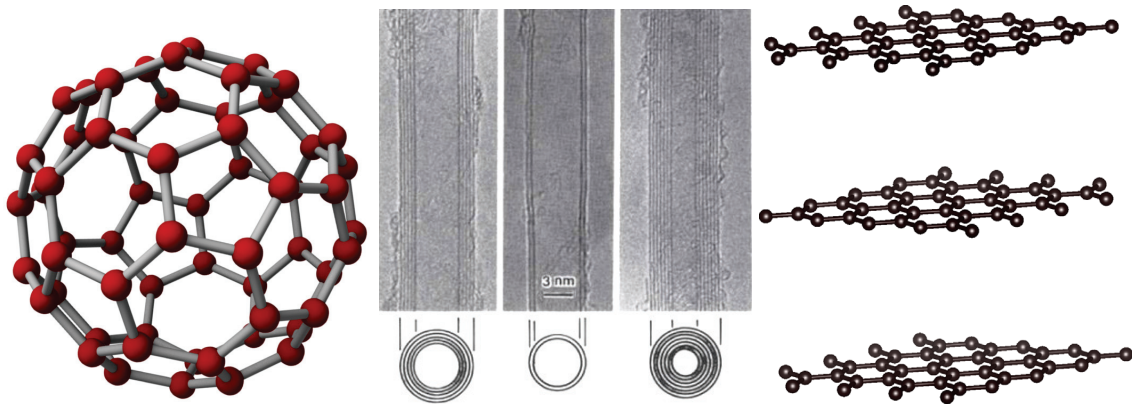

(a) (b) (c)

Figure 2.1 (a) fullerene C_{60}. (b) The first observation by TEM of multi-wall coaxial nanotubes by Iijima in 1991 [2]. (c) graphite structure.

length (1.42 Å). The way in which the graphene sheet is rolled up is described by the vector $\mathbf{C}_h$ and $\mathbf{T}$ in Fig. 2.3 (a).

The circumference of any carbon nanotube can be represented by the chiral vector $\mathbf{C}_h$ using a pair of indices (n,m), $\mathbf{C}_h = n\ \mathbf{a}_1 + m\ \mathbf{a}_2$, where $\mathbf{a}_1$ and $\mathbf{a}_2$ are the unit vectors of the hexagonal honeycomb lattice. (n,m) are called the chiral indexes. Fig. 2.3 (a) shows the chiral angle θ between the chiral vector $\mathbf{C}_h$ and $\mathbf{a}_1$. In the regular Cartesian coordinate system (x,y), $\mathbf{a}_1$ and $\mathbf{a}_2$ are respectively:

$$\mathbf{a_1} = \frac{a_0}{2}\begin{pmatrix}\sqrt{3}\\1\end{pmatrix}, \qquad \mathbf{a_2} = \frac{a_0}{2}\begin{pmatrix}\sqrt{3}\\-1\end{pmatrix} \tag{2.1}$$

and the corresponding reciprocal space vectors (Fig. 2.2 (b)) are $\mathbf{b}_1$ and $\mathbf{b}_2$ (with respect to the coordinate system (K_x,K_y)) which can be written respectively as:

$$\mathbf{b_1} = \frac{2\pi}{a_0}\begin{pmatrix}\frac{1}{\sqrt{3}}\\1\end{pmatrix}, \qquad \mathbf{b_2} = \frac{2\pi}{a_0}\begin{pmatrix}\frac{1}{\sqrt{3}}\\-1\end{pmatrix} \tag{2.2}$$

The lattice vectors respect the condition:

$$\begin{cases}\mathbf{a}_i \cdot \mathbf{b}_j = 2\pi\delta_{ij} \qquad i,j = 1,2\\ A_g \cdot B_g = (2\pi)^2\end{cases} \tag{2.3}$$

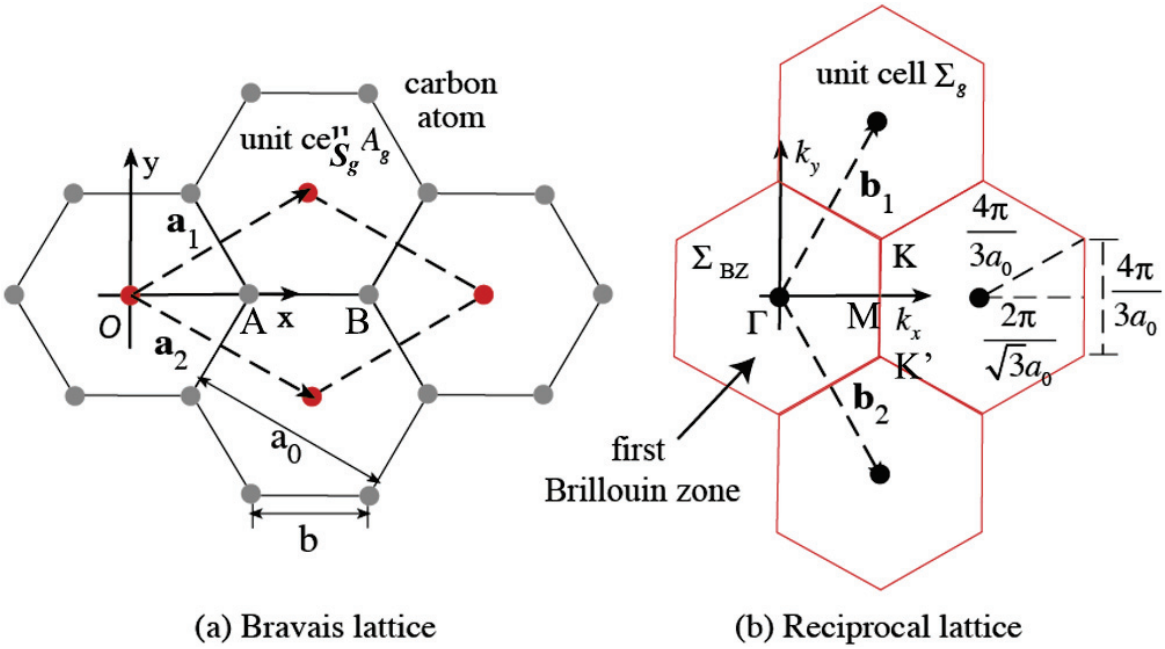

Figure 2.2 The crystal lattice of graphene. (a) Bravais lattice; (b) Reciprocal lattice

where A_g and B_g are the area of of the real and reciprocal unit cell, respectively. The nanotube diameter d_t and the chiral angle θ are given by

$$\begin{aligned} d_t &= \frac{|C_h|}{\pi} = \frac{\sqrt{a_0(m^2+mn+n^2)}}{\pi} \\ \theta &= tan^{-1}[\frac{\sqrt{3}n}{2m+n}] \end{aligned} \tag{2.4}$$

According to the value of θ, three categories of CNTs (see Fig. 2.3 and Fig. 2.5) can be defined:

(1) zigzag nanotubes $(n,0)$ $(\theta = 0^\circ)$;

(2) armchair nanotubes (n,n) $(\theta = 30^\circ$ or $n = m)$;

(3) chiral nanotubes (n,m) with $n > m > 0$ $(0 \leq \theta \leq 30^\circ)$;

Both zigzag and armchair nanotubes can be considered as achiral because of their mirror symmetry. In Fig. 2.3 (a), we have indicated another vector $\mathbf{T}$, called translation vector, defined as the shortest repeat distance along the tube axis, normal to $\mathbf{C}_h$:

$$\mathbf{T} = t_1\mathbf{a_1} + t_2\mathbf{a_2} \tag{2.5}$$

The rectangle defined by the vectors $\mathbf{C}_h$ and $\mathbf{T}$ represents the unit cell of the CNT. From the condition:

$$\mathbf{C_h} \cdot \mathbf{T} = 0 \tag{2.6}$$

we obtain

$$t_1 = \frac{2m+n}{d_R}, \qquad t_2 = -\frac{2n+m}{d_R} \tag{2.7}$$

and

$$|\mathbf{T}| = \frac{a_0\sqrt{3(n^2+nm+m^2)}}{d_R} \tag{2.8}$$

here, d_R is the greatest common divisor of $(2n+m)$ and $(2m+n)$ which is given by

$$d_R = \begin{cases} d, & \text{if} \quad n-m \quad \text{is not a multiple of } 3d \\ 3d, & \text{if} \quad n-m \quad \text{is a multiple of } 3d \end{cases} \tag{2.9}$$

We can also calculate the number of hexagons N, per unit cell of a chiral nanotube . First, the area A_g of the primitive unit cell can be easily obtained:

$$\begin{aligned} A_g &= |\mathbf{a_1} \times \mathbf{a_2}| \\ &= a_0^2 sin(\frac{\pi}{3}) = 0.05245 nm^2 \end{aligned} \tag{2.10}$$

Then, as we know the primitive unit cell contains two carbon atoms, we obtain

$$N = \frac{|\mathbf{C_h} \times \mathbf{T}|}{|\mathbf{a_1} \times \mathbf{a_2}|} = \frac{2(n^2+mn+mn)}{d_R} \tag{2.11}$$

Fig. 2.4 gives another classification according to the result of of $mod(n-m,3)$. We will discuss later how (n,m) correlates with the electronic properties of the CNTs (metal or semiconductor).

For completeness, it should be mentioned that the CNTs do not only exist SWCNTs but also come in other species as ropes of multi-wall carbon nanotube (MWCNTs), which consist of multiple rolled layers of graphene. According to the number of graphene layers, we distinguish double wall carbon nanotubes (DWCNTs) (two concentric carbon nanotubes), triple wall (TWCNTs), and quadruple (QWNTs) wall carbon nanotubes (see Fig. 2.6), and so on. In certain respects, MWCNTs are similar to SWCNT, but they also have their own characteristics. The interlayer distance in multi-walled nanotubes is in general close to the distance between graphene layers in graphite, approximately 3.4 Å. Compared with SWCNTs,

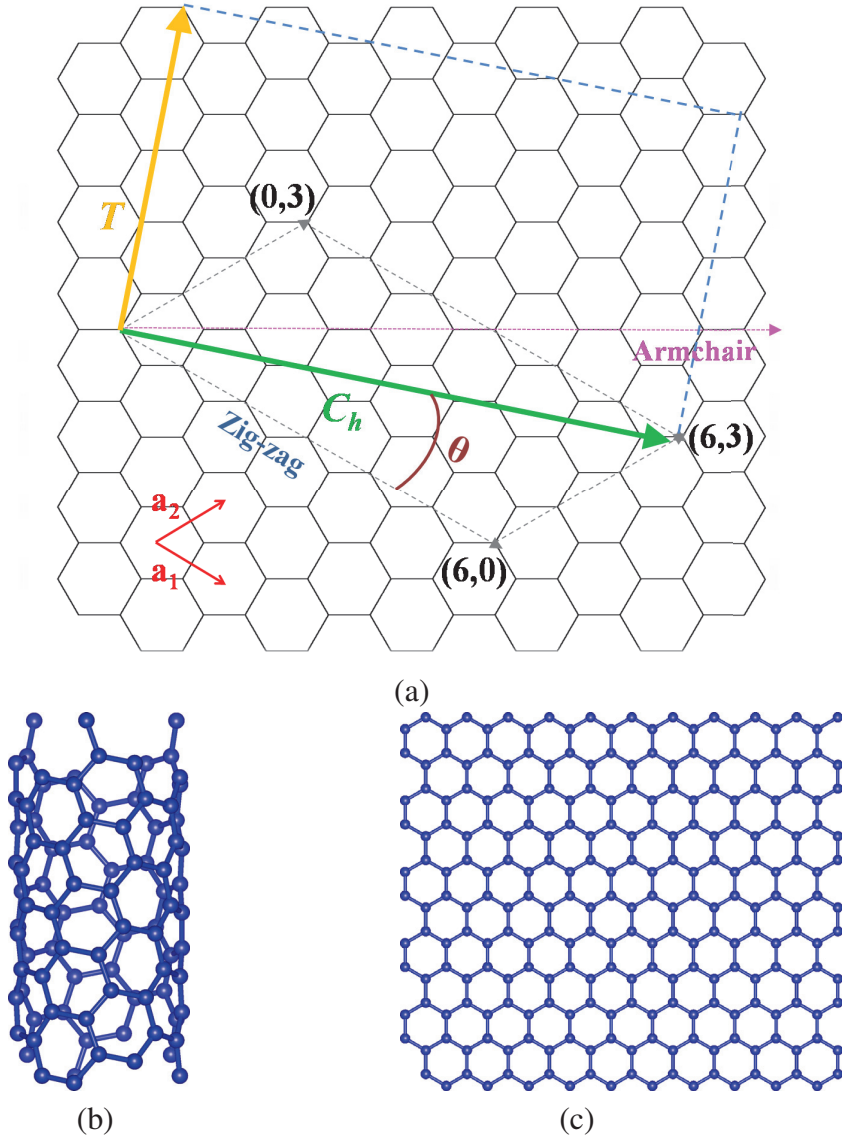

Figure 2.3 (a) The rolling up from the honeycomb lattice to build the (6,3) SWCNT. $\mathbf{C}_h$ and $\mathbf{T}$ are the chiral and the translation vectors of the SWCNT, respectively. The chiral angle θ is defined as the angle between $\mathbf{C}_h$ and the $\mathbf{a}_1$ vector, which defines the zigzag (n,0) direction. (b) The unit cell of the (6,3) CNT. (c) A layer of graphite (graphene).

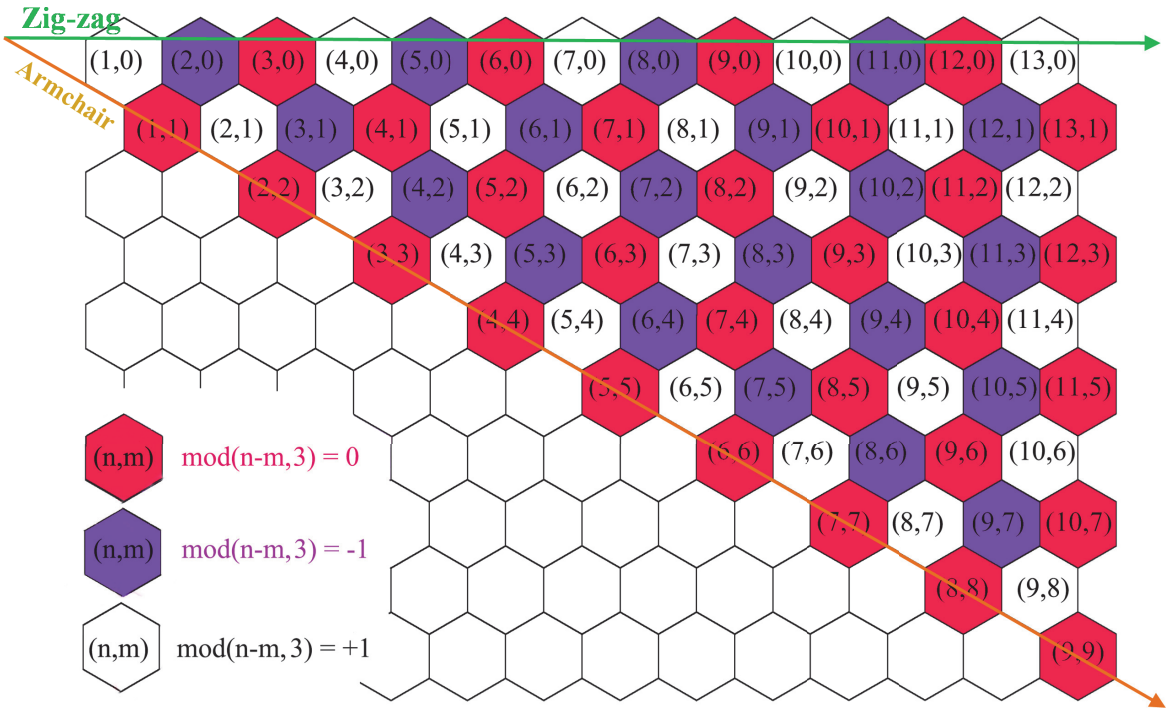

Figure 2.4 Chiral vectors of general carbon nanotubes, including zigzag, armchair, and chiral nanotubes specified by pair indices (n,m). Colored hexagons represent different results of mod(n-m,3).

MWCNTs can have in some respects improved properties that make them specifically interesting for the industry:

• High electrical conductivity (like copper). It is worth to note that only the outer-wall conduction is relevant and the inner walls are not instrumental to conductivity.

• Large mechanical strength. Defect-free, individual MWNTs have an excellent tensile strength and are easier to produce than SWCNTs.

2.2 Electronic properties of graphene

The electronic properties of CNTs can be in first approximation deduced from those of graphene by mapping the band structure of the 2D hexagonal lattice onto a cylinder. It is hense necessary to introduce the band structure of graphene first.

In the 2D hexagonal lattice, every carbon atom has three nearest neighbors and four valence orbitals ($2s$, $2p_x$, $2p_y$ and $2p_z$). The first three valence states are hybridized to form the sp^2 σ bonds with adjacent carbon atoms constructing the skeleton of the local structure, while the fourth state ($2p_z$) gives origin to the π band, which is oriented perpendicularly to the plane of the graphene lattice. The π band cannot couple with σ/σ^* states due to

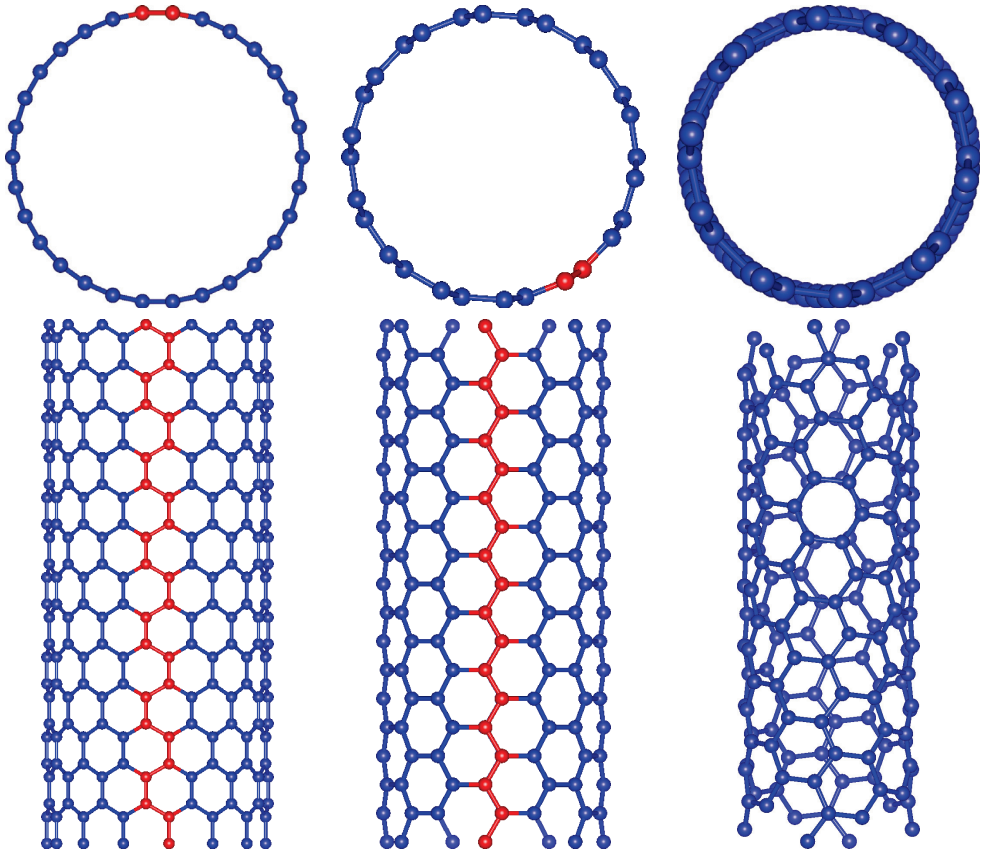

Figure 2.5 Chirality of SWCNTs (a) armchair (7,7) (b) zigzag (15,0) (c) chiral (6,4). The red line corresponds to the rolling axis of armchair and zigzag in Fig. 2.4.

symmetry. Interactions between neighboring p_z orbitals are strong and create a manifold of delocalized π/π^* orbitals in the planes above and below the atomic sheet. The delocalized π states form the highest occupied valence band at the Fermi level. The π and π^* states are degenerated at Brillouin zone corners points K. The π/π^* states close to the Fermi energy are dominant to conducting band, in contrast, the σ/σ^* bands are far from the Fermi energy and contribute little to conduction. Fig. 2.7 (a) shows the band structure of an ideal graphene layer according to a tight-binding model which includes 2 pairs of σ and σ^* bands, and one pair of π and π^* bands. Fig. 2.7 (c) shows the energy spectrum of graphene and zoom-in of the energy bands at the highlighted points of K and K'.

The Brillouin zone of graphene is shown in Fig. 2.2 (b), and presents a hexagonal structure with two nonequivalent K and K' points at the corner of the Wigner-Seitz cell. The first Brillouin zone is defined by the high symmetry Γ, K, and M as the center, the corner, and the center of the edge, respectively. The two corners points K and K' are of particular interest for

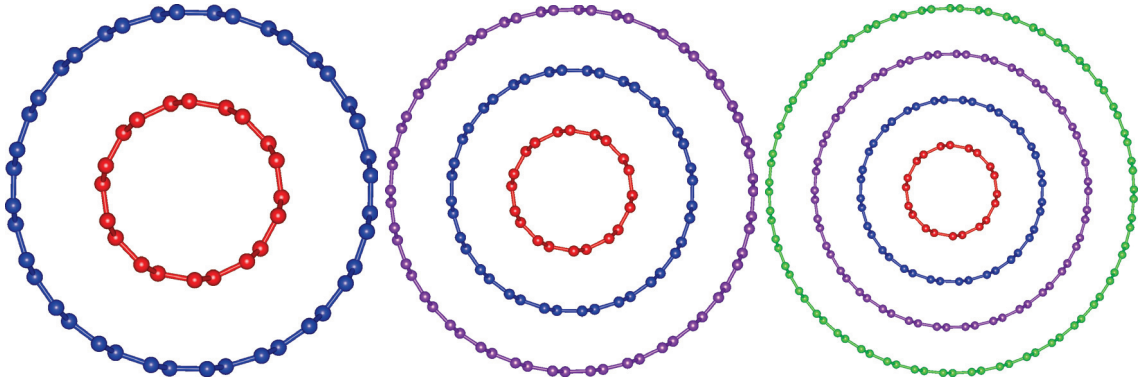

(a) (b) (c)

Figure 2.6 Example of multiple wall carbon nanotubes (a) DWCNT (5,5)@ (10,10) (b) TWCNT (5,5)@ (10,10)@ (15,15) (c) QWCNT (5,5)@ (10,10)@ (15,15)@ (20,20)

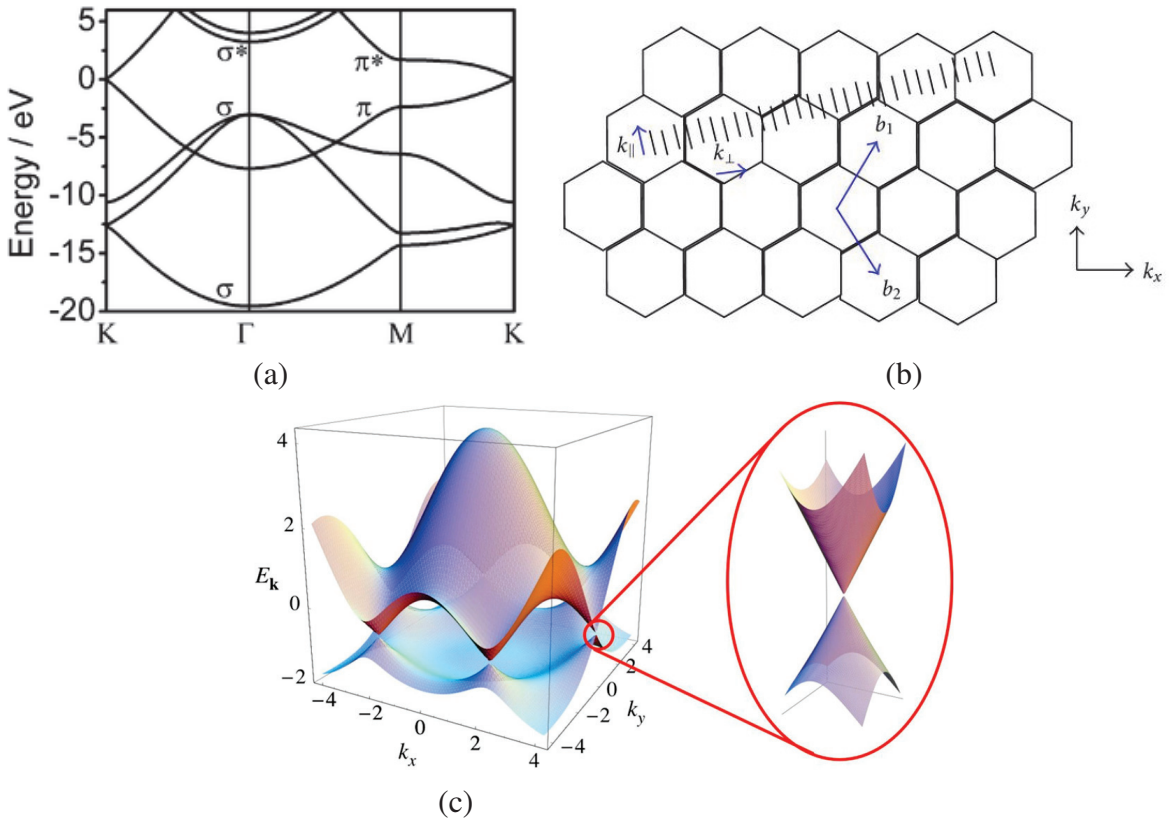

Figure 2.7 (a) Band structure of graphene. The energy dispersion along the high symmetry directions Γ*MK* of the 2D Brillouin zone ([38, 39]). (b)Vectors definition in the reciprocal lattice. $k_{\parallel}$ and $k_{\perp}$ are along the circumferential and nanotube axis direction, respectively. (c) The conduction band touches the valence band at the *K* and *K*′ points.

the physical properties of graphene. These two points are called Dirac points. The reason for giving this name will be explained later.

As mentioned above, the p_z orbitals forming the π energy bands can be treated independently in graphene. The electronic band structure of graphene π states is derived from the Schrödinger equation:

$$H\Psi(\mathbf{k}) = E_g(\mathbf{k})\Psi(\mathbf{k}), \tag{2.12}$$

where H is the Hamiltonian, $E_g(\mathbf{k})$ the eigenvalues, and $\Psi(\mathbf{k})$ is the eigenfunctions at wavevector $\mathbf{k}$. From the periodicity of the atom network, the eigenfunctions are written as a linear combination of Bloch functions of each sublattices (Φ_j):

$$\Psi(\mathbf{k}) = \sum_{j=A,B} c_j(\mathbf{k})\Phi_j((\mathbf{k},\mathbf{r})). \tag{2.13}$$

In the tight binding model [40], the Bloch functions can be expressed as a linear combination of the atomic wave function. Within this π-band approximation, the p_z electrons are described by the wave functions of $\varphi_z(\mathbf{r}-\mathbf{R}_A)$ and $\varphi_z(\mathbf{r}-\mathbf{R}_B)$, respectively, in sub-lattice A and B (see Fig. 2.2 (a)). Therefore, the Bloch functions for sublattices A and B are

$$\begin{aligned}
\Phi_A(\mathbf{k},\mathbf{r}) &= \frac{1}{\sqrt{N_{cells}}}\sum_{\mathbf{R}_A} e^{i\mathbf{k}\cdot\mathbf{R_A}}\varphi_z(\mathbf{r}-\mathbf{R_A}),\\
\Phi_B(\mathbf{k},\mathbf{r}) &= \frac{1}{\sqrt{N_{cells}}}\sum_{\mathbf{R}_B} e^{i\mathbf{k}\cdot\mathbf{R_B}}\varphi_z(\mathbf{r}-\mathbf{R_B}),
\end{aligned} \tag{2.14}$$

where N_{cells} is the number of unit cells in the graphene plane associated with atoms A and B. By substituting the expression of the eigenfunctions $|\Psi\rangle$ (Dirac's notation) in the Schrödinger equation (2.12), and multiplying the left side by $\langle\Psi_A|$ or $\langle\Psi_B|$, the eigenstates are derived by solving the system

$$\begin{pmatrix} H_{AA}(\mathbf{k}) - E_g(\mathbf{k})S_{AA}(\mathbf{k}) & H_{AB}(\mathbf{k}) - E(\mathbf{k})S_{AB}(\mathbf{k}) \\ H_{BA}(\mathbf{k}) - E_g(\mathbf{k})S_{BA}(\mathbf{k}) & H_{BB}(\mathbf{k}) - E(\mathbf{k})S_{BB}(\mathbf{k}) \end{pmatrix} \begin{pmatrix} c_A(\mathbf{k}) \\ c_B(\mathbf{k}) \end{pmatrix} = 0$$

here the matrix elements are as follows:

$$\begin{aligned}
H_{ij} &= \langle\Phi_i|H\left|\Phi_j\right\rangle \\
S_{ij} &= \langle\Phi_i|\Phi_j\rangle, \qquad i,j = A,B
\end{aligned} \tag{2.15}$$

the carbon atoms A and B are equivalent, thus

$$\begin{aligned} H_{AA} &= H_{BB}^{*}, \quad S_{AA} = S_{BB}^{*} \\ H_{AB} &= H_{BA}^{*}, \quad S_{AB} = S_{BA}^{*} \end{aligned} \tag{2.16}$$

With further the nearest-neighbor approximation and neglecting the overlap matrix element between wavefunctions S_{AB}, the eigenvalues are:

$$E^{\pm}(\mathbf{k}) = H_{AA} \mp H_{AB}. \tag{2.17}$$

The first term is a constant for self-interaction of each atom in atom A. Here we set $H_{AA} = 0$ as the reference. The second term means the interaction between the atom A and its nearest neighbors B. An atom A has 3 nearest neighbors (B1, B2 and B3) at the positions:

$$\mathbf{R}_{B1} = a_0 \begin{pmatrix} 0 \\ \frac{1}{\sqrt{3}} \end{pmatrix}, \mathbf{R}_{B2} = \frac{1}{2} a_0 \begin{pmatrix} 1 \\ \frac{1}{\sqrt{3}} \end{pmatrix}, \mathbf{R}_{B1} = -\frac{1}{2} a_0 \begin{pmatrix} 1 \\ \frac{1}{\sqrt{3}} \end{pmatrix}. \tag{2.18}$$

Thus the matrix elements can be expressed as,

$$H_{AB}(\mathbf{k}) = -\gamma_0 (e^{-i\mathbf{k}\cdot\mathbf{R}_{B1}} + e^{-i\mathbf{k}\cdot\mathbf{R}_{B2}} + e^{-i\mathbf{k}\cdot\mathbf{R}_{B2}}) \tag{2.19}$$

here -γ_0 is nearest neighbor hopping (approximately, -3.0 eV [41]). Finally, we get the valence (-) and conduction (+) π bands of graphene close to the Fermi energy.

$$E_g^{\pm}(\mathbf{k}) = \pm\gamma_0 \sqrt{1 + 4\cos(\frac{a_0 k_x}{2}) \sin(\frac{\sqrt{3} a_0 k_y}{2}) + 4\cos^2(\frac{a_0 k_x}{2})}. \tag{2.20}$$

The valence and conduction bands cross at the K and K' points, where the Fermi energy $E_F = 0$. Development of the cosines around these high-symmetry points yields

$$E_g^{\pm}(\mathbf{k} + K) = E_g^{\pm}(\mathbf{k} + K') = \pm \frac{\sqrt{3}\gamma_0 a_0}{2} \sqrt{k_x^2 + k_y^2} \tag{2.21}$$

showing a peculiar quasi-linear dispersion of graphene band structure in the K and K' valleys. The points close to the point K, which specify six locations in momentum space are called Dirac points (see Fig. 2.7 (c)). The "massless Dirac fermions" describe the linear dispersion realization in Eq. (2.21). They have the same dispersion as massless Dirac particles near the K and K' points. The linear relation of electrons energy and momentum leads to them propagating through graphene like massless Dirac fermions. This is the reason why we refer to them as Dirac points.

2.3 Electronic properties of CNTs

2.3.1 Zone folding approximation

The band structure of carbon nanotubes can now be derived from the one of graphene. As mentioned above, a nanotube is constructed from the graphene sheet by defining its chiral vector $\mathbf{C_h}$. Along $\mathbf{C_h}$, a periodic boundary condition imposed on the graphene wave function yields $\Psi(\mathbf{r}+\mathbf{C_h}) = \Psi(\mathbf{r})$, which is satisfied if and only if $\exp(i\mathbf{r}\cdot\mathbf{C_h}) = 1$. Along the main axis of the nanotube, the reciprocal lattice wave vector $\mathbf{k}_{\|}$ (see Fig. 2.7 (b)) is determined by the translational vector. $\mathbf{k}_{\|}$ remains continuous in the approximation of infinitely long tube, and its length falls in the interval $[-\pi/|\mathbf{T}|, \pi/|\mathbf{T}|]$. Along the circumference of the nanotube, i.e. parallel to $\mathbf{C_h}$, the wave vector $\mathbf{k}_{\perp}$ is quantized according to the periodic boundary condition:

$$\frac{|\mathbf{C_h}|}{\lambda} = |\mathbf{C_h}| \cdot \frac{\mathbf{k}_{\perp}}{2\pi} = integer \tag{2.22}$$

we obtain

$$k_{\perp,q} = \frac{2\pi}{|\mathbf{C_h}|} q = \frac{2}{d_t} q \qquad q = -\frac{N}{2}+1, \cdots, -\frac{N}{2}, \tag{2.23}$$

where N is the number of hexagons in the nanotube unit cell ($N = N_C/2$). In the reciprocal space of graphene, the couple ($\mathbf{k}_{\perp}$,$\mathbf{k}_{\|}$) (see Fig. 2.7 (b)) defines 1D cutting lines corresponding to the 1D energy subbands of nanotubes. This method, so-called zone-folding, is sketched in Fig. 2.9 for armchair and zigzag nanotubes. The quantized wave vectors $\mathbf{k}_{\perp}$ and the reciprocal lattice vector $\mathbf{k}_{\|}$ are derived from

$$\begin{aligned} &\mathbf{C_h}\cdot\mathbf{k}_{\perp} = 2\pi, \quad \mathbf{C_h}\cdot\mathbf{k}_{\|} = 0, \\ &\mathbf{T}\cdot\mathbf{k}_{\|} = 2\pi, \quad \mathbf{T}\cdot\mathbf{k}_{\perp} = 0. \end{aligned} \tag{2.24}$$

Thus, $\mathbf{k}_{\perp}$ and $\mathbf{k}_{\|}$ can be expressed as

$$\mathbf{k}_{\perp} = \frac{1}{N}(-t_2\mathbf{b_1} + t_1\mathbf{b_2}), \quad \mathbf{k}_{\|} = \frac{1}{N}(m\mathbf{b_1} - n\mathbf{b_2}) \tag{2.25}$$

The first Brillouin zone of CNTs consists of N k-lines (Fig. 2.9) of length $2\pi/|\mathbf{T}|$ and $2/d_t$ is the step size in $k_{\perp}$ direction. In other words, the cutting lines in the graphene conduction and valence bands are defined by:

$$\mathbf{k}_q = q\mathbf{k}_{\perp} + k\frac{\mathbf{k}_{\|}}{|\mathbf{k}_{\|}|}, \tag{2.26}$$

where $q \in [-N,N]$, $k \in [-\pi/|\mathbf{T}|, \pi/|\mathbf{T}|]$. $\mathbf{k}_\perp$ gives the discrete k values in the direction of $\mathbf{C}_h$. Another reciprocal lattice vector $\mathbf{k}_\parallel$ is along the nanotube axis and it is usually considered continuous. Finally the one-dimensional dispersion of the band q is obtained by inserting Eq. (2.26) in the dispersion of graphene Eq. (2.20):

$$E_q^{\pm}(\mathbf{k}) = E^{\pm}(k)(q\mathbf{k}_\perp + k\frac{\mathbf{k}_\parallel}{|\mathbf{k}_\parallel|}) \tag{2.27}$$

Close to Fermi level, i.e. close to K-point, the energy dispersion is linear in a first approximation. Hence, the dispersion of subband q can be expressed as

$$E_q^{\pm}(k) \approx \pm\frac{\sqrt{3}\gamma_0 a_0}{2}|\mathbf{k_q} - \mathbf{k_F}|, \tag{2.28}$$

where $\mathbf{k}_F$ is the Fermi wave vector. As in the case of graphene, K between K' has a two-fold degeneracy in the subbands. Due to symmetry, subbands with $k_\perp = |k_0|$ and $k_\perp = -|k_0|$ have exactly the same dispersion relation except that one is close to K point and the other close to K' point.

2.3.2 Semiconducting and metallic nanotubes

We can find that the reciprocal lattice $\mathbf{k}_\perp$ is much smaller because of the larger nanotube unit cell in real space. Thus, using the zone-folding method we map out the whole Brillouin zone and get the electronic band structure of SWCNT. Due to the quantization of $\mathbf{k}_\perp$, the energy band of carbon nanotubes are not so continuous like that of graphene. Fig. 2.8 gives a sketch zone folding approximation and cutting of the bands of graphene close to Dirac point. The green dashed line goes along the chiral vector $\mathbf{C}_h$ direction and the black dashed line indicates the axis direction (that is translation vector $\mathbf{T}$) and have constant $\mathbf{k}_\perp$ values. On the other hand, the angle between Γ $\mathbf{K}$ and $\mathbf{k}_\perp$ is the chiral angle θ. From 2D band structure of graphene in Fig. 2.7 (a), we know that $\mathbf{k}_\perp$ nearest the K point which dominates the fermi level and determines the conductivity of carbon nanotubes. It is also known that band structure of graphene does not have bandgap at K points. If one of the $k_\perp$ of nanotubes goes through K points, the nanotube will be metallic. Otherwise, the tube is semiconducting with a bandgap.

It is easy to show that one third of all nanotubes are metallic. If $k_\perp$ line crosses the point K, the distance between Γ and the intersection point is $(4\pi/3a)\cos\theta$. From Eq. (2.23), we get q value and introduce d and θ from the Eq. (2.4):

$$q = \frac{d}{2}k_\perp = \frac{d}{2}\cdot\frac{4\pi}{3a}\cos\theta = \frac{2n+m}{3} = n - \frac{n-m}{3} \tag{2.29}$$

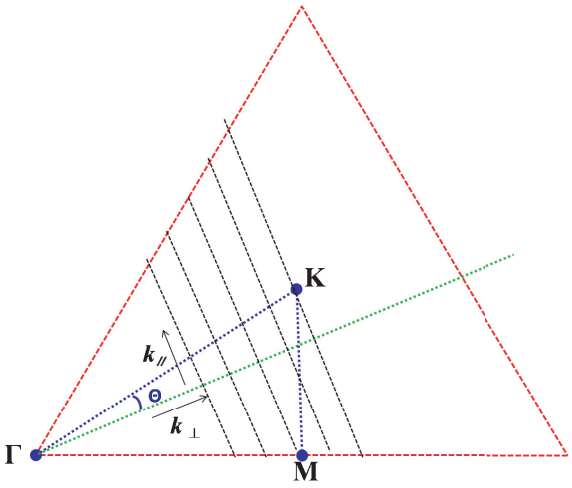

Figure 2.8 Sketch of the determination the band structure of nanotubes from the one of graphene

Thus, if $(n-m)/3$ is integer, then $k_\perp = (2/d)\cdot q = 2(2n+m)/(3d)$ will pass through the K point and give a gapless dispersion relation. If $(n-m)/3$ is not an integer, then the tubes are semiconducting. That is, 1/3 nanotubes are metallic and 2/3 are semiconducting. In this view, carbon nanotubes can be further classified based on the result of $\mu = mod(n-m,3)$ (Fig 2.4):

(1) $\mu = 0 \rightarrow$ metallic

(2) $\mu = +1 \rightarrow$ semiconducting type I

(3) $\mu = -1 \rightarrow$ semiconducting type II.

The cutting lines in the vicinity of the K point are shown in Fig. 2.9 for three different cases, $\mu = 0$, $\mu = +1$ and $\mu = -1$. Fig. 2.9 (a) corresponds to the cutting lines crossing the K point, resulting in metallic behavior. The Brillouin zone of a carbon nanotube is represented by the cutting line which passes through the highest symmetry point Γ. In (b) and (c), the K points are located at 1/3 and 2/3 distance of in units $k_\perp$ and the cutting lines do not cross the K and K' points. We also calculate the corresponding reciprocal vectors of three types of nanotubes in Fig. 2.9. More precisely, armchair CNTs are always metallic, whereas zigzag and chiral CNTs can be either metallic or semiconducting.

Fig. 2.10 shows schematic band dispersions and corresponding densities of states of (a) armchair ($n = m$) and (b) semiconducting ($\mu = \pm 1$) nanotubes. The metallic tube presents one valence and one condition band crossing the Fermi energy. Close to the Fermi energy (E_F) the dispersion relation can be expressed as

$$E^{\pm} \approx \frac{\sqrt{3}}{2}\gamma_0|\mathbf{k}-\mathbf{k_F}|, \tag{2.30}$$

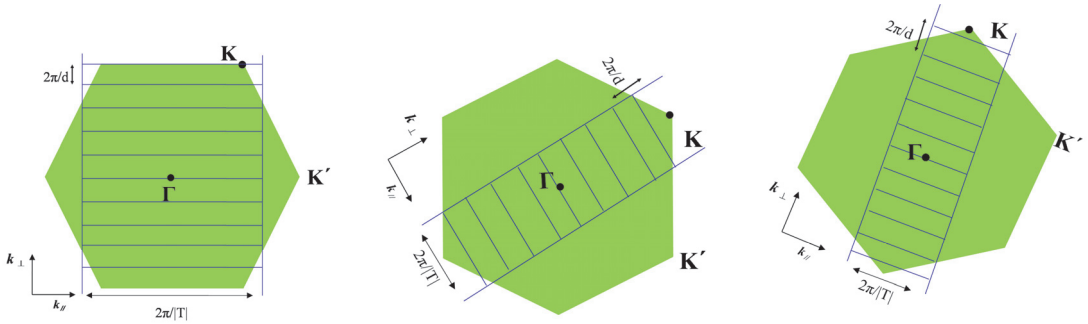

Figure 2.9 Three different configurations of the the cutting lines in the vicinity of the K points. (a) $\mu = 0$. The CNT (5,5) is metallic. The vectors $k_\perp$ and $k_\parallel$ are reciprocal lattice vectors corresponding to $\mathbf{C}_h$ and $\mathbf{T}$ respectively. $\mathbf{C}_h$ = (5,5), $\mathbf{T}$ = (1,-1), $\mathbf{k}_\perp = (\mathbf{b}_1 + \mathbf{b}_2)/10$, $\mathbf{k}_\parallel = (b_1 - b_2)/2$ and N = 10. (b) $\mu = +1$. The CNT (7,0) with vector $\mathbf{C}_h$ = (7,0), $\mathbf{T}$ = (1,-2), $\mathbf{k}_\perp = (\mathbf{2b}_1 + \mathbf{b}_2)/14$, $\mathbf{k}_\parallel = -\mathbf{b}_2/2$, and N = 14. (c) $\mu = -1$. The CNT (8,0) with vector $\mathbf{C}_h$ = (8,0), $\mathbf{T}$ = (1,-2), $\mathbf{k}_\perp = (\mathbf{2b}_1 + \mathbf{b}_2)/16$, $\mathbf{k}_\parallel = -\mathbf{b}_2/2$, and N = 16. (b) and (c) are semiconducting nanotubes of types I and II, respectively.

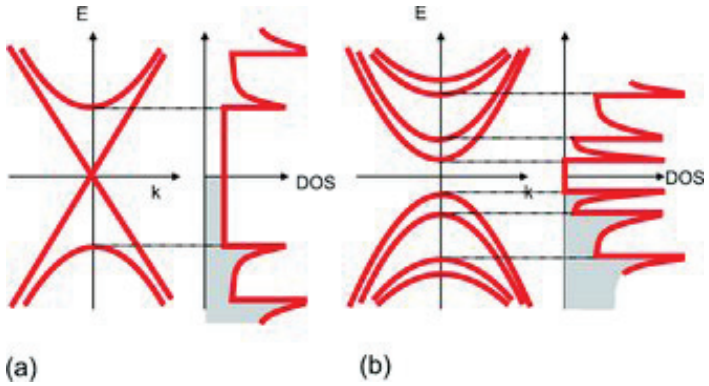

Figure 2.10 Schematic electronic band structure of (a) metallic ($n = m$) and (b) semiconducting ($\mu = \pm 1$) carbon nanotubes, in the tight binding approximation with linear dispersion of graphene [42].

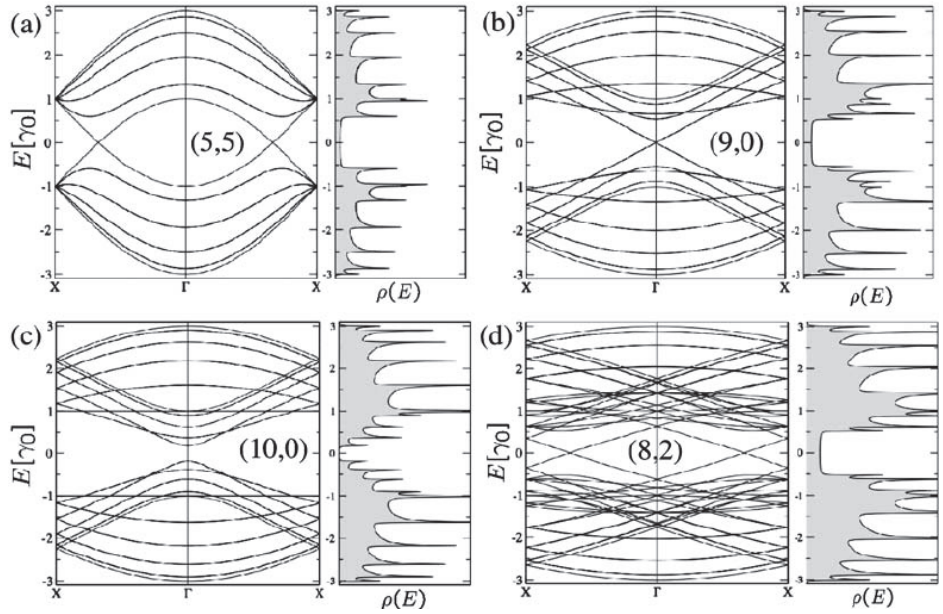

Figure 2.11 The band structure of densities of states (DOS) of the armchair (5,5), zigzag (9,0), (10,0) and chiral nanotube (8,2) as calculated using the π/π^* tight-binding model under the zone-folding approximation [43].

where **k** is wave-vector, yielding a linear energy momentum relation. For semiconducting CNTs, the highest valence subband and the lowest conduction are separated by an energy gap, whose value is estimated as:

$$\Delta E_g^1 = \frac{2\pi a_0 \gamma_0}{\sqrt{3}|\mathbf{C_h}|} = \frac{2a_{c-c}\gamma_0}{d_t}. \tag{2.31}$$

The ΔE_g^1 is estimated to decrease with the inverse of the tube diameter d_t [43]. In fact, trigonal warping leads to a band gap not only relying on the diameter but also on the (n,m) chiriality [44].

We give complete band structures and densities states of the armchair (5,5), zigzag (9,0), (10,0) and chiral (8,2) in Fig. 2.11. For (5,5) armchair, six conduction and six valence bands have been presented with mirror symmetry. Moreover, four of them are degenerate including 10 electrons together. For all armchair nanotubes, the energy bands have a large degeneracy at the zone boundary (X point, $k = \pm\pi/a$).

The electronic density of the states (DOS) is defined by $\Delta N/\Delta E$ counting the number of available states ΔN in given energy span $\Delta E(\Delta E \to 0)$. As a CNT is a one-dimensional system, the DOS diverges as $1/\sqrt{E}$, with van Hove singularities (VHs) [45] at energies close

to band edges. For all the metallic CNTs, the density of the states per unit length along the nanotube axis is a constant at the Fermi energy (E_F):

$$\rho(E_F) = \frac{2\sqrt{3}a_{c-c}}{\pi\gamma_0|\mathbf{C_h}|} \tag{2.32}$$

The DOS of zigzag carbon nanotubes (9,0) is also shown in Fig. 2.11 (b). As discussed before, it is metallic, whereas for (10,0) there is a small band gap at the Γ point, which is approximately 0.6 eV for CNTs with diameter of 1 nm [35, 46]. The band structure and DOS of the chiral nanotube (8,2) are also illustrated in the same figure. Because of $mod(n-m) = 0$, the nanotube shows a metallic behavior, with a band crossing at the Fermi energy level. Moreover, the DOS of metallic chiral nanotubes also exhibits van Hove singularities.

The DOS of both metallic and semiconducting nanotubes (achiral or chiral) have first been determined by scanning tunneling microscopy (STM) [47]. Meanwhile, resonant Raman scattering [48], optical absorption and emission measurements [49, 50] also confirmed the van Hove singularities of the density of states of SWCNT.

2.3.3 Phonon modes and Raman spectroscopy

The phonon dispersion relations of graphene similarly to the electronic properties, can be calculated by tight-binding or *ab initio* methods. The phonon dispersion relations in SWNTS have been obtained from those of the 2-D graphene sheet by using the same zone-folding approach of the Eq. (2.27):

$$\omega^{mq}(\mathbf{k}) = \omega^m(q\mathbf{k}_\perp + k\frac{k_\parallel}{|k_\parallel|}) \tag{2.33}$$

where m = 1, 2, $\cdots$, 6; q = 0, 1, $\cdots$, N-1; -π/|**T**| < k < π/|**T**|. All $2N$ carbon nanotubes in the unit cell can produce $6N$ phonon modes, because of three degrees of freedom of each atom. Among the $6N$ branches only a few modes are Raman active. The number of the Raman active modes can be calculated [51] from the crystal lattice and symmetry by group theory, as listed below:

armchair: $2A_{1g} + 2E_{1g} + 4E_{2g}$

zigzag: $2A_{1g} + 3E_{1g} + 3E_{2g}$

chiral: $2A_{1g} + 3E_{1g} + 3E_{2g}$

Here we use the force constant model [52] and the zone-folding method [53] to calculate the phonon dispersions of the armchair (10,10) CNT of Fig 2.12. For the $2N = 40$ carbon atoms of the (10,10) CNT per circumferential strip, we can obtain 120 phonon branches with

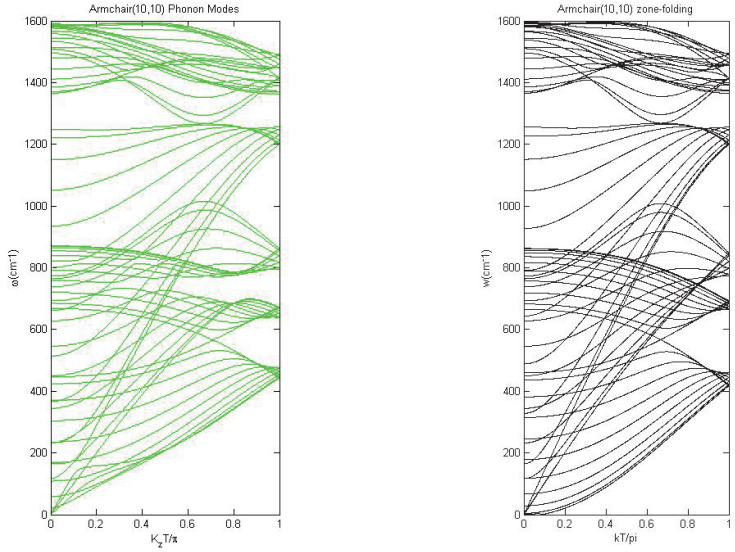

(a) (b)

Figure 2.12 The calculation for phonon dispersion of armchair (10,10) SWCNT: (a) Force constant method [52] (b) zone-folding method [53].

a large number of phonon modes doubly degenerate. There are a longitudinal acoustic (LA) mode, corresponding to motion of the atoms along the tube axis, two degenerate transverse acoustic (TA) modes, corresponding to atomic displacements perpendicular to the nanotube axis (a combination of in-plane and out-of plane TA modes in graphene), and a twist mode corresponding to a torsion of the tube around its axis. Another important mode is radial breathing mode (RBM), which is the strongest low frequency mode, describing the radial expansion-contraction of CNTs. The calculated energy of the RBM mode of the (10,10) CNT is 21.7 meV [54].

Experimentally, the force constants fitted on the phonon frequencies can be measured by inelastic Raman scattering in graphite [55]. Moreover, Raman spectroscopy is one of the most powerful and widespread techniques to study the characteristics of carbon nanotubes at extreme conditions (high pressure). Raman spectroscopy is the inelastic scattering of (optical) photons from a material. In general, when a beam of light interacts with the target matter, a photon is absorbed, exciting an electron to an empty state, which decays emitting another photon almost immediately. If the scattered (emitted) photon has the same energy (frequency/wavelength) of the incident (absorbed) photon, the scattering is elastic (Rayleigh scattering, Fig. 2.13 (a)). On the other hand, if the emitted photon has a slightly different wavelength, we talk about Raman scattering. When the incident photon loses energy and emits a longer wavelength photon, the red-shifted Stokes scattering occurs in a

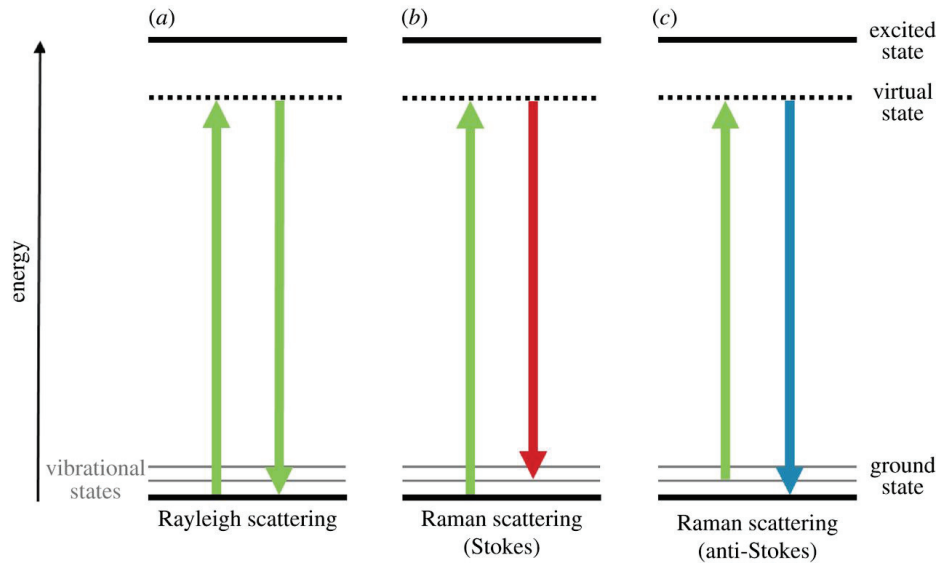

Figure 2.13 Sketch of diagram of Rayleigh scattering (elastic) and Raman (inelastic)

higher vibrational state (Fig. 2.13 (b)). If the electron is already in a higher vibrational state, resulting in the emission of a lower wavelength photon (Fig. 2.13 (c)), that phenomenon is called blue-shifted anti-Stokes scattering.

Due to the uniqueness of characteristic bonds and vibrational modes of each material, the Raman spectra can be used as fingerprint to identify different molecules, crystals and disordered systems. As a consequence of their unique 1-D phonon bands, resonant Raman scattering spectroscopy is a powerful technique for the characterization and study of CNTs. The most widely used and intense Raman-active vibrational modes to study and characterize CNTs are shown in Fig. 2.14. The lowest frequency mode ($\approx$ 120-300 cm^{-1}) for CNTs with diameter between 0.9 and 2.0 nm, which only appears in CNTs and fullerene structures is the RBM [56], corresponding to the coherent vibration in the radial direction. It is one of the most used methods to determine optically the tube diameter, since its frequency varies inversely with the nanotube diameter [56]:

$$\omega_{RBM} = \frac{A}{d_t} + B. \tag{2.34}$$

Where A and B are sample and environment dependent parameters, given by experiments. The excitation energy dependence of specific RBMs can be determined by the laser source. The energy at which the RBM Raman intensity reaches a maximum corresponds to the incident and scattered photon resonances with the SWCNT optical transition. Consequently, both diameter and optical transition energy can be determined from RBM Raman measurements, allowing for assignment of RBM Raman features to specific (n,m) SWCNTs. The RBM

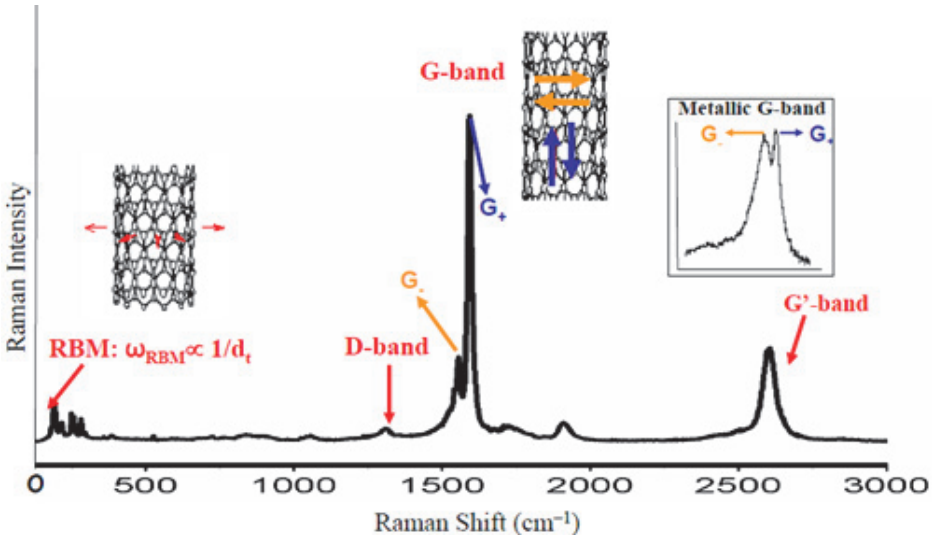

Figure 2.14 A typical resonant Raman spectrum of a bulk SWCNT showing important features like RBM, D-band, G-band and G'-band, taken at 785 nm excitation [54].

intensity profile with a tunable laser can give directly the electron transition energy within ± 3 meV [48, 57]. Both diameter and transition energies can be determined from RBM Raman measurements, then they can be used to assign the chiral index (n,m).

As shown in Fig. 2.14, the G-band of a SWCNT, ranging from 1500 to 1600 cm^{-1} is another typical intense vibration mode, originated from folding of the the Raman active optical phonon mode E_{2g} of 2-D graphene . Due to the phonon wave vector confinement along the SWCNT circumferential direction and the curvature-induced inequality, the G-band is discomposed into G^+ and G^- peaks. Depending on the difference of lineshape (intensity), it is possible to distinguish metallic or semiconducting nanotubes (see Fig. 2.14). Other bands as the D-band (characteristic of the presence of defects) or the double resonant G' band are discussed in many works [51, 58].

2.4 Carbon nanotubes under high pressure

Coupled to its one-dimensional nanomaterial, CNTs exhibit fascinating mechanical and electronic properties. Their robust mechanical properties are due to the strong sp^2 covalent bonds between carbon atoms. Theoretical prediction as well as experimental results indicate a Young's modulus close to 1 TPa for SWCNTs along their symmetry axis [4, 59]. However, the radial stability of the nanotubes is much lower. The unique structures and special characteristics have led to intense research on this material over the last decade. These outstanding properties suggested a lot of potential applications of the usage of CNTs, i.e.

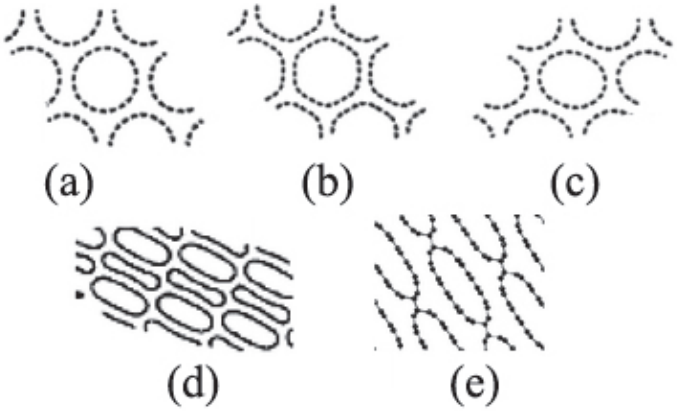

Figure 2.15 Different shapes of bundled SWCNTs [63]. (a) circular shape stable at ambient pressure. (b) hexagonal polygonization (c) ovalization (d) mixture of racetrack and peanut shape (e) interlinked racetrack shape

hydrogen storage [60], gas sensors [61], nanochemical devices [62] and so on. On the other hand, high pressure can serve as an effective means to create new structures and new phases by varying the interatomic distance of a substance. It is really an intriguing and important topic to employ high pressure to study the structure and the property of CNTs. In the context of carbon nanotubes, the pressure can induce the change of the vibrational characteristics, and consequently, CNTs can undergo phase transitions. Such phase transitions corresponds to changes of radial shape and collapse of the tubes.

With different calculation methods, including classical molecular dynamics , *ab-initio* calculations, or a combination of different techniques, one obtains different results due to the approximation of different models and limit for the method of calculation. However, a common result is that the SWCNTs undergo a structural phase transition and the cross-section of bundled CNTs evolve from circular to oval, or hexagonal to peanut-like, and even race-track-like at high pressures, as shown in Fig. 2.15.

The nature of the phase transition and the deformation paths are extremely complex. It is expected that the value of collapse pressure P_c decreases with the increasing nanotube diameter, following the function of $P_c \sim 1/d^3$ [64, 65] or $P_c \sim 1/d$ [66], as shown in Fig. 2.16 and Fig. 2.17, respectively.

The structural deformation further induces the change of electronic properties. Charlier *et al.* [25], through simple tight-binding models calculations, reported that the polygonization from the circular shape induces strong $\sigma^* - \pi^*$ hybridization effects due to the high curvature effect near the edges of the cross section for zigzag nanotubes. Lower symmetry and curvature effects narrow the band gap. Furthermore, Lammert *et al.* [67] revealed that the deformation of nanotubes can produce two greatly different behaviors: metal nanotubes (n,n) and $(3n,0)$

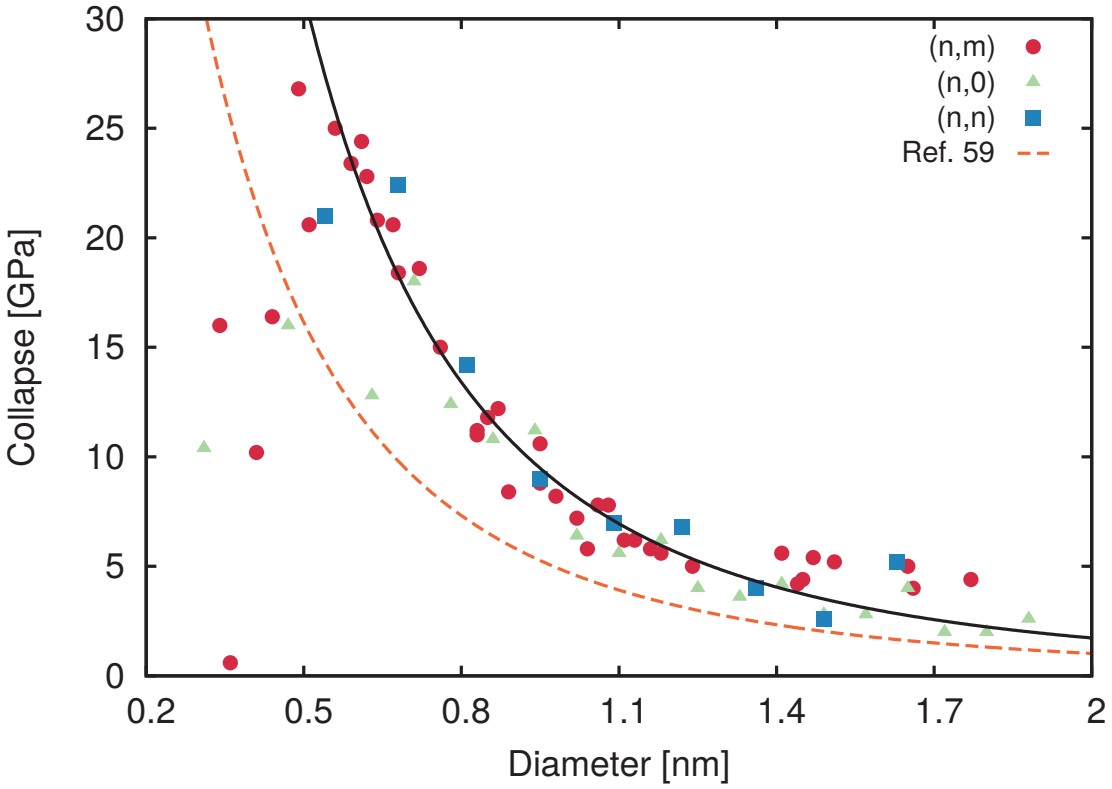

Figure 2.16 Collapse pressure as a function of the diameter of nanotube (zig-zag, armchair and chiral nanotubes) fitted by $P_c = \alpha/(\beta + d)^3$ with density-functional tight-binding study from Ref. [65]

.

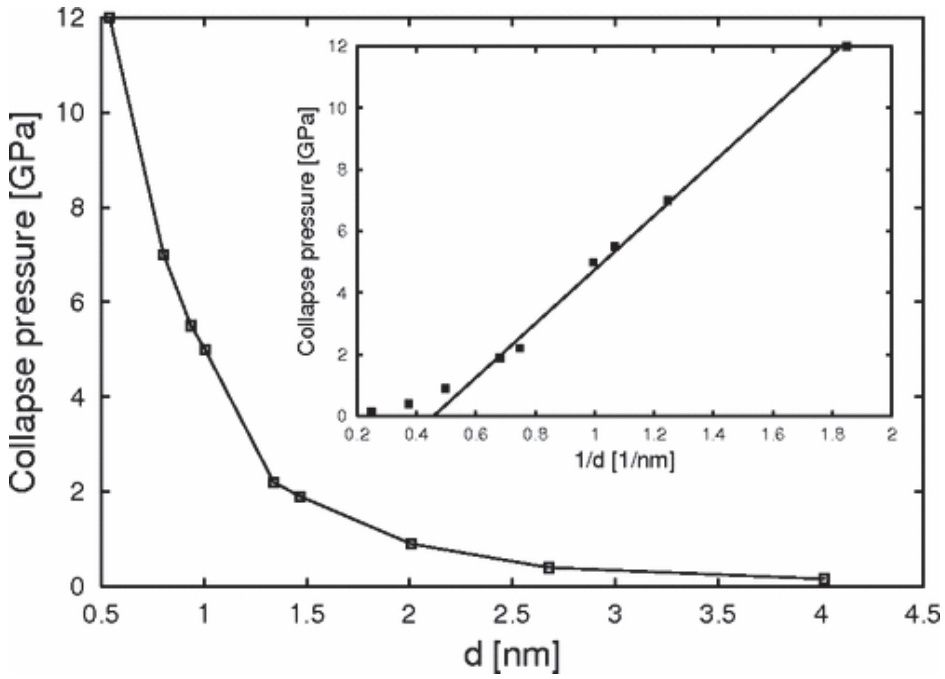

Figure 2.17 Collapse pressure of SWCNT bundles as a function of tube diameter. The inset shows a fit using P_c, $P_c = A/d$, of classical molecular dynamic calculations from Ref. [66].

are extremely sensitive to deformation. Thus the radial deformation in the SWCNTs could lead to open or close the band gap, causing an insulator to metal transition or, on the contrary, a transition of metallic into small-gap nanotubes [67–70].

Nanotubes collapse has been experimentally investigated by X-ray diffraction [71, 72], Raman spectroscopy [73–77], neutron diffraction and optical absorption [78] for decades. Studies in literature disagree on the pressure of collapse, measured as the point of disappearance of RBMs. Most of the works agree on critical pressures of around 2 GPa [74, 79]. However, it is also reported that the RBMs still can be observable even up to 10 GPa, thus RBM disappearance cannot be the phase transition signal [77]. Cailler *et al.* [14] observed a change of sign in the pressure derivative of the G-band Raman shift which showed to be a signature of the collapse pressure (see Fig. 2.18 (a)). Also Yao *et al*. [80] observed a *G*-band frequencies "plateau" under pressure clearly in Fig. 2.18 (b). Both the *G*-band inflexion in its pressure evolution [14] or the plateau [80] have been then identified as signatures of a structure change and as the onset of the collapse. A recent work of Torres-Dias *et al.* [15] has shown that the penetration of pressure transmitting medium inside the tubes can play a significant role in the pressure evolution of the G-band energy with pressure and could then explain the observed difference in various experiments.

Although the way of characterizing the collapse phase transition pressure is still under debate, large diameter collapsed nanotubes at ambient pressure have been observed by High Resolution Transmission Electron Microscope (HRTEM) imaging, as shown in Fig. 2.19. Van der Waals forces are in that case responsible for the collapse.

High pressure theoretical and experimental studies have not only been conducted for SWCNTs, but also for DWCNTs. With classical molecular dynamics simulation, Gadagkar *et al*. [83] obtained that the collapse pressure followed $P_c \sim 1/R^3$, where R is the effective radius as $1/R^3_{eff} = (1/n)\sum_{i=1}^{n}(1/R_i^3)$, and n is the number of MWCNT walls. They also demonstrated that the inner tube supports mechanically the outer tube, while the outer tube screens the environment. However, P_c in double-wall CNTs, was reported to depend mainly on the diameter of the inner tube [84]. Experimentally, Aguiar *et al*. observed that the collapse of DWCNTs can be divided into two steps: The first step corresponds to the deformation of outer tube with 1.56 nm at $\sim$ 21 GPa, then followed by the collapse of the inner tube with a diameter of 0.86 nm at $\sim$ 25 GPa [18]. Later, these authors investigated the effect of intercalation and inhomogeneous filling on the collapse of bromine-intercalated CVD-grown DWCNTs, and observed that a saturation or downshift of the *G* band denotes the onset of the collapse at 12-13 GPa [81] as shown in Fig. 2.20. With a shock wave compression study, Mases *et al*. [85] observed structural damage between 19 and 26 GPa, indicating the collapse of the tubes. These discrepancies can be attributed to the difficulty in working with double-wall CNT samples, due to the large diameter distribution or the purity of samples.

Nearly at the same time, Aguiar *et al.* also [82] observed theoretically that DWCNTs first transform by polygonizing the outer tube, while the inner tube keeps an oval shape until simultaneous collapse of the outer and inner tube, as shown in Fig. 2.21.

Besides studies of pure nanotubes (including SWCNTs, DWCNTs and MWCNTs), the introduction of foreign species into nanotubes have also attracted a great interest. For example, when polyiodides are confined into SWCNTs under high pressure, modifications occur in two steps: first between 1 and 2.3 GPa, polyiodides are modified, second between 7 and 9 GPa, the nanotubes are modified. The great change in the Raman mode intensities indicates the formation of new phase of iodides [86].

Moreover, for nanotubes filled with C_{70} (peapods) [14] molecules, transitions were observed under pressure, indicated by modifications of the Raman spectra, concerning RBM and G-band modes. One first transition occurs at about 2-2.5 GPa, corresponding to ovalization or polygonization of the nanotubes (Fig. 2.23). The other transition takes place at 10-30 GPa and is due to the deformation of the peapods and the flattening of the tubes (see Fig. 2.18 (a)). For C_{60} molecules confined in nanotubes, polymerization can be achieved and

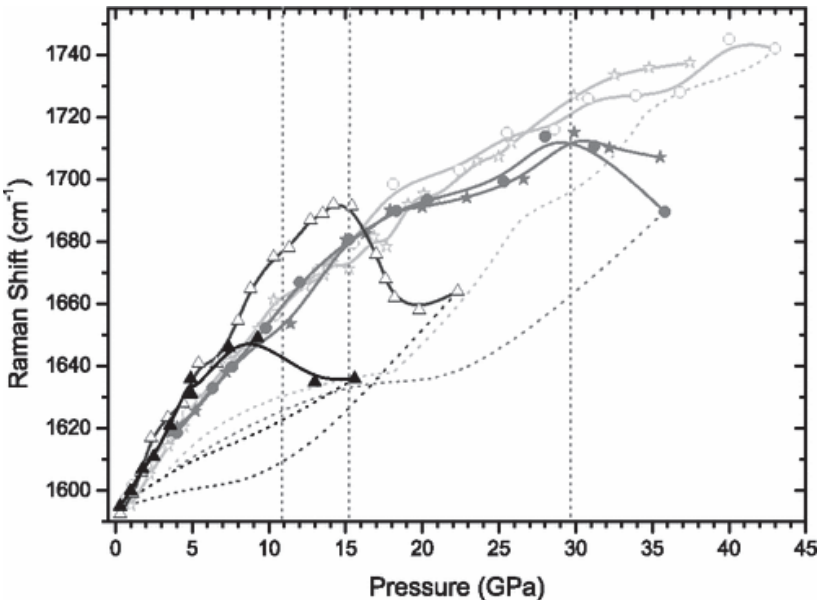

(a)

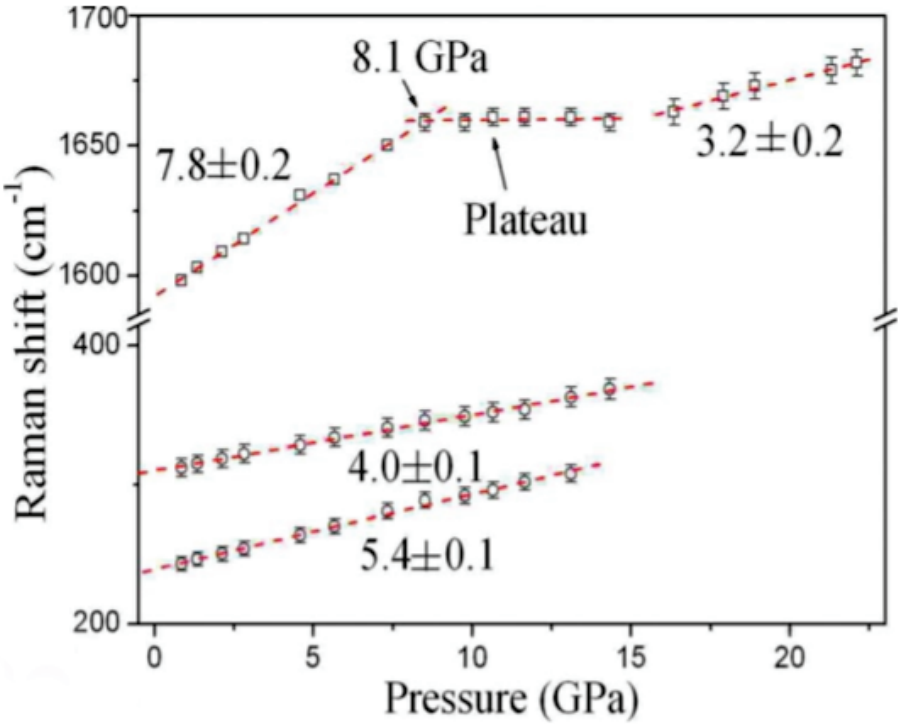

(b)

Figure 2.18 (a) Raman frequency evolution of the TM maximum intensity with pressure in different PTM. Filled and hollow symbols represent the peapods and empty nanotubes, respectively [14]. (b) The frequencies of two RBM (circles) and the most intense G^+ peak (squares) about SWCNTs (with diameter 0.6-1.3 nm) are plotted with pressure from Ref. [80].

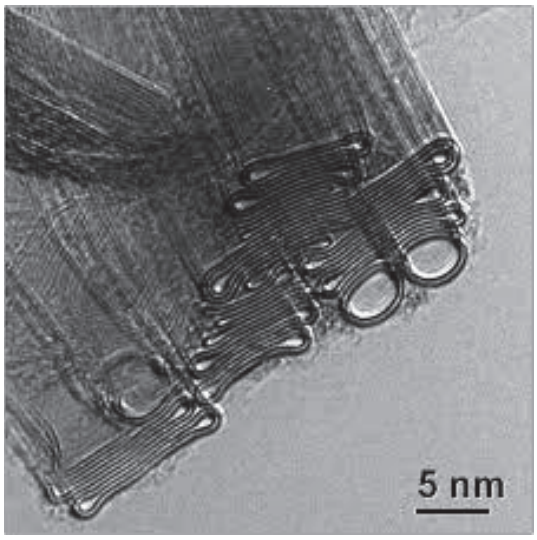

Figure 2.19 HRTEM images of collapsed CNTs, including single, double and triple wall CNTs from Ref. [73].

measured by the distance of C_{60}-C_{60} as a function of pressure until formation of a corrugated tubule [12, 13] (see Fig. 2.24).

In conclusion, many spectroscopic techniques, like Raman spectroscopy, and theoretical studies, based on classical molecular dynamics, density functional theory or tight-binding have been used to investigate the collapse behavior of CNTs under high pressure. We will show in the next chapters our original contributions to this topics and try to understand the effect of diameter, the chirality, the PTM as well as filling on the collapse of CNTs.

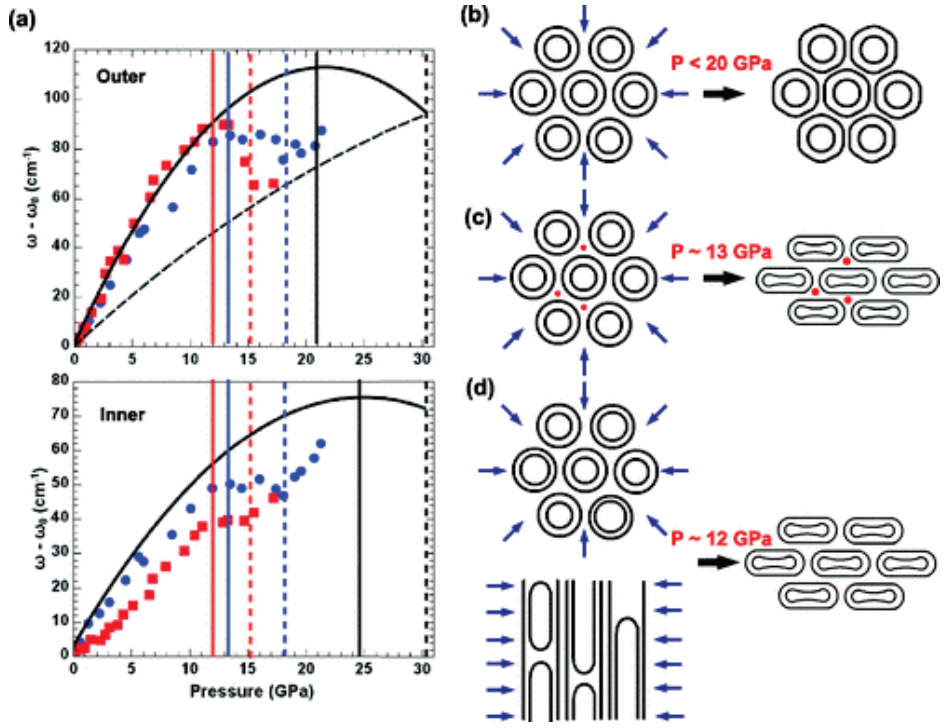

Figure 2.20 (a) The plots of G^+ components of inner and outer tubes of DWCNTs. (b) Bromine-intercalated DWNTs (c) peapod-derived DWNTs and (d) samples from Ref. [81].

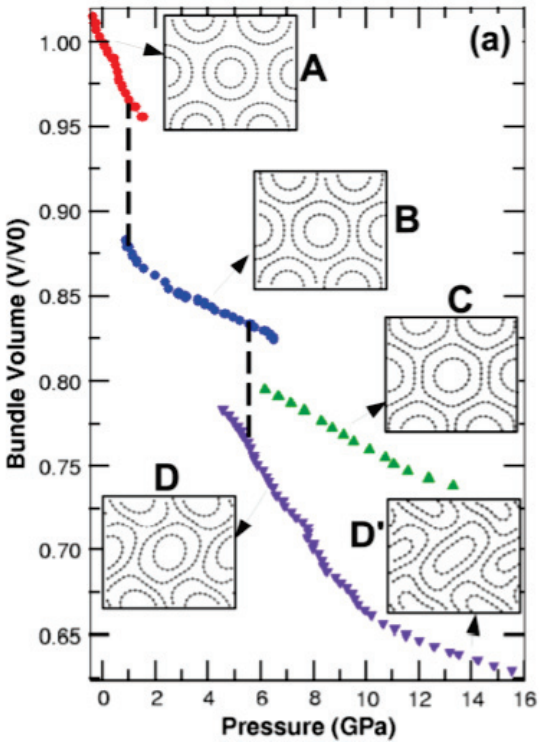

Figure 2.21 Bundle volume of SWCNTs as a function of pressure. The insert presents the snapshots of the evolution of different phases. A) The configuration of DWCNTs under ambient pressure, with circular shape both for inner and outer tube. B) The configuration with polygonization for the outer tube and circular for inner tube. C) The configuration with polygonization for the outer tube and oval shape for the inner tube. D) The configuration with peanut/oval shapes for outer and inner tubes from Ref. [82].

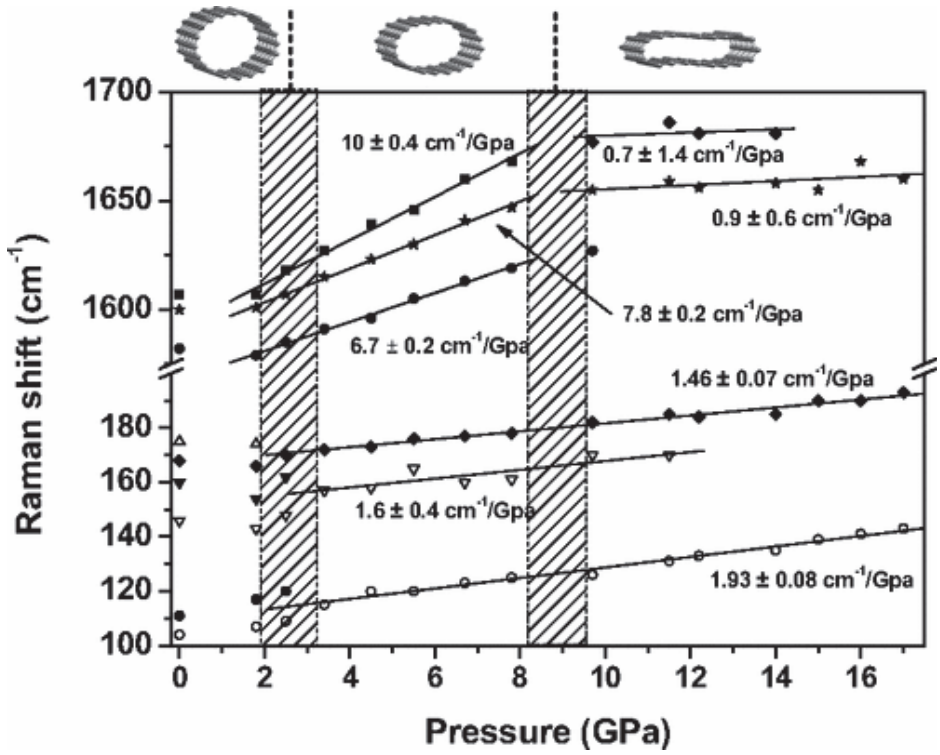

Figure 2.22 Raman shift as a function of pressure of I@SWCNT. The grey regions correspond to the modification of the polyodides and SWCNTs during the compressing procedure from Ref. [86].

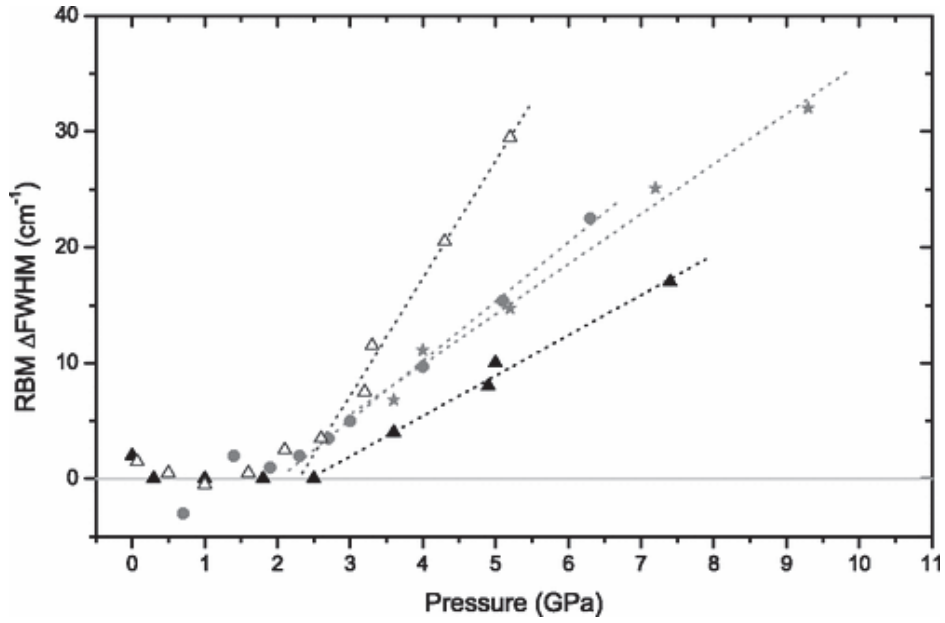

Figure 2.23 RMB linewidth of C_{70} in different pressure transmitting medium (PTM), oil (filled triangles), alcohol (filled circles) and argon (filled stars) [14].

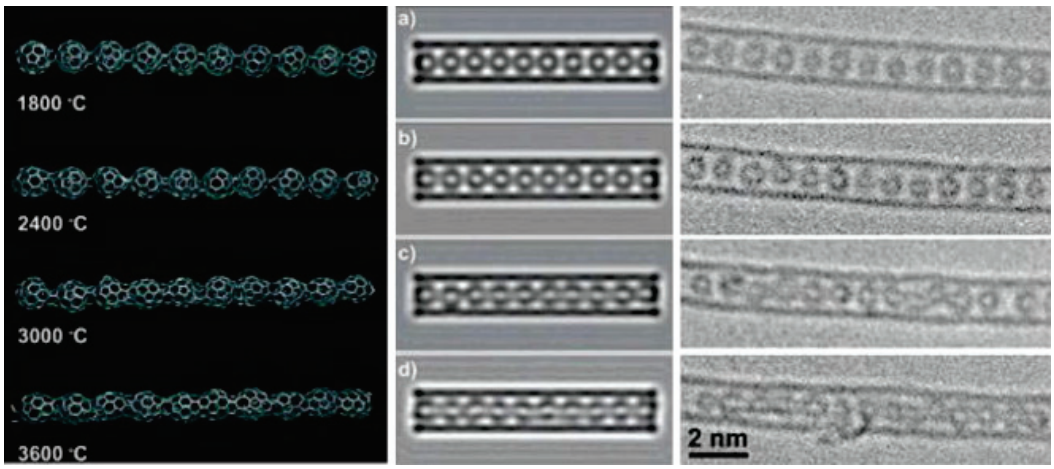

Figure 2.24 Coalescence of C_{60} molecule. Left images are obtained by MD simulations, noting that the outer (10,10) tube is not depicted for visualization purposes. The middle images are the HRTEM simulations corresponding to the left temperature and right images are the experimental sequences of C_{60} peapods. Four phases are visible at different temperatures: (a) 1800 K (b) polymerization (2400 K), (c) rearrangement (3000 K) (d) coalescence (3600 K) into a corrugated tubule from Ref. [12].

Chapter 3

Theoretical background

Density-Functional Theory (DFT) is by now the most successful and popular quantum mechanical method for condensed matter *ab initio* simulations of, e.g. band structure of solids, superconductivity and magnetic properties of alloys. DFT attributes its versatility to the generality of its fundamental concepts and the flexibility one has in implementing them. In spite of this flexibility and generality, DFT is based on quite a rigid conceptual framework.

In this chapter, I introduce the basic concepts underlying density functional theory and some recent developments in exchange correlation functionals. In the following, a basic introduction on van der Waals functional will be presented , as normal DFT functional cannot account for van der Waals interactions. At the end, I give a description of the density functional tight-binding method (DFTB), an approximation to DFT method, which allows for faster calculation for larger system sizes. A series of models that are derived from Taylor series expansions of the DFT total energies and some approximations of DFTB are also introduced.

3.1 The Solution of the Schrödinger Equation

We will be primarily concerned with the calculation of the ground state energy of a collection of atoms. The energy may be computed by solution of the Schrödinger equation, which, in the time independent, non-relativistic, Born-Oppenheimer approximation (assumption that the motion of atomic nuclei and electrons in a molecule can be separated) reads:

$$\hat{H}\Psi(\mathbf{r}_1,\mathbf{r}_2,\ldots,\mathbf{r}_N) = E\Psi(\mathbf{r}_1,\mathbf{r}_2,\ldots,\mathbf{r}_N). \tag{3.1}$$

The Hamiltonian operator $\hat{H}$ consists of a sum of three terms: the kinetic energy, the interaction with the external potential ($\hat{V}_{\text{ext}}$) and the electron-electron interaction ($\hat{V}_{\text{ee}}$):

$$\hat{H} = -\sum_{i=1}^{N} \frac{1}{2}\nabla_i^2 + \hat{V}_{\text{ext}} + \sum_{i<j}^{N} \frac{1}{|\mathbf{r}_i - \mathbf{r}_j|}. \tag{3.2}$$

In our case the external potential is simply the Coulomb interaction of the electrons with the atomic nuclei;

$$\hat{V}_{\text{ext}} = -\sum_{i=1}^{N} v_{\text{ext}}(\mathbf{r}_i)\,, \tag{3.3}$$

with

$$v_{\text{ext}}(\mathbf{r}_i) = -\sum_{I} \frac{Z_I}{r_{iI}} \qquad \text{and} \qquad \mathbf{r}_{iI} = |\mathbf{r}_i - \mathbf{R}_I|\,. \tag{3.4}$$

Here, $\mathbf{r}_i$ is the coordinate of electron i and the charge on the nucleus at R_I is Z_I. In order to simplify the notation and to focus the discussion on the main features of DFT, the spin index is omitted here and throughout the whole chapter. In principle, Eq. (3.1) can be solved for a set of $\{\Psi\}$ subject to the condition that $\{\Psi\}$ are antisymmetric – they change sign if the coordinates of any two electrons are interchanged. The lowest energy eigenvalue E_0 is the ground state energy and the probability density of finding an electron at $\{\mathbf{r_1}, \cdots, \mathbf{r_N}\}$ is $|\Psi_0|^2$.

The average total energy for a state specified by a particular Ψ, not necessary one of the eigenfunctions of Eq. (3.1), is the expectation value of $\hat{H}$, that is:

$$E[\Psi] = \int \Psi^* \hat{H} \Psi d\mathbf{r} \equiv \langle \Psi | \hat{H} | \Psi \rangle, \tag{3.5}$$

The notation $[\Psi]$ emphasizes the fact that the energy is a *functional* of the wavefunction. The energy in Eq. (3.1) is higher than that of the ground state, unless Ψ corresponds to Ψ_0 – which gives the *variational theorem*:

$$E[\Psi] \geq E_0. \tag{3.6}$$

The ground state wave function and energy may be found by searching all possible wave functions for the one that minimizes the total energy. The Hartree-Fock theory consists of an

ansatz for the structure of Ψ - it is assumed to be an antisymmetric product of functions $\{\varphi_i\}$ which depend on the coordinates of a single electron, that is:

$$\Psi_{\mathrm{HF}} = \frac{1}{\sqrt{N!}} det[\varphi_1(\mathbf{r_1})\varphi_2(\mathbf{r_2})\varphi_3(\mathbf{r_3})\cdots\varphi_N(\mathbf{r_N})] \tag{3.7}$$

where, *det* indicates a matrix determinant. Substitution of this ansatz for Ψ into the Schrödinger equation results in an expression for the Hartree Fock energy:

$$\begin{aligned} E_{HF} = &\int \varphi_i^*(\mathbf{r})[-\frac{1}{2}\sum_{i=1}^{N}\nabla_i^2 + V_{\mathrm{ext}}]\varphi_i(\mathbf{r})d\mathbf{r} \\ &+\frac{1}{2}\sum_{i,j}^{N}\int \frac{\varphi_i^*(\mathbf{r}_1)\varphi_i(\mathbf{r}_1)\,\varphi_j^*(\mathbf{r}_2)\varphi_j(\mathbf{r}_2)}{|\mathbf{r}_i-\mathbf{r}_j|}\,d\mathbf{r}_1 d\mathbf{r}_2 \\ &-\frac{1}{2}\sum_{i,j}^{N}\int \frac{\varphi_i^*(\mathbf{r}_1)\varphi_j(\mathbf{r}_1)\varphi_i(\mathbf{r}_2)\varphi_j^*(\mathbf{r}_2)}{|\mathbf{r}_i-\mathbf{r}_j|}\,d\mathbf{r}_1 d\mathbf{r}_2 \end{aligned} \tag{3.8}$$

The second term is simply the classical Coulomb energy written in terms of the orbitals and the third term is the *exchange* energy. The ground state orbitals are determined by applying the variational theorem to the energy expression in Eq. (3.8) under the constraint that the orbitals are orthonormal. This leads to the Hartree-Fock or SCF (self-consistent functional) equations:

$$\left[-\frac{1}{2}\nabla^2 + V_{\mathrm{ext}}(\mathbf{r}) + \int \frac{\mathrm{n}(\mathbf{r}')}{|\mathbf{r}-\mathbf{r}'|}d\mathbf{r}'\right]\varphi_i(\mathbf{r}) + \int V_{\mathrm{X}}(\mathbf{r},\mathbf{r}')\varphi_i(\mathbf{r}')d\mathbf{r}' = \varepsilon_i\varphi_1(\mathbf{r}), \tag{3.9}$$

where the non-local exchange potential V_X is such that

$$\int V_{\mathrm{X}}(\mathbf{r},\mathbf{r}')\varphi_i(\mathbf{r}')d\mathbf{r}' = -\sum_{j}^{N}\int \frac{\varphi_j(\mathbf{r})\varphi_j^*(\mathbf{r}')}{|\mathbf{r}-\mathbf{r}'|}\,\varphi_i(\mathbf{r}')d\mathbf{r}'. \tag{3.10}$$

The Hartree-Fock equations describe non-interacting electrons under the influence of a mean field potential consisting of the classical Coulomb potential and a $non-local$ exchange potential. From this starting point better approximations (correlated methods) for Ψ and E_0 are readily obtained, but the computational cost of such improvements is very high and scales prohibitively quickly with the number of electrons treated (for an excellent introduction see Ref. [87]). In addition, accurate solutions require a very flexible description of spatial variation of the wave function, i.e. a large basis set is required, which also adds to the expense for practical calculations. In other words, it is not possible to solve the Schrödinger equation and determine the "exact" 3N dimensional wavefunctions even for small atomic systems.

3.2 The Hohenberg-Kohn Theorems

For a N-electron system with a non-degenerate ground state, in 1964 Hohenberg and Kohn proved two theorems [88], which we state below.

Theorem1

For any system of interacting particles in an external potential V_{ext}, the density is uniquely determined. In other words, the external potential is a unique *functional* of the ground state of electron density $n_0(\mathbf{r})$.

To prove this theorem, we use *reductio ad absurdum* in the case of a non-degenerate ground state. Assume that there exist two potentials $V_{ext}^{(1)}$ and $V_{ext}^{(2)}$ that differ by more than a constant, producing the same ground state density $n_0(\mathbf{r})$. Each potential has its own Hamiltonian, $H_{ext}^{(1)}$ and $H_{ext}^{(2)}$, and wavefunctions $\Psi_{ext}^{(1)}$ and $\Psi_{ext}^{(2)}$.

For $H_{ext}^{(1)}$, no wavefunction can give an energy that is less than the energy $E^{(1)}$ associated to $\Psi_{ext}^{(1)}$, according to the variational principle:

$$E^{(1)} = \left\langle \Psi^{(1)} \middle| \hat{H}^{(1)} \middle| \Psi^{(1)} \right\rangle < \left\langle \Psi^{(2)} \middle| \hat{H}^{(1)} \middle| \Psi^{(2)} \right\rangle \tag{3.11}$$

Supposing no degeneracy for the ground state, we can rewrite the expectation value as

$$\left\langle \Psi^{(2)} \middle| \hat{H}^{(1)} \middle| \Psi^{(2)} \right\rangle = \left\langle \Psi^{(2)} \middle| \hat{H}^{(2)} \middle| \Psi^{(2)} \right\rangle + \int d\mathbf{r} \left[V_{ext}^{(1)}(\mathbf{r}) - V_{ext}^{(2)}(\mathbf{r}) \right] n_0(\mathbf{r}) \tag{3.12}$$

Exchanging labels from 1 to 2

$$\left\langle \Psi^{(1)} \middle| \hat{H}^{(2)} \middle| \Psi^{(1)} \right\rangle = \left\langle \Psi^{(1)} \middle| \hat{H}^{(1)} \middle| \Psi^{(1)} \right\rangle + \int d\mathbf{r} \left[V_{ext}^{(2)}(\mathbf{r}) - V_{ext}^{(1)}(\mathbf{r}) \right] n_0(\mathbf{r}) \tag{3.13}$$

Adding Eq. (3.12) and Eq. (3.13), we obtain

$$E^{(1)} + E^{(2)} < E^{(2)} + E^{(1)} \tag{3.14}$$

which is an obvious contradiction. Thus the theorem has been proven by *reductio ad absurdum*.

Theorem2

The total energy $E[n(\mathbf{r})]$ can be defined as a function of density. For any positive definite trial density $n(\mathbf{r})$, with $\int n(\mathbf{r})\, d\mathbf{r} = N$ then:

$$E[n(\mathbf{r})] \geq E_0 \tag{3.15}$$

where E_0 is the ground state energy, which can be obtained by minimizing $E[n(\mathbf{r})]$:

$$E_0 = \min_{\{n\}} E[n(\mathbf{r})]\,. \tag{3.16}$$

Eq. (3.16) also can be written as

$$\delta[E[n(\mathbf{r})] - \mu(\int n(\mathbf{r})d\mathbf{r} - N)] = 0 \tag{3.17}$$

The ground state energy and density correspond to the minimum of the functional $E[n(\mathbf{r})]$ with the normalization of density to the total number of electrons N. μ is the Lagrange multiplier represents the electronic chemical potential.

Since the external potential is uniquely determined by the density, and the potential determines uniquely in turn the ground state wave function, it means that the *Hamiltonian operator* in Eq. (3.2) is *uniquely* determined by the *electron density*. Thus, in principle, all material properties could be uniquely determined by the ground state charge density. For instance, the total energy $E[n(\mathbf{r})]$ including the ion-ion interaction (E_{II}) can be written in the following way:

$$\begin{aligned} E[n(\mathbf{r})] &= \langle\Psi|\hat{T} + \hat{V}_{\mathrm{ext}} + \hat{V}_{\mathrm{ee}}|\Psi\rangle + E_{\mathrm{II}} \\ &= F_{\mathrm{HK}}[n(\mathbf{r})] + \int n(\mathbf{r})\,V_{\mathrm{ext}}(\mathbf{r})d\mathbf{r} + E_{\mathrm{II}} \end{aligned} \tag{3.18}$$

and

$$F_{\mathrm{HK}}[n(\mathbf{r})] = T[n(\mathbf{r})] + V_{\mathrm{ee}}[n(\mathbf{r})] \tag{3.19}$$

The HK functional F is unknown, but it must be a universal functional of only the electron density. Correspondingly, the Hamiltonian can be written as

$$\hat{H} = \hat{F} + \hat{V}_{\mathrm{ext}} \tag{3.20}$$

where $\hat{F}$ is the operator F_{HK} and can be expressed as

$$\hat{F} = \hat{T} + \hat{V}_{\mathrm{ee}} \tag{3.21}$$

Ground state energy is defined by the unique ground state $\mathrm{n}_0(\mathbf{r})$,

$$E_0 = E[n_0] = \langle\Psi_0|\,\hat{H}\,|\Psi_0\rangle \tag{3.22}$$

According to the variational principle, another density $\mathrm{n}_1(\mathbf{r})$ will necessarily produce a higher energy:

$$E_0 = E[n_0] = \langle \Psi_0 | \hat{H} | \Psi_0 \rangle < \langle \Psi_1 | \hat{H} | \Psi_1 \rangle = E_1 = E[n_1] \tag{3.23}$$

3.3 Kohn-Sham Equations

In the Schrödinger equation (Eq. (3.1)) the energy functional contains three terms – the kinetic energy, the interaction with the external potential and the electron-electron interaction:

$$E[n(\mathbf{r})] = T[n(\mathbf{r})] + V_{\mathrm{ext}}[n(\mathbf{r})] + V_{\mathrm{ee}}[n(\mathbf{r})] \tag{3.24}$$

The external potential term can be written as a local functional of the density;

$$V_{\mathrm{ext}}[n(\mathbf{r})] = \int \hat{V}_{\mathrm{ext}}[n(\mathbf{r})] d\mathbf{r} \tag{3.25}$$

Note that the Kinetic $T[n(\mathbf{r})]$ and electron-electron interactions $V_{\mathrm{ee}}[n(\mathbf{r})]$ are difficult to determine, and we need therefore to approximate these functionals. Kohn and Sham [89] induced a fictitious system containing N non-interacting electrons ($V_{\mathrm{ee}} = 0$). For the non-interaction system, the many-body ground-state wave-function can be described as a Slater determinant of single particle wavefunctions φ_i:

$$\Psi_s(\mathbf{r}_1, \mathbf{r}_2, \ldots, \mathbf{r}_N) = \frac{1}{\sqrt{N!}} \begin{vmatrix} \varphi_1(\mathbf{r}_1) & \varphi_2(\mathbf{r}_1) & \cdots & \varphi_N(\mathbf{r}_1) \\ \varphi_1(\mathbf{r}_2) & \varphi_2(\mathbf{r}_2) & \cdots & \varphi_N(\mathbf{r}_2) \\ \vdots & \vdots & \ddots & \vdots \\ \varphi_1(\mathbf{r}_N) & \varphi_2(\mathbf{r}_N) & \cdots & \varphi_N(\mathbf{r}_N) \end{vmatrix}. \tag{3.26}$$

The kinetic energy can be known exactly as

$$T_s[n] = -\frac{1}{2} \sum_i^N \langle \varphi_i | \nabla^2 | \varphi_i \rangle. \tag{3.27}$$

Here the suffix s emphasizes the kinetic energy of a non-interacting electrons system. The ground state density can be obtained as:

$$n(\mathbf{r}) = \sum_i^N |\varphi_i|^2. \tag{3.28}$$

The construction of the ground state density involves the N lowest occupied orbitals, which can be constructed from an antisymmetric wavefunction.

Now we turn our attention again to the interacting system. A contribution to the electron-electron interaction is the classical Coulomb interaction – i.e. the Hartree energy, which is simply the second term of Eq. (3.8) written as the functional of density:

$$V_{\mathrm{H}}[n(\mathbf{r})] = \frac{1}{2}\int\int \frac{n(\mathbf{r_1})n(\mathbf{r_2})}{|\mathbf{r_1}-\mathbf{r_2}|} d\mathbf{r_1} d\mathbf{r_2}, \tag{3.29}$$

Correspondingly, the energy functional can be written as:

$$E[n] = T_s[n] + V_{\mathrm{ext}}[n] + V_{\mathrm{H}}[n] + E_{\mathrm{xc}}[n], \tag{3.30}$$

where E_{xc} is the $exchange - correlation$ functional:

$$E_{\mathrm{xc}}[n] = (T[n] - T_s[n]) + (V_{\mathrm{ee}}[n] - V_{\mathrm{H}}[n]). \tag{3.31}$$

Eq. (3.30) is built explicitly in terms of the density of non-interacting orbitals (see Eq. (3.28)). When applying the variational theorem, we obtain:

$$\left[-\frac{1}{2}\nabla^2 + V_{\mathrm{ext}}(\mathbf{r}) + \int \frac{n(\mathbf{r}')}{|\mathbf{r}-\mathbf{r}'|} d\mathbf{r}' + V_{\mathrm{xc}}(\mathbf{r})\right] \varphi_i(\mathbf{r}) = \varepsilon_i \varphi_i(\mathbf{r}). \tag{3.32}$$

We here introduced the *exchange-correlation*, potential defined as:

$$V_{\mathrm{xc}}(\mathbf{r}) = \frac{\delta E_{\mathrm{xc}}[n]}{\delta n}. \tag{3.33}$$

This set of non-linear equations, known as Kohn-Sham equations, describes the behavior of non-interacting electrons in an effective local potential. If the local *exchange-correlation potential* is known, the "orbitals" will generate the exact ground state density and exact ground state energy. Even if the exact V_{xc} is unknown, a number of excellent approximations have been developed. Thus, the quality of the theory rests on the approximation chosen for E_{xc}.

3.4 Exchange-Correlation functionals

This section will roughly introduce the history of the development of the two mostly used exchange-correlation functionals, the local-density approximation (LDA) and the generalized gradient approximation (GGA).

3.4.1 LDA

The first and most important approximation for the development of DFT is the local-density approximation (LDA) [90]. LDA is an approximation that only depends on the value of the electronic density of each point of space. First, we need to understand the non-interacting kinetic energy $T_s[n]$ in the Thomas-Fermi approximation.

In a homogeneous system, the kinetic energy of per volume is

$$t_s^{hom}(n) = \frac{3\hbar^2}{10m}(3\pi^2)^{2/3}n^{5/3}, \tag{3.34}$$

where $n = const$. But for inhomogeneous system, $n = n(\mathbf{r})$, in the local approximation

$$t_s(\mathbf{r}) \approx t_s^{hom}(n(\mathbf{r})) = \frac{3\hbar^2}{10m}(3\pi^2)^{2/3}n(\mathbf{r})^{5/3}, \tag{3.35}$$

and the full kinetic energy

$$T_s^{LDA} = \int d^3r t_s^{hom}(n(\mathbf{r})) = \frac{3\hbar^2}{10m}(3\pi^2)^{2/3}\int d^3r n(\mathbf{r})^{5/3}. \tag{3.36}$$

The same approximation and procedure can also be applied for the exchange-correlation energy E_{xc}. The exchange energy per unit volume of homogeneous electron gas is exactly known [91]:

$$e_x^{hom}(n) = -\frac{3q^2}{4}(\frac{3}{\pi})^{1/3}n^{4/3}. \tag{3.37}$$

As

$$E_{xc} = \int d\mathbf{r} n(\mathbf{r})\varepsilon_{xc}(n(\mathbf{r})), \tag{3.38}$$

where $n(\mathbf{r})$ is the electronic density and ε_{xc} is the exchange-correlation energy per particle, we define:

$$E_x^{LDA}[n] = -\frac{3q^2}{4}(\frac{3}{\pi})^{1/3}\int n(\mathbf{r})^{4/3}d\mathbf{r}. \tag{3.39}$$

This is the E_x of LDA. While, for the correlation energy E_c, it is much more complicated without knowing the analytic expression $e_c^{hom}(n)$. In the early times, the perturbation theory was adopted to approximate $e_c^{hom}(n)$ [91]. Nowadays, this method is replaced by using precise Quantum Monte Carlo (QMC) simulations and parameterizing $e_c^{hom}(n)$ functionals from these data [92].

Independently of the parametrization, the $E_xc[n]$ of LDA [90] is

$$E_{xc}[n] \approx E_{xc}^{LDA} = \int e_{xc}^{hom}(n) d\mathbf{r}|_{n\to n(\mathbf{r})} = \int e_{xc}^{hom}(n(\mathbf{r})) d\mathbf{r}, \tag{3.40}$$

where $e_{xc}^{hom} = e_x^{hom} + e_c^{hom}$.

This approximation for E_{xc} has been greatly successful. One possible explanation is that LDA underestimates E_c but overestimates E_x, leading to systematic error cancellation. Moreover, LDA exactly satisfies the sum rule $\int d\mathbf{r} n_{xc}(\mathbf{r},\mathbf{r}') = -1$ [93]. The LDA can calculate rather accurate bond lengths and lattice constants, but it seriously overestimate atomization energies of molecules and solid.

3.4.2 GGA

In LDA, the correlation energy only depends on the density at a specific point. For any real system, the density is inhomogeneous and it is possible to include information on the rate of the density variation of the functional. The first attempt was the 'gradient-expansion approximation' (GEA). It tried to include gradient-dependent terms $|\nabla n(\mathbf{r})|$, $|\nabla n(\mathbf{r})|^2$, $\nabla^2 n(\mathbf{r})$, etc., in the energy functional. This leads for the kinetic energy term to

$$T_s[n] \approx T_s^W[n] = T_s^{LDA}[n] + \frac{\hbar^2}{8m}\int d^3r \frac{|\nabla n(\mathbf{r})|^2}{n(\mathbf{r})}, \tag{3.41}$$

The integral term is called the von Weizsäker term [94] and the E_x for GEA approximately equals

$$E_x[n] \approx E_x^{GEA}[n] = E_x^{LDA}[n] - \frac{10q^2}{432\pi(3\pi^2)^{1/3}}\int d^3r \frac{|\nabla n(\mathbf{r})|^2}{n(\mathbf{r})^{4/3}}. \tag{3.42}$$

The integral term is the lowest-order gradient correction for the $E_x^{GEA}[n]$. In fact, when introducing the low-order gradient corrections, we don't improve the LDA as expected, and we can even get worse results. We note that it is more difficult to introduce higher-order gradient corrections. In this case, the solution was the development of the generalized gradient approximation (GGA). Instead of higher-order gradient expansion terms, one considers more in general functions of $n(\mathbf{r})$ and $\nabla n(\mathbf{r})$ [95]:

$$E_x^{GGA}[n] = \int d^3r f(n(\mathbf{r}), \nabla n(\mathbf{r})). \tag{3.43}$$

There exist many different GGA functionals, depending on different choices of the function $f(n,\nabla n)$. Among the most popular GGAs we find B88 [96] and PBE [95]:

$$E_x^{B88} = -\sum_{\sigma=\alpha,\beta}\int n\sigma^{4/3}\left[\frac{3}{4}(\frac{6}{\pi}^{1/3} + \frac{\beta x_\sigma^2}{1+6\beta x_\sigma sinh^{-1}x_\sigma}\right]d\mathbf{r}, \tag{3.44}$$

$$E_x^{PBE} = -\int n^{4/3}\left[\frac{3}{4}(\frac{3}{\pi})^{1/3} + \frac{\mu s^2}{1+\mu s^2/\kappa}\right]d\mathbf{r}. \tag{3.45}$$

where $x = |\nabla n|/n^{4/3}$. GGA improves on atomization and cohesive energies for molecules and solids [97], however, there still exist problems. GGA almost always overestimates the lattice constants of solids, while LDA usually underestimates them. Another problem is that LDA and GGA cannot predict the quasiparticle band gap correctly. Consistently, the band gap is strongly underestimated for most semiconductors and insulators. Furthermore, common GGA and LDA do not account for van der Waals interactions.

3.5 Van der Waals functionals in density functional theory

Van der Waals (vdW) forces refer to attraction and repulsions between atoms, molecules, and surfaces which are not due to covalent and ionic bonds. These interactions include dipole-dipole, dipole-induced dipole, and instantaneous dipole-induced dipole forces (also called London dispersion force). The London dispersion force is an attractive force arising from non-local electron correlation. Van der Waals density functional (vdW-DF) [98] was developed to include this kind of interaction. The correlation energy in the density functional theory can be divided into two pieces, local density approximation LDA, and a nonlocal (nl) part E_c^{nl}

$$E_c[n] = E_c^0[n] + E_c^{nl}[n], \tag{3.46}$$

where the $E_c^0[n]$ is taken approximately equal to E_c^{LDA}. The second term is treated in the full potential approximation:

$$E_c^{nl}[n] = \int_0^\infty \frac{du}{2\pi} Tr[ln(1-V\tilde{\chi}) - ln\varepsilon] \tag{3.47}$$

where $\tilde{\chi}$ is the fully self-consistent density response to a potential. V is the Coulomb interaction, ε is an approximate dielectric function and u is the imaginary frequency [98]. Calculations usually use the self-consistent charge density from Perdew-Burke-Ernzerhof

(PBE) or revised PBE (revPBE) functionals. Eq. (3.47) can be expanded to second order in $S \equiv 1 - \varepsilon^{-1}$ as:

$$E_c^{nl}[n] \approx \int_0^\infty \frac{du}{4\pi} Tr\left[S^2 - \left(\frac{\nabla S \cdot \nabla V}{4\pi e^2}\right)\right]. \tag{3.48}$$

To approximate S, one can be inspired by the plasmon-pole model [99] and obtain

$$S_{\mathbf{q},\mathbf{q}'} = \frac{1}{2}[\tilde{S}_{\mathbf{q},\mathbf{q}'} + \tilde{S}_{-\mathbf{q},-\mathbf{q}'}], \tag{3.49}$$

where

$$\tilde{S}_{\mathbf{q},\mathbf{q}'} = \int d^3 r e^{-i(\mathbf{q}-\mathbf{q}')\cdot\mathbf{r}} \frac{4\pi n(\mathbf{r}) e^2/m}{[\omega + \omega_q(\mathbf{r})][-\omega + \omega'_q(\mathbf{r})]}. \tag{3.50}$$

In Eq. (3.50), $\omega(\mathbf{r})$ is a function of the local density and its gradient at the point $\mathbf{r}$, which we will choose. Here the form we use is

$$\omega_q(\mathbf{r}) = \frac{q^2}{2m} \frac{1}{h[q/q_0(\mathbf{r})]} \tag{3.51}$$

define $q_0^2 = \gamma/l^2$, and $\gamma = 4\pi/9$ and $h(y) = 1 - e^{-\gamma y^2}$. The choice of $\omega(\mathbf{r})$ functional is somewhat arbitrary. Here, it depends on a single length scale l, resulting in ω_q values in the range from $1/2ml^2$ to $q^2/2m$. Finally, with this choice, we define the exchange-correlation energy as

$$E_{xc}^0 = \int d^3 r \varepsilon_{xc}^0(\mathbf{r}) n(\mathbf{r}) \approx \int_0^\infty \frac{du}{2\pi} Tr(ln\varepsilon) - E_{self} \approx \int_0^\infty \frac{du}{2\pi} TrS - E_{self}, \tag{3.52}$$

where E_{self} is the internal Coulomb self-energy of each electron. Introducing the approximation from Eq. (3.50), we obtain the exchange correlation energy density

$$\varepsilon_{xc}^0(\mathbf{r}) = \frac{e^2 q_0(\mathbf{r})}{\pi} \int_0^\infty dy[h(y) - 1] = -\frac{3e^2}{4\pi} q_0(\mathbf{r}) \tag{3.53}$$

and

$$q_0(\mathbf{r}) = \frac{\varepsilon_{xc}^0(\mathbf{r})}{\varepsilon_x^{LDA}(\mathbf{r})} k_F(\mathbf{r}), \tag{3.54}$$

with k_F the Fermi wave vector and LDA exchange value ε_x^{LDA} are

$$k_F = (3\pi^2 n)^{1/3}, \qquad \varepsilon_x^{LDA} = -\frac{3}{4} e^2 (\frac{3n}{\pi})^{1/3}, \tag{3.55}$$

and with

$$\varepsilon_{xc}^{0} \approx \varepsilon_{xc}^{LDA} - \varepsilon_{x}^{LDA}\left[\frac{Z_{ab}}{9}\left(\frac{\nabla n}{2k_F n}\right)^2\right]. \tag{3.56}$$

Here $Z_{ab} = -0.8491$ is defined as the "screened exchange" parameter [100].

Finally, the E_c^{nl} in a plane-wave representation is

$$E_c^{nl} = \frac{1}{2}\int\int d^3r d^3r' n(\mathbf{r})\phi(\mathbf{r},\mathbf{r}')n(\mathbf{r}'), \tag{3.57}$$

where ϕ, the integration kernel, is given by

$$\phi(\mathbf{r},\mathbf{r}') = \frac{2me^4}{\pi^2}\int_0^\infty a^2 da \int_0^\infty b^2 db W(a,b) \times T(\nu(a),\nu(b),\nu'(a),\nu'(b)), \tag{3.58}$$

and

$$\begin{aligned} W(a,b) = 2[&(3-a^2)b\cos b\sin a + (3-b^2)a\cos a\sin b \\ &+ (a^2+b^2-3)\sin a\sin b - 3ab\cos a\cos b]/a^3b^3, \end{aligned} \tag{3.59}$$

$$T(w,x,y,z) = \frac{1}{2}\left[\frac{1}{w+x}+\frac{1}{y+z}\right]\left[\frac{1}{(w+y)(x+z)}+\frac{1}{(w+z)(y+x)}\right], \tag{3.60}$$

$$\begin{aligned} \nu(y) &= y^2/2h(y/d), \\ \nu'(y) &= y^2/2h(y/d'), \end{aligned} \tag{3.61}$$

with

$$\begin{aligned} d &= |\mathbf{r}-\mathbf{r}'|q_0(\mathbf{r}), \\ d' &= |\mathbf{r}-\mathbf{r}'|q_0(\mathbf{r}'). \end{aligned} \tag{3.62}$$

Obviously, ϕ in Eq. (3.58) depends on $\mathbf{r}$ and $\mathbf{r}'$ only through d and d'. We can define d and d' as the sum and difference of the variables D and δ: $d = D(1+\delta)$ and $d' = D(1-\delta)$. With the value $0 \le D < \infty$ and $0 \le |\delta| < 1$, for large d and d'

$$\phi \to -\frac{C}{d^2 d'^2(d^2+d')} \tag{3.63}$$

where $C = 12(4\pi/9)^3 me^4$ and ϕ has the r^{-6} asymptotic dependence. In conclusion, the form of the exchange correlation energy for vdW [98] consists of the exchange energy E_x^{GGA} through the GGA approximations and correlation energy E_c^{LDA} and a nonlocal (nl) part E_c^{nl} given by Eq (3.57). The vdW functional has been applied successfully to a variety of systems,

in particular, molecules adsorbed on surfaces, molecular solids, and layered solids [101–103]. However, the double spatial integral Eq. (3.57) leads to prohibitive computational request for large systems. To solve this problem, Román-Pérez and Soler [104] simplified Eq. (3.57) by fixing some parameters. Thus, ϕ can be interpolated as

$$\phi_0(\mathbf{r},\mathbf{r}') \approx \sum_{\alpha\beta} \phi_0(q_\alpha, q_\beta, |\mathbf{r}-\mathbf{r}'|) p_\alpha(q_0(\mathbf{r})) p_\beta(q_0(\mathbf{r}')), \tag{3.64}$$

where q_α are fixed values which are chosen to give a good ϕ, and p_α is a cubic spline. Correspondingly, the original non-local functional can be expressed as

$$\begin{aligned} E_c^{nl} &= \frac{1}{2}\sum_{\alpha\beta} \int d^3r d^3r' \theta_\alpha(\mathbf{r}) \phi_{\alpha\beta}(|\mathbf{r}-\mathbf{r}'|) \theta_\beta(\mathbf{r}') \\ &= \frac{1}{2}\sum_{\alpha\beta} \int d^3k \theta^*_\alpha(\mathbf{k}) \phi_{\alpha\beta}(k) \theta_\beta(\mathbf{k}'). \end{aligned} \tag{3.65}$$

Here $\theta_\alpha(\mathbf{r}) = n(\mathbf{r}) p_\alpha(q_0(n(\mathbf{r}), \nabla n(\mathbf{r})))$. $\theta_\alpha(\mathbf{k})$ is Fourier transform of $\theta_\alpha(\mathbf{r})$ and $\phi_{\alpha\beta}(k)$ is the Fourier transform of $\phi_{\alpha\beta}(r) \equiv \phi(q_\alpha, q_\beta, |\mathbf{r}-\mathbf{r}'|)$.

With this factorization of the integration kernel ϕ plus the fast Fourier transforms, a six-dimensional integral is simplified as three-dimensional. The vdW self-consistent potential, total energy and atomic forces can be quickly evaluated with a $O(NlogN)$ algorithm [104], where N is the number of atoms in the system.

This implementation is successful for first-principles calculations of large systems. Nowadays, the current vdW-DF calculations for large systems with this method have a negligible time difference if compared with standard GGA calculation [104].

In this thesis, we use the vdW-optB88 method [101], which applies the optB88 exchange functional which has two parameters fit to the S22 dataset [105] (a set of 22 weakly interacting dimers mostly of biological importance). This method has been proven successfully to obtain accurate lattice constants, bulk moduli and atomization energy of solids [102].

3.6 Density Functional Tight-Binding Method

DFT is a very successful method for accurate and efficient calculations of physical and chemical properties in most systems. However, faster but more approximate methods are still required for larger systems. For instance, molecular mechanics with classical force field methods can be several orders of magnitude faster than DFT and allowing calculations of thousands to millions of atoms in a nanosecond time scale. Such classical molecular dynamics force field contains a large number of empirical parameters and can be very accurate

for specific system on which the parameters were fitted, but with a limited transferability for other new systems.

The density functional based tight-binding (DFTB) method [106, 107] combines computational efficiency and transferability, because its parametrization is mainly related to DFT calculations. Based on DFT calculations, which guarantee a large transferability, it has been applied to large molecules, clusters, nanostructures and and condensed-matter systems with a wide range of elements. The energy functional is derived directly from the expectation value of the Kohn-Sham hamiltonian (Eq. (3.32)):

$$E[n] = \sum_i^N \langle \varphi_i | -\frac{\nabla^2}{2} + v_{\text{ext}}(\mathbf{r}) + v_{\text{H}}[n](\mathbf{r}) + v_{\text{xc}}[n](\mathbf{r}) | \varphi_i \rangle + E_{\text{II}}, \tag{3.66}$$

where E_{II} is the ion–ion interaction energy. For clarity, first, we simplified the notation $\int d\mathbf{r} \to \int$, $\int d\mathbf{r}' \to \int'$, $[n(\mathbf{r})] \to [n]$ and $[n(\mathbf{r}')] \to [n']$. Next we need to approximate: we consider the true charge density $n(\mathbf{r}) = n_0(\mathbf{r}) + \delta n(\mathbf{r})$, where $n(\mathbf{r})$ is composed of atomic densities and $\delta n(\mathbf{r})$ is a small charge fluctuation. With this notation and simplification, we expand $E[n]$ at $n_0(\mathbf{r})$ to second order in the fluctuation $\delta n(\mathbf{r})$ as;

$$\begin{aligned} E[\delta n] \approx & \sum_i^N \langle \varphi_i | -\frac{\nabla^2}{2} + v_{\text{ext}}(\mathbf{r}) + \frac{1}{2}\int' \frac{n_0'}{|\mathbf{r}-\mathbf{r}'|} + v_{\text{xc}}[n_0] | \varphi_i \rangle \\ & - \frac{1}{2}\int\int' \frac{n_0' n_0}{|\mathbf{r}-\mathbf{r}'|} + E_{\text{xc}}[n_0] - \int v_{\text{xc}}[n_0] n_0 + E_{\text{II}} \\ & + \frac{1}{2}\int\int' \left(\frac{1}{|\mathbf{r}-\mathbf{r}'|} + \left.\frac{\delta^2 E_{\text{xc}}}{\delta n \delta n'}\right|_{n_0} \right) \delta n \delta n' \, . \end{aligned} \tag{3.67}$$

The first line of Eq. (3.67) is the band-structure energy, E_{BS}. It is usually written in a compact form as

$$E_{\text{BS}} = \sum_i^N \langle \varphi_i | \hat{H}[n_0] | \varphi_i \rangle \, . \tag{3.68}$$

The second line is called the repulsive energy, E_{rep}, mainly from the ion–ion repulsion term E_{II} and last line is called E_{coul} mainly from the Coulomb interaction but with exchange and correlation contributions as well. $E_{\text{xc}}[n_0]$ is a complicated term which we can deal with as it is done in DFT: we put the most difficult physics here and approximate it with a sum of terms over atom pairs, because each term only depends on elements and their distance, then the repulsive energy can be approximated as

$$E_{\text{rep}} = \sum_{I<J} V_{\text{rep}}^{IJ}(\mathbf{R}_{IJ}) \, . \tag{3.69}$$

We have to note that the repulsive functions $V_{\text{rep}}^{IJ}(\mathbf{R})$ are obtained by fitting to large amount of DFT calculations.

Finally we need to approximate E_{coul}. In fact, for the standard DFTB model without self-consistency [108], this term is simplify neglected. Therefore, the calculations of the total energy do not depend on the electronic-density fluctuations δn, and accordingly, it doesn't have to be interactively calculated. However, this term has to be involved when the chemical bonds in the system are controlled by a more delicate charge balance between atoms, i.e. heteronuclear molecules and polar semiconductors. In order to include the density fluctuation effect in a simple yet efficient way, we can decompose $\delta n(\mathbf{r})$ in the superposition of normalized atom contribution δn_I [109]:

$$\delta n = \sum_I \Delta q_I \delta n_I \ , \tag{3.70}$$

with the extra electron population on atom I

$$\Delta q_I \approx \int_{V_I} \delta n \ . \tag{3.71}$$

and $\int_{V_I} \delta n_I = 1$.
The charge fluctuation interactions can be written as

$$E_{\text{coul}} = \frac{1}{2} \sum_{IJ} \gamma_{IJ}(R_{IJ}) \Delta q_I \Delta q_J \ , \tag{3.72}$$

where

$$\gamma_{IJ}(R_{IJ}) = \begin{cases} U_1, & I = J \\ \frac{erf(C_{IJ} R_{IJ})}{R_{IJ}}, & I \neq J \end{cases} \tag{3.73}$$

γ_{IJ} only depends on the distance R_{IJ} and the Hubbard parameters U_I and U_J.

Now, we expand the single-particle wave-functions φ_i using a minimal local basis, which means having only one radial function for each angular momentum state: one for s-states, three for p-states, five for d-states, and so on;

$$\varphi_i(\mathbf{r}) = \sum_\mu c_\mu^i \phi_\mu(\mathbf{r}) \ . \tag{3.74}$$

with this expansion, the final DFTB energy expression (Eq. (3.67)) can be written as;

$$E = \sum_i \sum_{\mu\upsilon} c_\mu^{i*} c_\upsilon^i H_{\mu\upsilon}^0 + \frac{1}{2} \sum_{IJ} \gamma_{IJ}(\mathbf{R}_{IJ}) \Delta q_I \Delta q_J + \sum_{I<J} V_{\text{rep}}^{IJ}(\mathbf{R}_{IJ}) \ . \tag{3.75}$$

By variations of $\delta(E - \sum_i \varepsilon_i \langle \varphi_i | \varphi_i \rangle)$, where ε_i is Lagrange multipliers, we obtain

$$\sum_{\mu}^{M} c_{\mu}^{i}(H_{\mu\upsilon} - \varepsilon^{i} S_{\mu\upsilon}) = 0, \quad \forall\, \upsilon, i \tag{3.76}$$

with

$$\begin{aligned} H_{\mu\upsilon} &= H^{0}_{\mu\upsilon} + \frac{1}{2} S_{\mu\upsilon} \sum_{K} (\gamma_{IK} + \gamma_{JK}) \Delta q_K, \\ &= H^{0}_{\mu\upsilon} + H^{1}_{\mu\upsilon}\ , \end{aligned} \tag{3.77}$$

here

$$S_{\mu\upsilon} = \left\langle \varphi_{\mu} \middle|\ \varphi_{\upsilon} \right\rangle, \quad H^{0}_{\mu\upsilon} = \left\langle \varphi_{\mu} \middle| H^{0} \middle| \varphi_{\upsilon} \right\rangle \quad \forall\ \mu \in I,\ \upsilon \in J\ . \tag{3.78}$$

Now we discuss how to calculate the matrix elements $S_{\mu\upsilon}$ and $H^{0}_{\mu\upsilon}$. First we construct the minimal basis functions φ_{μ} in the Eq. (3.74) as:

$$\varphi_{\mu}(\mathbf{r}') = \mathbf{R}_{\mu}(\mathbf{r}) \tilde{Y}_{\mu}(\theta, \varphi) (\mathbf{r}' = \mathbf{R}_I + \mathbf{r}, \mu \in I) \tag{3.79}$$

with real spherical functions $\tilde{Y}_{\mu}(\theta, \varphi)$ which should strongly represent bound electrons of a solid or molecules in our simulating systems. The orbitals thus cannot come from free atoms, as they would be too diffuse. For this purpose, we adopt the orbitals from a pseudo-atom, where we add an additional confinement potential V_{conf} into the Hamiltonian. The pseudo-atom is calculated with DFT only once for this confined potential. Once we get the localized basis functions φ_{μ}, the $S_{\mu\upsilon}$ and $H^{0}_{\mu\upsilon}$ are calculated and tabulated as a function of the distance between atomic pairs $\mathbf{R}_{IJ}$. Thus, it is not necessary to recalculate any integrals during a geometry optimization or molecular dynamics simulations. In the beginning part of our work in this thesis, we perform the DFTB calculations using DFTB+ software package [110]. The *ab initio* DFT calculations part as implemented in VASP [111] code are also presented at the end.

Chapter 4

Filling and PTM effect on carbon nanotubes collapse

4.1 Introduction

Since their observation in 1991 by Iijima [2], carbon nanotubes (CNTs) have been at the center of a considerable research effort. CNTs can be produced in a large number of diameters and chiralities, they can have a single or multiple walls, they can have their extremities open or closed, be empty or filled with several substances, they can be isolated, dispersed in a solution or in a composite material, appear in bundles, etc [112]. Of course, this remarkable variety allows to tune and engineer the already unique, and highly anisotropic, electronic, mechanical and transport properties of CNTs, making them a cornerstone material for a wealth of possible applications, ranging from electronics to their use as nanoprobes for biological investigations [5]. Among the different applications, CNTs are studied as vessels for host–guest chemistry thanks to their inner cavity which can be filled with different molecular entities. Up to now CNTs have been used as passive nanovessels for chemical reactions or storage capabilities. We propose here to provide CNTs with an active role in the elaboration of novel molecular structures through the control of the geometry of the nanocavity by applying hydrostatic pressure.

Theoretical and experimental studies have shown that CNTs can undergo drastic radial deformations under hydrostatic pressure [65, 66, 82, 113–115], going from a circular cross-section to an oval or polygonal one, and from this to a fully collapsed, peanut-like, shape [114]. The exact details of the collapse process are however still under debate. Several contradicting values for the collapse pressure of CNTs have been obtained experimentally. The source of such discrepancies probably resides in the interactions with the pressure transmitting

medium [14, 15]. On the other hand, theoretical calculations show that the chirality has only a small effect on the collapse pressure P_c, which is mainly determined, for single-wall tubes, by the tube diameter [65, 66, 82] (going as $P_c \sim 1/d^3$, where d is the diameter of the tube). Furthermore, the electronic structure of CNTs is strongly dependent not only on its chirality but also on the modification of its radial cross-section geometry [116–123], which can be affected by external forces like van der Waals interactions with a surface [124, 125] or hybridization with an interface [126].

In the rest of this Chapter, we will first focus on the theoretical study of the effect of high-pressure in the nano-confinement of molecular systems inside isolated CNTs. In particular we are interested in the effect of the nanotube radial collapse, which imposes extremely anisotropic constrains to the filling material. We will consider two guest molecules, namely H_2O and CO_2. Afterwards, we will examine the effect of different pressure transmitting medium (PTM) on the collapse of empty CNTs, considering in water, CO_2 and argon environment.

We chose to apply the density-functional based tight-binding method (DFTB) [107, 107] introduced in Chapter 2. The DFTB balances the precision problem of classical potentials and calculation complexity of density-functional theory. Thus, it has the advantage of being considerably faster than a standard density-functional theory (DFT) calculation, but at the same time it retains much of the accuracy of this latter theory. Moreover, and as it is a fully quantum approach, it can describe reliably the different hybridization states of carbon, and in particular the increase/reduction of sp^3 content during the collapse process. This method was successfully applied for carbon in previous works [65, 107, 127–129]. We will adopt therefore the same parameters [65].

4.2 Nanostructured molecules inside collapsing filled nanotubes

We will deal with the collapse process of CNTs which encapsulate a molecular “foreign material”. In fact, we can fill CNTs with several guest molecules, such as argon [9, 130–134], neon [134], helium [132], fullerenes [14, 135], water [14–17, 20–22, 135–149], etc. The effect of the filling is two-fold. On the one hand, guest compounds can differ significantly from bulk matter [20–22, 139] due to the strong bilateral confinement at the nanometer scale. Moreover, the behavior and properties of the inclusion compound can be strongly influenced by the tube diameter [147, 150]. On the other hand, guest molecules can also influence the electronic and mechanical properties of the host CNTs [14, 23, 135]. For example, recent

experimental studies demonstrated that water filling can increase substantially the collapse pressure of CNTs [15], while the structure of enclosed C_{60} [151], C_{70} [14] or iodine [10] can be modified by the tube radial cross-section evolution.

A particularly interesting example is given by water filling. Theoretical calculations have shown that, for small diameter nanotubes ($0.54 < d < 0.811$ nm) encapsulated water cannot move freely and forms a single-file water structure [147, 152]. This fact was experimentally confirmed using Raman spectroscopy by Cambré *et al.* [16] who observed the single-file water chain down to a (5,3) CNT (with a diameter of 0.548 nm). For larger tubes the situation is considerably more complicated. Noon *et al.* [22] and Liu *et al.* [141] found that water molecules form a very ordered spiral-like chain along the CNT axis. On the other hand, Koga *et al.* [21] found n-membered rings of water inside CNTs under pressure (in the range 0.05–0.5 GPa), where the n value depends on the diameter of the tube. Similar structures were also found inside a (9,9) CNT by Mashl *et al.* [143] Furthermore Shiomi *et al.* [153] and Wang *et al.* [147] found that ice-like structures formed inside CNTs. Finally, Paineau *et al.* [154] discovered in X-ray scattering experiments that the structure of water in CNTs depends on its percentage in mass: if the water content is larger than 5% in mass, water filling is no more homogeneous and the molecules form 3 layers [154]. Also closely related is a recent outstanding experiment reporting a novel form of water, named “square ice”, formed between two layers of graphene due to nano-confinement [136], although this finding has already been questioned [155].

All these studies were performed either at ambient conditions or at very low pressure. High pressures, on the other hand, is a much less explored subject, even if it is well know that pressure can affect considerably the structural properties of materials.

Our simulations of the collapse of empty and filled CNTs were performed using the density-functional tight-binding (DFTB) technique, as implemented in the DFTB+ software package [110]. DFTB has the advantage of being considerably faster than a standard density-functional theory (DFT) calculation, retaining at the same time much of the accuracy of this latter theory. Moreover, as it is a fully quantum approach, it has no problem to describe the different hybridization states of carbon, and in particular the modification of sp^3 content during the collapse process. The parameters describing the carbon-carbon interaction were taken from the matsci-0-3 set [156], while the rest of the parameters were taken from the mio-1-1 set [108]. In order to account for possible charge transfer processes we used the self-consistent charge DFTB scheme [108]. Concerning the validation of the parameters, the carbon-carbon Slater-Koster parameters we used have been extensively applied for the study of CNTs since at least 2003 [157]. We recently used these parameters to study the collapse of bundles of single-wall/ CNTs [65]. The parameters required to describe water

have also been extensively tested [158, 159]. The excellent agreement that we find in the present work on the evolution of the CNT collapse pressure in empty and water filled CNTs with the experimental work of Ref. [15] further validates our set of parameters.

We carried out our simulations using a periodic hexagonal supercell containing 4 (10,10) CNTs (d=1.36 nm, 160 carbon atoms). The *a* and *b* lattice constants are chosen such that tubes are separated by at least 10 Å in order to minimize interactions between neighbors. The tubes are surrounded with enough water (200 molecules) or CO_2 (150 molecules) to fill the unit cell. Moreover, we consider the inclusion of guest molecules inside the CNT, exploring a range of concentration from 3% to 40%, which covers the experimental range. All the starting cells are first thermalized at 370 K, and then rapidly quenched to 10 K. Finally, individual atomic positions and cell vectors are fully optimized until all forces are smaller than 10^{-4} Ha/Bohr. From these starting geometries, we then perform quasi-static simulations by increasing the pressure in small steps of 0.2 GPa up to 15 GPa, unless the tube collapses before. At each pressure step the geometry is again fully optimized. We remark that high temperature may help CNTs to overcome energy barriers leading to a plastic collapse [160], however we want to focus here on the effect of hydrostatic pressure and we will therefore disregard temperature effects.

The electronic structures were then analyzed with DFT as implemented in the Vienna ab initio Simulation Package (VASP) code [111]. We used the Perdew–Burke–Ernzerhof [95] approximation to the exchange correlation, a plane wave energy cutoff of 700 eV and $2\times2\times3$ k-meshes.

Before discussing our results, it is worthwhile defining how to calculate the volume of deformed CNTs. The critical point is to calculate the area of the cross-section. To this end we project all the positions of carbon atoms on a plane perpendicular to the axis. Second, we delete atoms with the same projected positions (within a small tolerance distance). Then, we choose one reference point on the plane (for example outside the tube) and we connect it to all projected atoms. We define in this way a set of ordered vectors v_i with a common end point, and whose other end points draw in the plane a close chain of N points. These vectors divide the plane in triangles. The cross section area of the tube can now be calculated by adding the half of (positive and negative) values of the cross products of all couples of neighboring vectors: $\frac{1}{2}\sum_{i=1}^{N} v_i \times v_{i+1}$ with $v_{N+1} = v_1$. Once we have calculated the cross-section area, the volume can be easily obtained by multiplying it by the length of the tube along its axis.

We study an isolated (10,10) CNT, using either H_2O or CO_2 both as filling and pressure transmitting medium. Experimentally, the water filling of arc-type single-wall CNT [which are comparable in diameter to the (10,10) tube used here] was estimated to be between 11% to 29% of the total weight fraction of fully filled nanotubes [154]. Therefore, to cover the

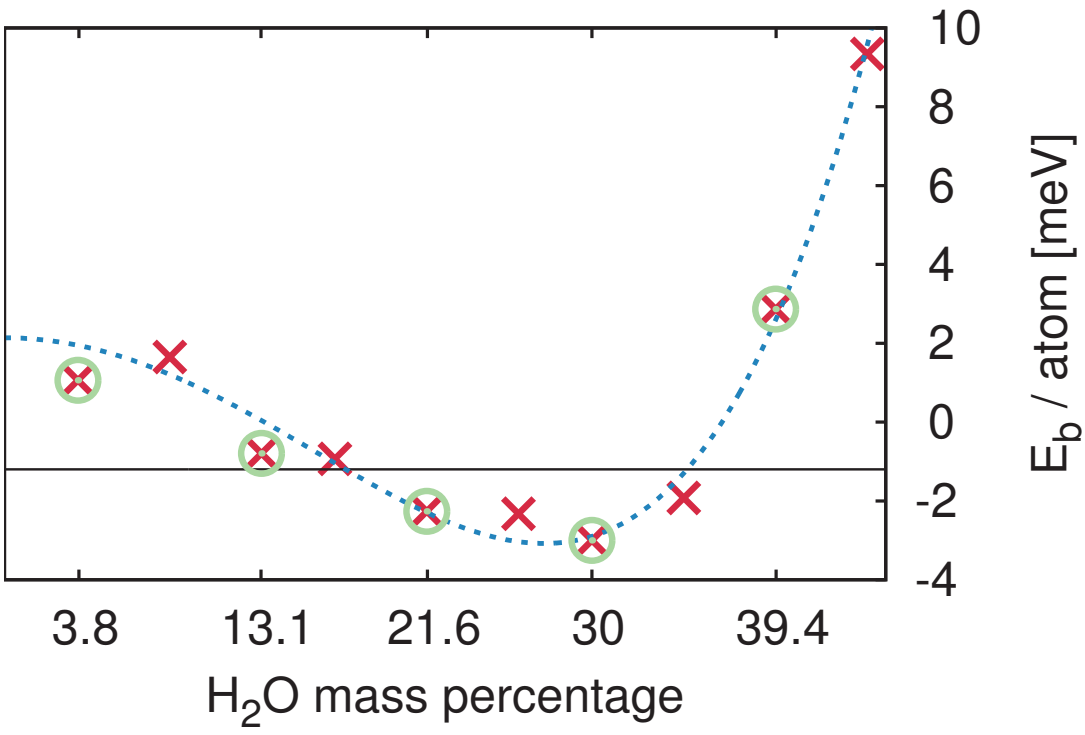

Figure 4.1 Binding energy per atom for the (10,10) nanotubes as a function of the water concentration. Red crosses are filled tubes in vaccum, green circles mark the cases where we also calculated the tube in water.

whole experimental range we studied concentrations of water of 3.8%, 13.1%, 21.6%, 30%, and 39.4%. This corresponds respectively to 4, 14, 23, 32, and 42 molecules of H_2O in our simulation supercells. The binding energies (E_b) of the tubes filled with water were calculated (Fig. 4.1) and compared with experiment [65].

$$E_b = E_{filled} - E_{empty} - E_{H_2O} \times N_{H_2O} \tag{4.1}$$

where E_{filled} is the tube energy filled with N_{H_2O}, E_{empty} is the energy of the empty, isolated tube and E_{H_2O} is the energy of one water molecule. we deduce from Fig. 4.1 that the optimum filling ratio for (10,10) tubes according to our calculation is from 17% to 35%. we remark that, due to finite length (4 unit cell length) of the nanotube, a more precise estimation with longer nanotubes is necessary.

It's time to focus on the effect of water-filling on the collapse. In Fig. 4.2 we plot the volume of the tube (normalized to its volume at zero pressure) as a function of pressure. The volume is calculated as described above. The upper panel contains results for CNTs

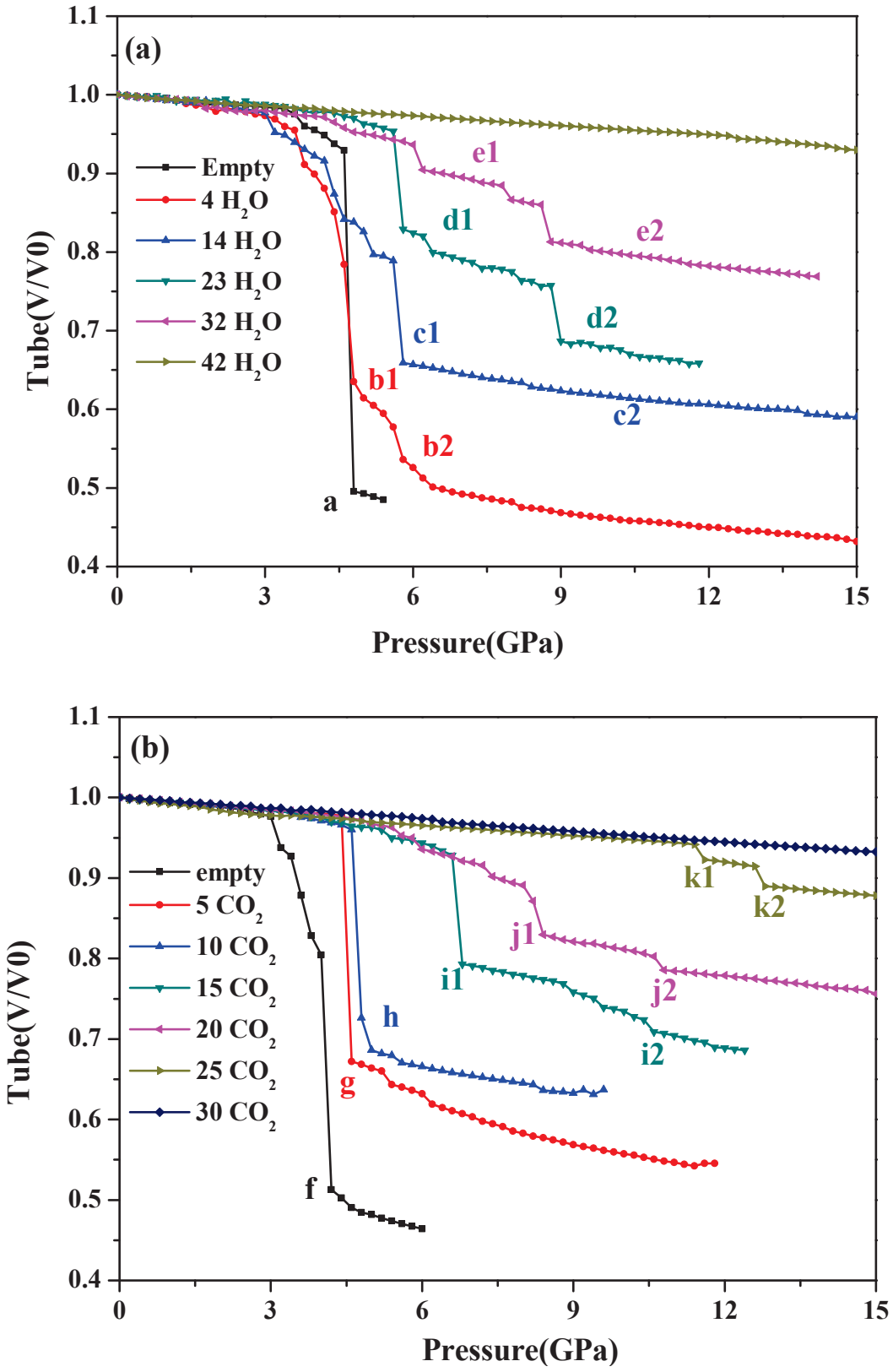

Figure 4.2 Variation of volume as a function of pressure for (10,10) CNTs filled with a different amount of molecules of H_2O (a) and CO_2 (b). The letters label different regimes for which we show snapshots of the nanotube structure in Fig. 4.5, Fig. 4.6, and Fig. 4.7.

Table 4.1 Number of H_2O and CO_2 molecules inside the tubes per unit cell, corresponding H_2O to carbon and CO_2 to carbon mass percentage (%wt), onset pressure (P_o in GPa) and collapse pressure (P_c in GPa) of (10,10) CNTs filled with H_2O and CO_2 in H_2O or CO_2 environments, respectively. We did not observe any collapse up to the maximum pressure of 15 GPa for the cases of 42 H_2O or 30 CO_2 molecules inside the CNTs. For these same filling rations, the P_o incertitude is very high and the values are not included in the table. If not specified, the estimated error for the computed collapse or onset pressure is of ± 0.3 GPa.

nH_2O	%wt	P_o(GPa)	P_c(GPa)	nCO_2	%wt	P_o(GPa)	P_c(GPa)
0	0.0	3.4	4.8	0	0.0	3.0	4.2
4	3.8	1.2	4.8	5	11.5	4.2	4.6
14	13.1	3.0	5.8	10	22.9	3.6	5.0
23	21.6	4.8	5.8	15	34.4	5.2	6.8
32	30.0	4.0 ± 1	6.2	20	45.8	5.4	8.4
42	39.4		> 15	25	57.3	11.4	11.6
				30	68.8		> 15

filled with H_2O, while the lower panel refers to CO_2 filling. The bulk modulus B_0 of the non-collapsed (10,10) nanotube can be estimated from the linear regime variation of V/V_0, yielding a value of $B_0 \simeq 250$ GPa, independently of the filler. In empty tubes, the collapse process to a peanut-like shape is abrupt [65], as it can be clearly seen from the large discontinuity of the corresponding curves. Upon tube filling the collapse process changes considerably. First, the compressibility curves start to deviate progressively from a straight line, marking a difference between the pressure onset of the tube deformation (P_o), and the pressure at which the collapsed shape is found (P_c). The final volume of the collapsed tube increases with filling, simply because the tube can not completely collapse due to the presence of the guest molecules. Finally, the collapse process becomes less abrupt, until it becomes inhibited for large enough filling concentration in the pressure domain of our study.

Due to this complex behavior, it is necessary to define how to measure the deformation onset and the collapse pressure. The onset of the radial deformation can be well established by monitoring the evolution with pressure of the distance of two pairs of carbon atoms belonging to the nanotube, which define perpendicular segments of length approximately equal to the tube diameter as shown in Fig. 4.3. Information and corresponding CNTs structures are displayed in Fig. 4.4. The difference between the length of the two segments becomes larger at P_o. The values of P_o obtained following this criterium to define the ovalization pressure are shown in Table 4.1. Only in the case of 42 H_2O and 30 CO_2, the method did not allow for determining a clear value of P_o , whereas visually a slight deformation of the carbon nanotube cross-section could be observed at high pressure.

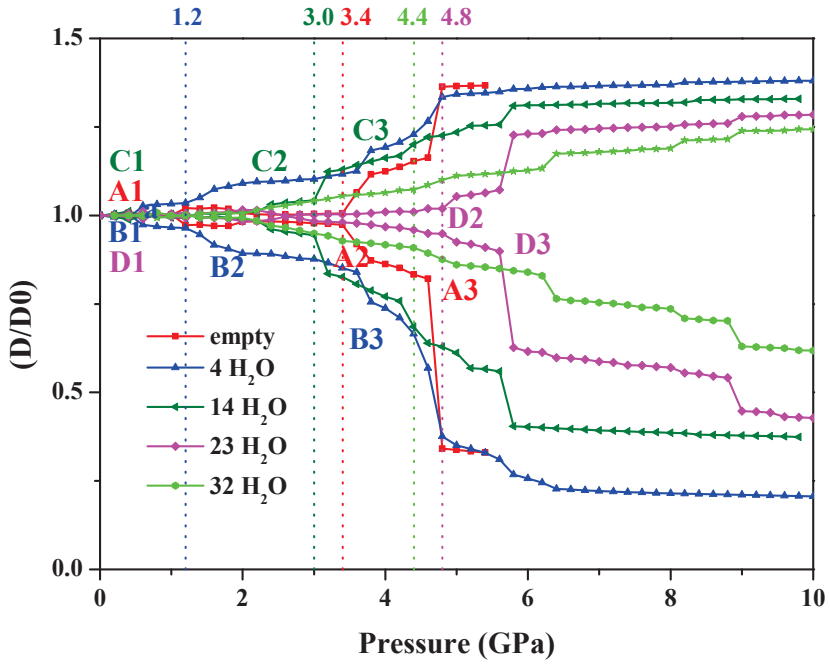

(a)

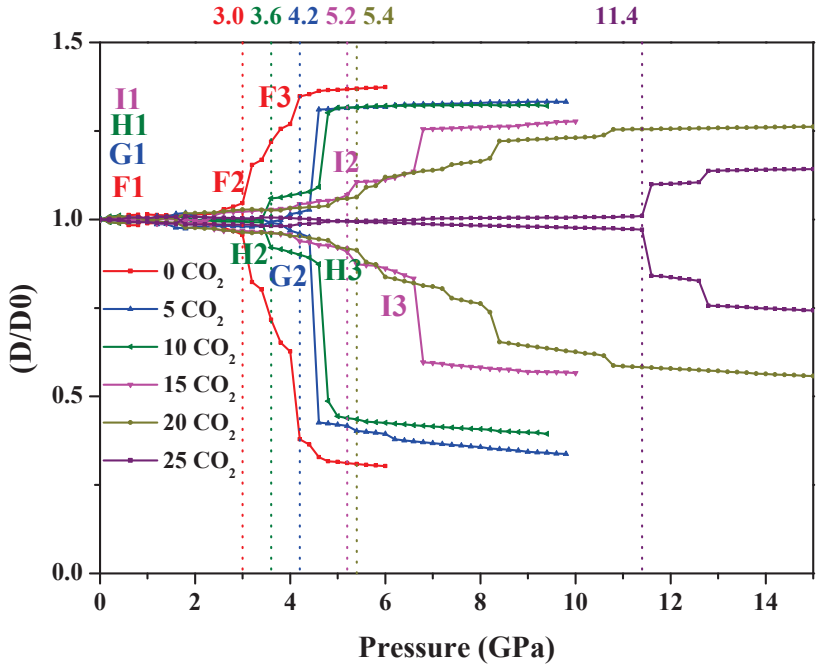

(b)

Figure 4.3 (a) Variation of distance from two pairs of C atoms belonging to the (10,10) CNTs filled with different amount of H_2O and (b) CO_2 molecules as a function of pressure. The segments formed by the pairs of C atoms are approximately perpendicular and their length is approximately equal to the tube diameter. The numbers indicate the onset pressure for the tube deformation *P*o.

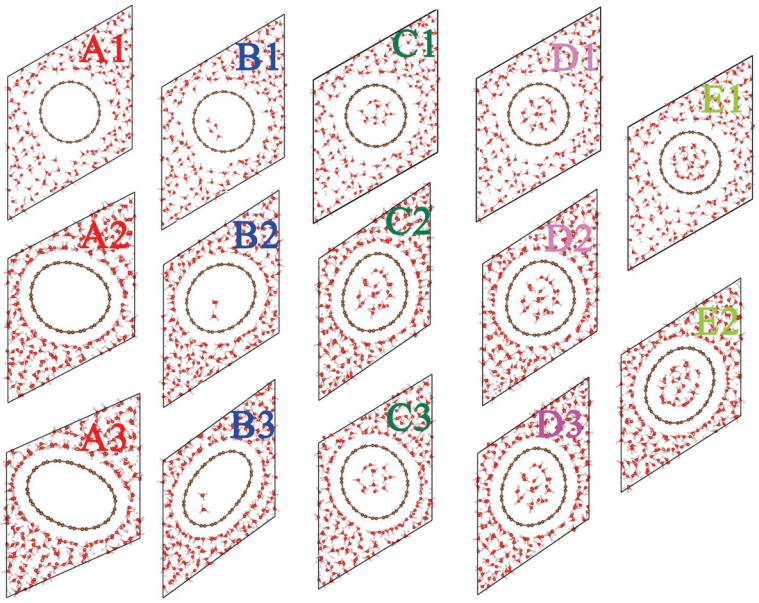

(a)

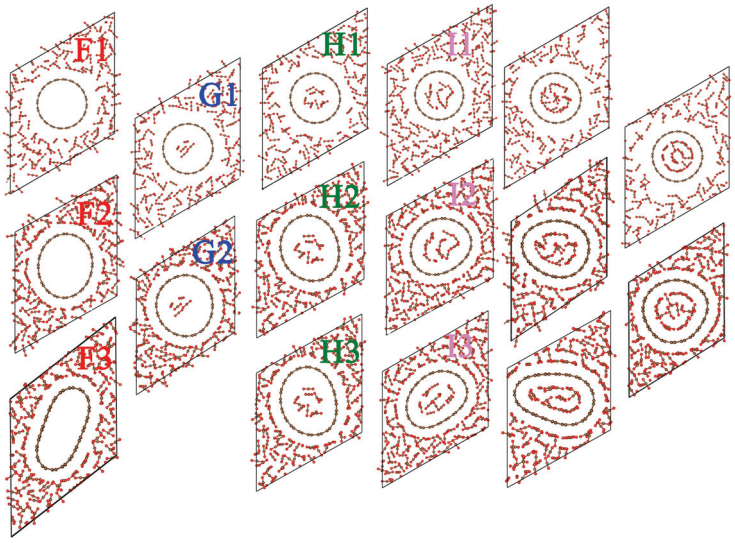

(b)

Figure 4.4 (a) CNTs structures for filling with different amounts of, H_2O and (b) CO_2 molecules, as in Fig. 4.3, before reaching the collapse pressure *P*c.

It is noticeable that whereas a CO_2 filling provides mechanical support [$P_o(n) > P_o(n = 0)$], in the case of H_2O filling, the enclosed molecules favor the deformation of the tube, at least at low and moderate filling [$P_o(n) < P_o(n = 0)$ for $n \leq 23$]. We will discuss again later the implications of this observation in the light of the geometries of the molecular structures that form inside the CNTs.

In order to measure the collapse pressure, one can search for a discontinuity in V/V_0 or in the Gibbs free energy. This method works well for empty tubes or at low-filling. For higher filling ratios, on the other hand, the collapse process is more continuous, and the collapse pressure is difficult to identify precisely. In this case, we decided to define the collapse pressure as the first obvious discontinuity of the volume of the CNT, corresponding to the end of the first "step" of the V/V_0 curve.

In Table 4.1 are also shown the collapse pressures calculated using this procedure as a function of H_2O and CO_2 content. The first result we can read from the table regards the dependence of the collapse pressure with the pressure transmitting medium. Empty (10,10) tubes collapse at around 4.8 GPa (when the transmitting medium is water) and 4.2 GPa (when the transmitting medium is carbon dioxide). These values of pressure are very close to the value calculated for the same (10,10) nanotubes in a bundle geometry (4.5 GPa) [65]. Our result for the (10,10) tube (of diameter 1.36 nm) using water as pressure transmitting medium is also quite close to the 3.9 GPa measured experimentally in Ref. [15] for individualized single-wall (SW) CNTs with an average diameter of 1.32 nm immersed in a water medium containing surfactant molecules. These agreement confirms the validity of our model and approximations.

For tubes filled with 4 and 14 water molecules, we observe two main discontinuities in the volume/pressure curves. A closer inspection of the intermediate structures reveals that the first is mainly related to the transformation of the nanotube cross-section, while the second corresponds to a structural modification of the guest molecules to a more compact geometry. For larger filling the collapse process consists in a series of smaller steps, which correspond to changes of the cross-section of the tube and/or modifications of the structures of the guest molecules as the applied pressure increases. Finally, tubes containing 40 H_2O molecules per unit cell or 30 CO_2 molecules per unit cell do not collapse in the range of explored pressures, i.e. until 15 GPa.

From Fig. 4.2 and Table 4.1 it is clear that the collapse pressure increases with increasing filling, indicating that the guest molecules provide overall mechanical support to the CNT. This is in qualitative agreement with recent experimental findings on water filled tubes [15]: by filling with water a SWCNT with $\langle d \rangle$ = 1.32 nm, and with a measured P_c of 3.9 GPa when empty, the collapse onset moves to 14 $\pm$ 2 GPa and ends at 17 GPa. This is in agreement

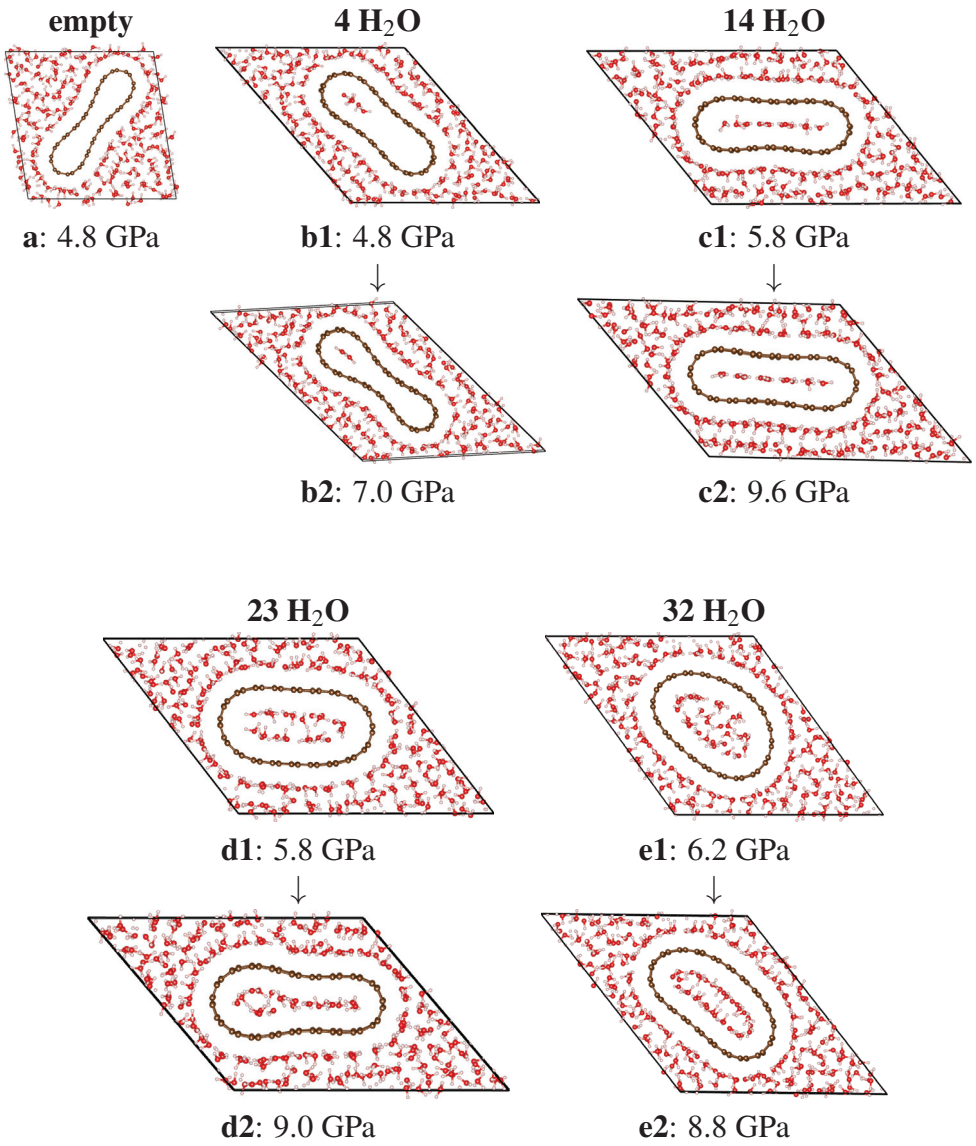

Figure 4.5 Snapshots of cross sections of collapsed CNTs filled with various quantities of H_2O. Under each figure we display a label to specify the corresponding curve and pressure range of Fig. 4.2 (a).

with our findings. In fact, once that the extremities of the tube have been opened, one can not prevent water from entering the tube due to the effect of pressure, until the solidification of the pressure transmitting medium (water with a surfactant), which was observed at around 2 GPa. At this pressure liquid water increases its density by 33%, corresponding in our modeling to a water filling larger than 42%wt. For this filling we did not observe any collapse up to the maximum pressure of 15 GPa.

We show in Fig. 4.5 snapshots of the collapsed water-filled nanotubes, corresponding to the positions marked in the volume/pressure curve of Fig. 4.2. For low water content, we find that the tubes still collapse to the peanut-like shape [see Fig. 4.5 (b1) and (c1)] that they would assume if they were empty [see Fig. 4.5 (a)]. At larger filling [Fig. 4.5 (d1) and (e1)] steric effects prevent the full collapse of the tube, which conserves a highly deformed, ovalized, cross-section. Even more interesting is what happens to the water molecules inside the tube. In Fig. 4.5 (b1) and Fig. 4.6 (b1) we see the formation of a water rhombus, while in Fig. 4.5 (c1) and Fig. 4.6 (c1) we can clearly see the appearance of 2D water nanoribbons, which resemble the "square ice" found in Ref. 31. In these structures the O–O distance is between 2.78 Å to 2.96 Å (significantly smaller than the experimental value of 3.3 Å at ambient pressure), while the O–H distance (O from the acceptor molecules and hydrogen from the donor) lies between 1.81 Å and 1.98 Å (to be compared with 2.4 Å at ambient pressure). [152] The 2D confinement imposes a H–O–H angle of around 107°, inbetween the angle of 104.47° of gaseous water and the tetrahedral angle of 109.47° of hexagonal ice. However, the angle formed by hydrogen bonds is greatly reduced to values between 50° and 90°, depending on the degree of planarity of the hydrogen bonds. At larger water content, as shown in Fig. 4.5 (d) and (e), we find that the guest molecules form water nanotube-like structures, which support the outer carbon tubes, making it more difficult to undergo a significant transformation. This action is similar to the one present in, for example, double-wall CNTs, where the inner tubes provide mechanical support to the outer tube [18, 161].

The second row of Fig. 4.5 depicts the structures of water-containing collapsed CNTs at pressures which correspond to the second discontinuity of the volume/pressure curves of Fig. 4.2 (a). There are some notable differences. In the case of a nanotube containing only 4 water molecules, the rhombus breaks down and a single zigzag chain of water molecules is formed on one of the sides of the tube (see Fig. 4.6). In this case the hydrogen atoms are all in the same plane, and the distance between neighboring molecules becomes 2.71 Å. When the nanotube is filled with 14 water molecules [Fig. 4.5 (c2) and Fig. 4.6 (c2)], there is no large deformation of the water sheet, but now the 2D structure is more planar, with a better alignment of hydrogen atoms in the plane. Increasing even further the water filling,

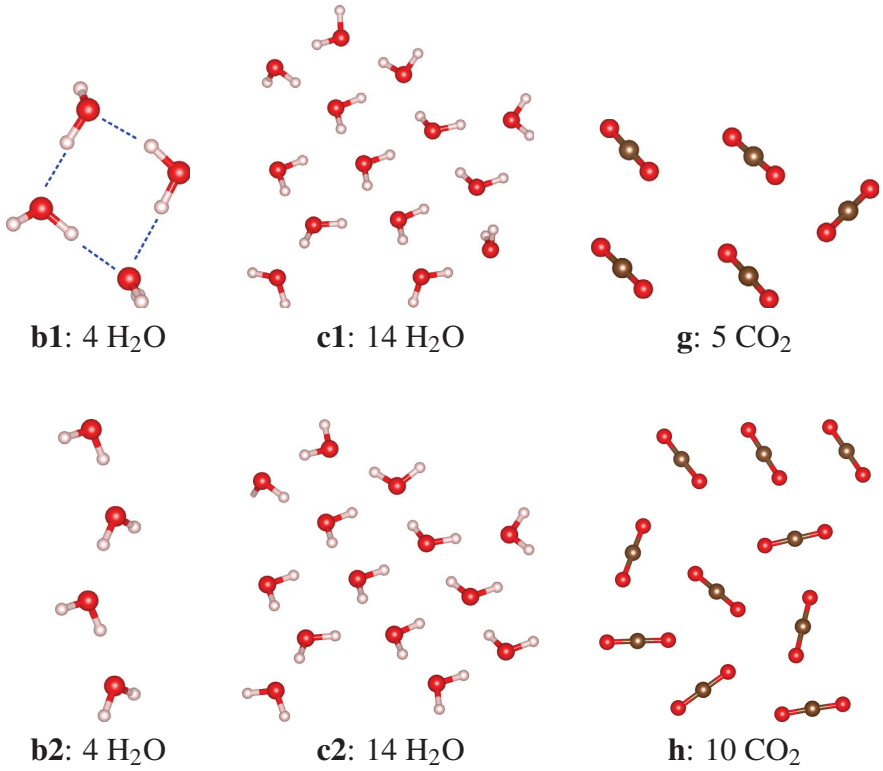

Figure 4.6 Top view of water and CO_2 structures inside collapsed CNTs. The labels refer to those of Fig. 4.5 and Fig.4.7.

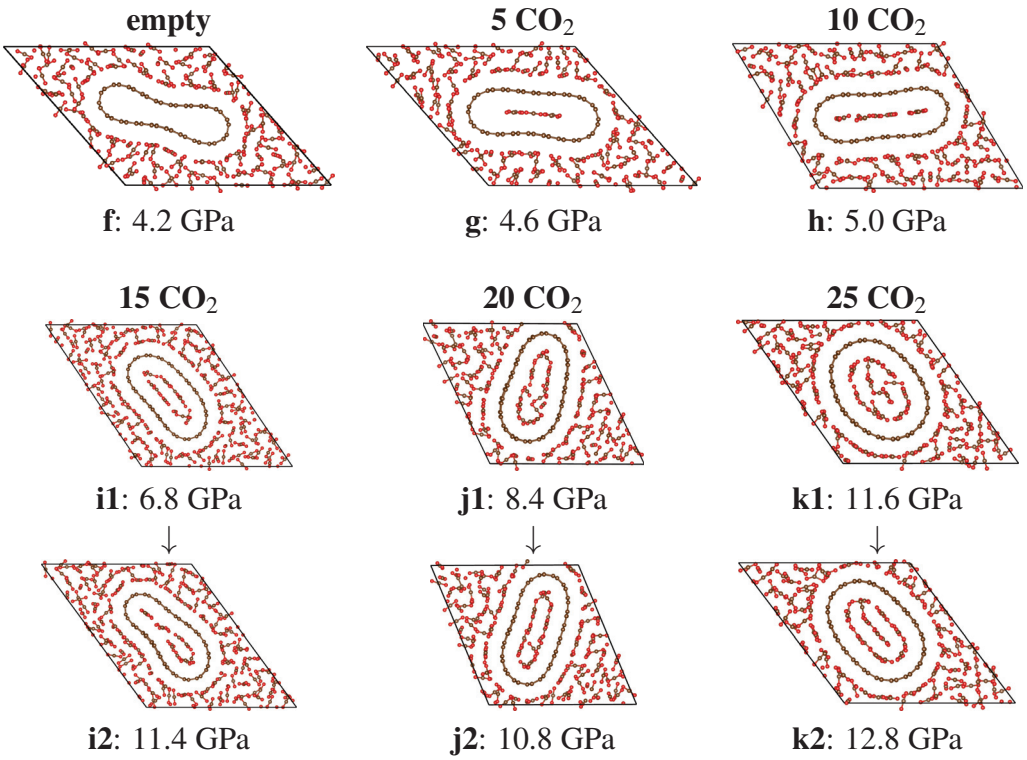

Figure 4.7 Snapshots of cross-section of collapsed CNTs filled with various quantities of CO_2. Under each figure we display a label to specify the corresponding curve and pressure range of Fig. 4.2 (b).

we observe that water inside the CNT of Fig. 4.5 (e2) forms a nearly perfect collapsed water-nanotube. The case in Fig. 4.5 (d2) is a mixed case, as there is not enough water to form a collapsed water nanotube, but there is too much for it to form a 2D water nanoribbon.

A very similar situation arises when we replace water molecules with CO_2. In Fig. 4.7 we show snapshots of collapsed CNTs after the first and the second discontinuities of the volume/pressure curves of Fig. 4.2 (b). Depending on the content of molecules inside the tubes we find planar structures, collapsed nanotubes, and even nanoribbons inside collapsed CO_2 nanotubes inside CNTs. We find that the CO_2 collapsed nanostructures are substantially more planar than those made of water. This fact can be simply explained by the absence of the two lone pairs and the two hydrogen bonds of water, that favor a tetrahedral environment. In spite of this difference, the behavior of water and CO_2 inside tubes is remarkably similar, which makes us believe that the main effect of the nano-confinement is purely geometrical and does not have an electronic nature. This was confirmed by performing electronic structure calculations within DFT. It turns out that the density of electronic states of the combined system can be obtained as a simple superposition between the density of states (DOS) of

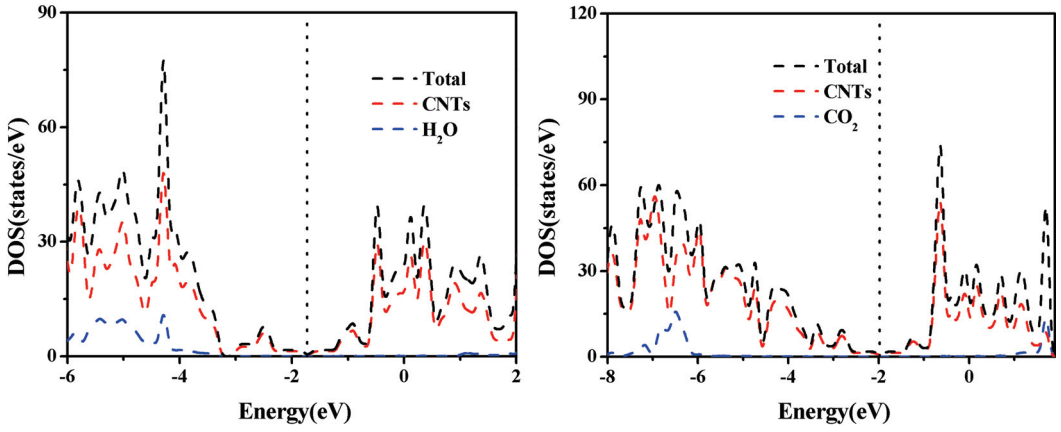

(a) (b)

Figure 4.8 The DOS of some collapsed tubes. (a) and (b) are the DOS of c1 (see Fig. 4.5) and g (see Fig. 4.7) , respectively. The vertical dash lines denote the fermi energy level.

the collapsed tube, the pressure transmitting medium, and the encapsulated molecules (see Fig. 4.8).

In Fig. 4.9 we summarize the results by plotting the collapse pressure and the onset pressure for radial deformation as a function of filling. We observe that the effect of the filling on the collapse pressure follows two different regimes. Indicating with n the number of molecules contained in the tube unit cell and with n_c the critical filling number, for $n < n_c$ P_c increases at a rate of less than 0.1 GPa per n unit whereas for $n > n_c$, P_c increases at least $4-5$ times faster. This critical filling is filler dependent with values of $n_c^{H_2O} \approx 32-42$ and $n_c^{CO_2} \approx 10-15$ in our case. These two different regimes of evolution of $P_c(n)$ can be better understood if we consider the molecular structure inside the CNTs. In the case of CO_2, the critical value n_c corresponds to the number of molecules needed for the nanostructuration of an internal molecular nanotube which provides important mechanical support. The linear structure of the CO_2 molecule allows for a molecular nanotube structuration with a lower number of molecules than what is needed for water, explaining why $n_c^{CO_2} < n_c^{H_2O}$. The case of water is more complicated because the water nanotubes (d1 and e1) do not seem to provide a support as good as the one of CO_2 nanotubes. The different nature of the inter-molecular interactions in H_2O and CO_2 should certainly play an important role in determining the n_c value. In fact, in water the structure of ice is driven by the hydrogen-bond interactions, whereas in CO_2 quadrupole-quadrupole interactions are essential. These interactions lead to pentameric H_2O bulk ice arrangements, on one hand, and to zig-zag arrangements of CO_2 molecules on the other hand.

The dependence on the filling factor of the onset pressure for radial deformation P_o is similar to the dependence of the collapse pressure, and it can be explained by the same

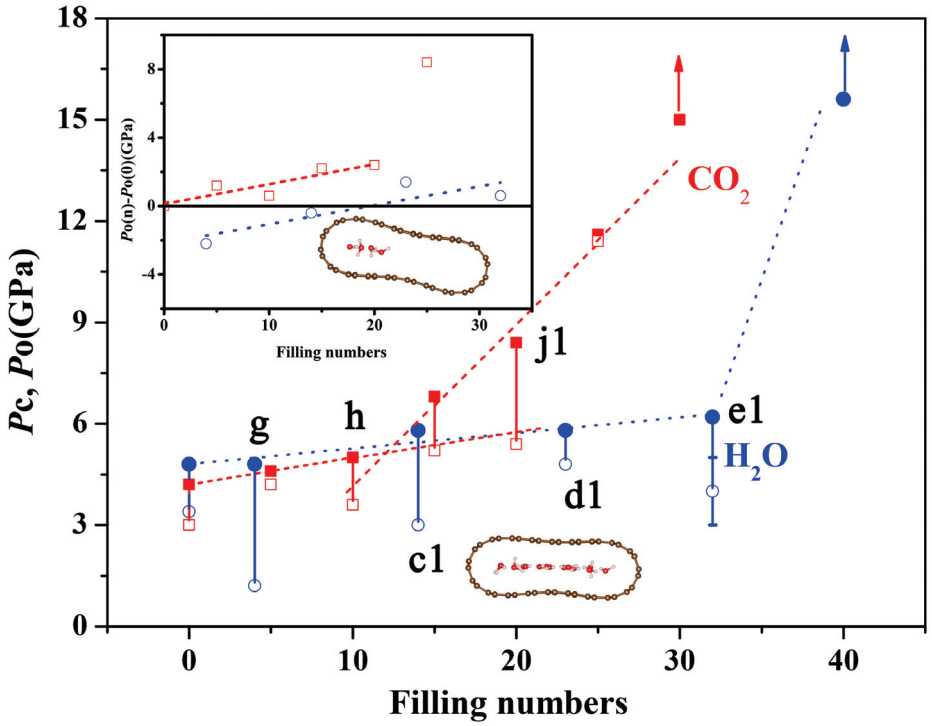

Figure 4.9 Collapse pressure (filled symbols) and pressure for the onset of radial deformation (empty symbols) as a function of molecular filling (water in blue and CO_2 in red). Two regimes can be depicted. The first one corresponds to the low-slope linear evolution of P_c which corresponds to the formation of planar structures. The second regime in which P_c increases more rapidly is associated to the formation of tubular molecular structures that can support the external CNT. The inset shows the evolution of the onset pressure of radial deformation with respect to the empty nanotube. The negative values correspond to non-symmetric filling.

mechanism. In fact, the nanostructures of CO_2 at low filling are more planar and favor a more symmetric filling, yielding therefore a better support to a symmetric collapse. In the case of water, a non planar clustering at low concentration leads to a non-symmetric incomplete filling of the CNT, favoring a radial deformation already at pressures lower than the onset of the empty tube. This is due to the inhomogeneous strain field introduced by the asymmetric filling. We can observe this effect in the inset of Fig. 4.9, where the negative values of $P_o(n) - P_o(0)$ correspond indeed to incomplete (non-symmetric) filling of the CNT.

4.3 Empty carbon nanotubes in water and argon environment

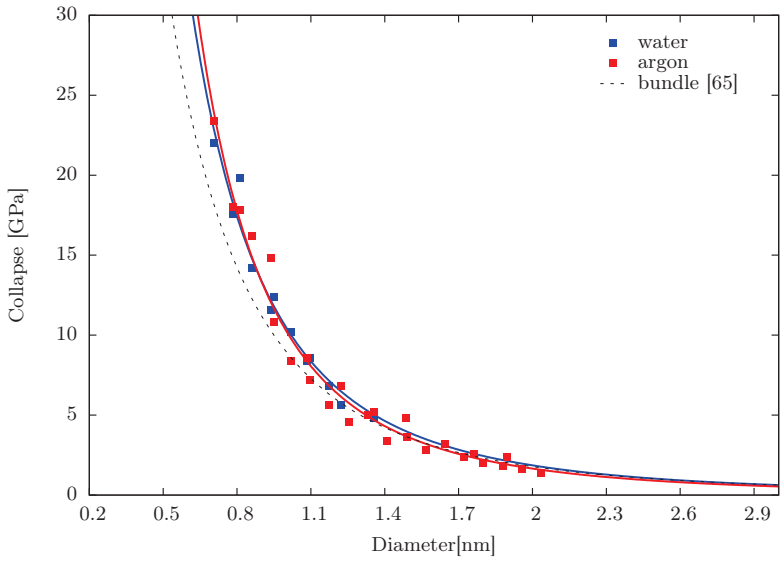

Figure 4.10 Collapse pressure as a function of the nanotube diameter of bundles (Ref. [65]) and individualized CNTs in water and argon environment

In this section, we investigate the effect of PTM (water and argon) on the pressure stability of empty individualized SWCNTs. The parameters used for the DFTB simulation of water are the same used in the section above. We observe that there are no DFTB parameters avaliable for Ar-Ar and Ar-C pairs. However, we can only account for the van der Waals forces with Lennard-Jones potentials as the argon is an inert gas. The parameters were therefore taken from Ref. [9]. To describe the empty CNTs surrounded with molecules, we selected the armchair and zigzag nanotubes with diameters in the range 0.7 –1.4 nm, considering the computational complexity and available experiment here. For the case of argon, we included diameters are up to 3.132 nm due to the fact that calculation of Lennard-Jones potential are computationally efficient. We take 12 and 32 empty tubes in water and argon environment, respectively. As defined above, the calculated collapse values are corresponding to the end of collapse process. The collapse pressure P_c and diameter (d) of CNTs are fitted according to

$$P_c = a/(b+d)^3 \tag{4.2}$$

as is proposed for bundled CNTs [65]. We obtain a = 16.78 GPa nm^3, b = 0.18 nm for water and a = 17.56 GPa nm^3, b = 0.20 nm for argon. As a comparison we also present the fitting values for bundles from Ref. [65], where a = 24.6 GPa nm^3 and b = 0.42 nm.

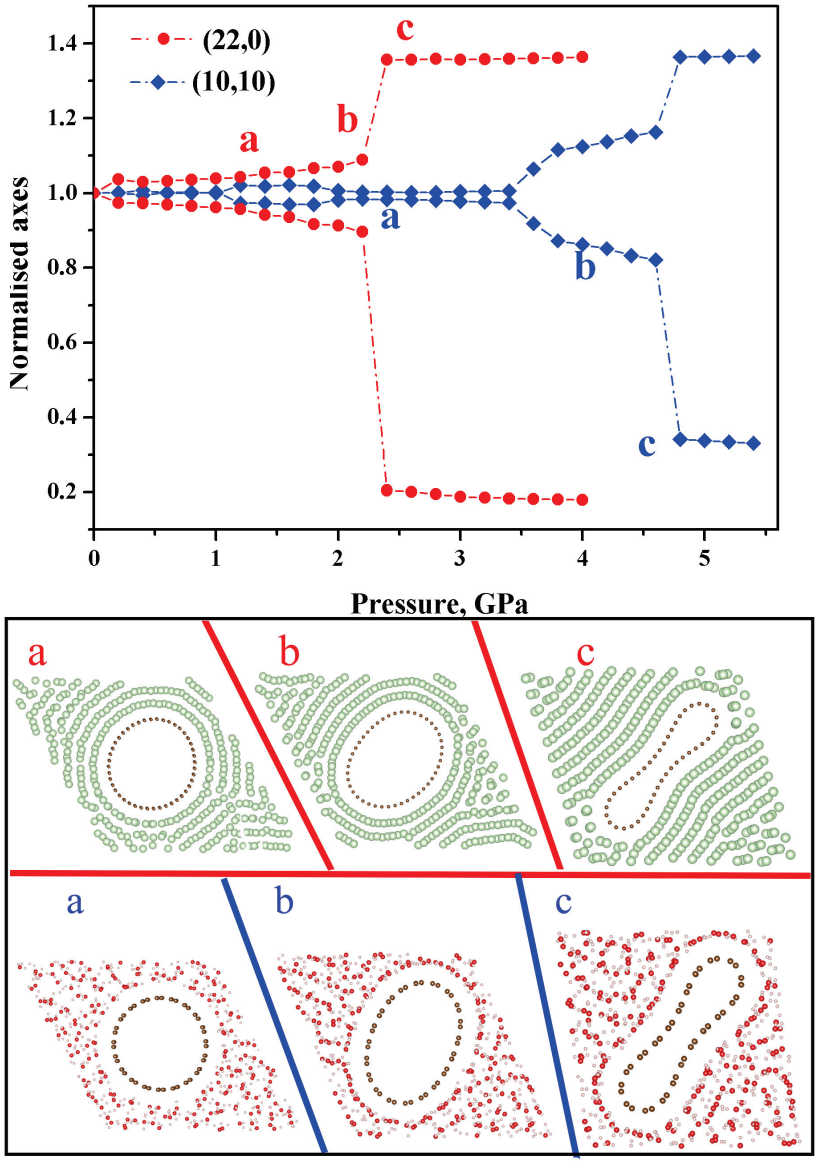

Figure 4.11 (upper panel) Variation of distance from two pairs of C atoms belonging to the (10,10) and (22,0) empty CNTs surrounding by different amount of H_2O and (blue diamond) argon (red circle) molecules as a function of pressure. The segments formed by the pairs of C atoms are approximately perpendicular and their length is approximately equal to the tube diameter. (low panel) The corresponding snapshots.

Table 4.2 Parameters for the bending stiffness, D, determined from the fits of Fig. 4.12. Fits to the data produce α, β and D. Note that 1 GPa nm^3 = 6.242 eV.

	β (nm)	α	D (eV)
DFTB Ar	0.46	1.5	2.34
DFTB H_2O	0.45	1.5	2.33
DFTB bundles [65]	0.41	1.5	1.72
Experiment [15]	0.51	1	1.7

From Fig. 4.10, we find a similar behavior in comparison with bundles. The collapse pressure of individualized CNTs with these three PTMs perfectly follows the d^{-3} law. Effects of the nanotubes chirality on the collpase are not observed. This behavior is again consistent with the previous calculations for bundles [65]. Surprisingly, the collapse pressure of SWCNT depends barely on the PTM, but it is mainly determined by diameters. Experimentally, for the open-ended SWCNTs using different PTM (like paraffin oil, argon , methanol ethanol. etc.), we could not stop the liquid filling into the CNTs. This kind of penetration of liquid PTM will influence the signal of x-ray diffraction [11] and Raman spectra [162], therefore affecting the estimation of collapse. Another note is that the collapse pressure of individual CNTs is slightly higher than the bundles in the small diameter region. Some snapshots of empty CNTs with argon and water are given in Fig. 4.11. We find that most of the DFTB bifurcation cures show discontinuous jumps to the completely collapsed state. It was confirmed again that CNTs undergo phase transition from the circular to a ovalized-shape and then collapse to a peanut shape[73, 163].

On the other hand, theoretical studies had previously proposed a collapse of single-wall CNTs following the Lévy Carrier law $P_C \propto d^{-3}$ [165, 166]. We have proposed a modified version according to the polygon model by introducing the parameter β in the recent work Ref. [164], taking into account for deviations for small diameters ($\sim$ 1 nm), which leads to $P_C d^3 \propto (1-\beta^2/d^2)$. With this modification, we replot the normalized collapse pressure $P_N = P_C d^3$ as a function of collapse pressure shown in Fig. 4.12. The experiment data (including start and end of collapse) [15] and bundled nanotubes without PTM [65] are also fitted as a comparison. All pressures are normalized by d^3 for the continuum mechanics elastic ring prediction $P_C d^3 = 24D$ corresponds to a horizontal straight line, where D is graphene bending modulus. We find empirically that both small and larger tubes follow the Lévy-Carrier formula as $P_C d^3 = 24\alpha D(1-\beta^2/d^2)$, where α is a correction factor with a value of 1 and 1.5 for onset or the end of collapse, respectively. Fitting this expression to all data in Fig. 4.12, we obtained the values of β and D given in Table 4.2.

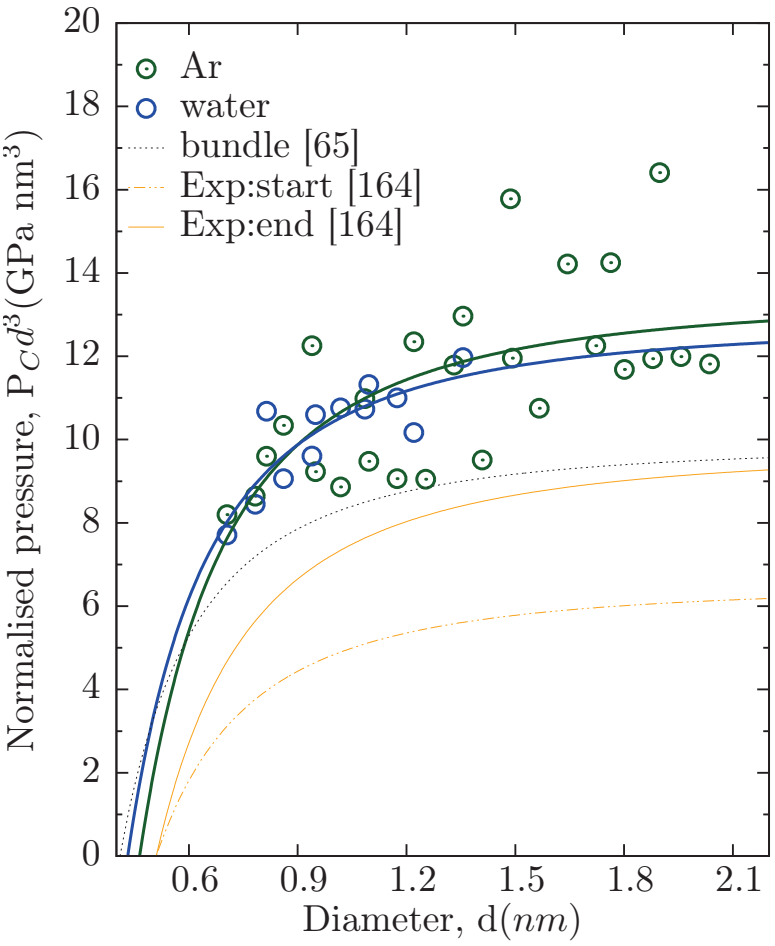

Figure 4.12 The normalized collapse pressure as a function of the diameter. The lines from our DFTB calculations correspond to the end of collapse by fitting to the data using $P_C d^3 = 24\alpha D(1-\beta^2/d^2)$, in which α is 1 for the onset of collapse and 1.5 for the end. The onset and end of collapse from experiment [164] and DFTB bundle [65] are also fit for comparison.

From the Table 4.2, we find a remarkable agreement on β, describing the deviation from the d^{-3} behavior among the theoretical and experimental data. All the values in Table 4.2 are consistent with $\beta = 0.44 \pm 0.03$ nm. That means that in individualized and bundled tubes, β is not greatly affected by the details of the interatomic potentials between the tube and the environment (water, argon, other tubes in DFTB). Within the statistical error bars the effect of β on the collapse pressure begins to be important for diameters below ~ 1 nm, distinguishing the regimes of nano- and meso-scale mechanics. The graphene bending modulus D from the DFTB results on bundles [65] is excellently agreement with experimental [15] data. Larger D values for the DFTB modeling with argon and water are consistent with the solidification and the observed tube-like structure of the first shell of the PTM around the tube, which confers an additional mechanical support [167].

4.4 Conclusions

In summary, we investigated how to use collapsing carbon nanotubes as active nanoavils to engineer exotic molecular structures. By encapsulating water and carbon dioxide, and varying the filling factor and the external hydrostatic pressure, we could easily produce one-dimensional molecular chains, two-dimensional nanoribbons, and even molecular nanotubes that can collapse together with the external carbon nanotube. It is easy to control which structure is formed by varying the density of guest molecules in the nanotube as well the pressure parameter. The procedure described here seems to be quite general, and it can be used to create novel exotic nano objects from a variety of different molecular systems. Moreover, we have shown that depending on the details of the confined molecular nanostructures, they can either favor the deformation of the carbon nanotube cross-section with pressure or, on the contrary, provide support, leading to a strengthening of the nanotube mechanical stability under compressive forces. An important enhancement of the collapse pressure is observed beyond a critical molecular filling ratio characteristic of each molecule. Thanks to the strong dependence of the electronic properties of carbon nanotubes on modifications of their radial cross-section geometry, the molecular filling of carbon nanotubes under pressure appears as an attractive method to tune the electronic structure of nanodevices or composite materials. In the case of nanotubes with large diameters, i.e. with lower radial stability, there is in particular a potential for using the observed phenomena for the development of high sensitivity manometers or gas detectors.

For perfect empty CNTs, collapse under high pressure is barely affected by the PTM environment, but it is mainly determined by the CNTs diameter. However, experimentally, unavoidable liquid penetration and PTM filling the CNTs will significantly influence the

Raman spectra and x-ray diffraction. Depending on the different filling ratio, it will increase the collapse pressure correspondingly. This may explain why some experiments do not observe any phase transitions of CNTs at low pressures.

Adopting the modified Lévy-Carrier law $P_C d^3 \propto (1-\beta^2/d^2)$, β is suggested to depend only on the geometry of the tubes. The bending stiffness of graphene is given as $D = 1.7 \pm 0.2\ eV$ combining theoretical and experimental studies. These studies confirm the underlying Lévy-Carrier d^{-3} dependence of the collapse pressure as in continuum mechanics, with a progressive deviation from d^{-3} at smaller diameters as a consequence, at least in part, of the atomistic nature of the carbon nanotubes.

Chapter 5

Radial collapse in few-wall carbon nanotubes

In this chapter, we will apply the DFTB method to investigate the high-pressure behavior on few (single, double and triple) wall CNTs combining theoretical and experimental studies. The first section presents the basic introduction about the previous experimental and theoretical study of single and double wall carbon nanotubes. The second section describes the methodology, including the theoretical methods and experimental setup, as well as the sample characteriztion. The third section will present the results and our discussion, comparing theoretical simulations and experimental characterization. The last section is the conclusion for this chapter.

5.1 Introduction

A double-wall CNT can be viewed as a single-wall tube filled by another single-wall tube. As such, it is reasonable to expect that the inner tube provides mechanical support, while the outer tube screens the environment [161, 168, 169]. Therefore, double-wall tubes are believed to show higher mechanical stability than single-wall CNTs. Unfortunately, at the beginning of this thesis, it was difficult to extract from the different experimental and theoretical works published up to now a coherent picture on the collapse of CNTs having more than one wall.

Some theoretical results indicate that P_c in double-wall CNTs depends mainly on the diameter of the innter tube d_{in} [84]. In contrast, other studies obtain that P_c is a function of the average of d_{in} and d_{out}, respectively the inner and outer tube diameters [170]. This result implies that not only d_{in}, but also the distance between the walls, are relevant factors

in the collapse process. By averaging over samples having d_{in} varying from 0.5 to 1.9 nm, some experimental studies proposed that geometrical changes happen already at pressures as low as 3 GPa [171], and the response is elastic up to pressure of at least 10 GPa [172]. Other dynamic high-pressure experiments found that only minor tube structure damage occurs below 19 GPa, with the collapse of the double-wall CNT occurring at $\sim$ 26 GPa [85]. However, other works which considered similar diameter distributions reported collapse or large structural modifications at different pressures ranging from $\sim$ 13–15 GPa [173, 174] to $\sim$ 25 GPa [19, 168]. Such important discrepancies can be attributed to the difficulty in working with double-wall CNT samples, mainly due to the large diameter distribution, the effect of the environment on the resonance conditions, and the presence of defects, which depend on synthesis, preparation and handling of the samples.

In this chapter we shed some light on this problem by performing systematic simulations of a large number of few-wall (1, 2, and 3 walls) CNTs, including tubes having different inter-wall separation. These simulations are performed using density-functional tight-binding theory (DFTB) [106], that once again provides an excellent compromise between accuracy and numerical efficiency for carbon-based systems. We compare our results with experimental measurements of the mechanical response and collapse of double-wall CNTs as a function of pressure for samples having inner and outer diameter distributions (as well inter-wall separation) larger than those previously reported.

5.2 Methodology

5.2.1 Calculation details

Density functional tight-binding [106] calculations were performed using the DFTB+ software package [107] with the matsci-0-3 parameter set [175]. This method and the set of parameters are particularly good for carbon compounds, as demonstrated in the previous chapter. Since carbon nanotubes are relatively inert structures where no significant charge transfer is expected [127], we decided to adopt the non-self-consistent charge scheme of DFTB.

Hexagonal unit cells containing two nanotubes with periodic boundary conditions in the three directions were used for a better description of the bundle geometry [65]. To keep calculations feasible, we chose only armchair nanotubes with diameters ranging from 0.6 nm to 3.3 nm: 24 single wall, 22 double wall and 5 triple wall (results for single-wall CNTs with diameter below 1.9 nm were taken from Ref. [65]). Triple-wall nanotubes with inner diameters larger than $\sim$1.2 nm were unfortunately too large to be handled in this work. The

inter-tube distance of the multi-wall CNTs was chosen to be 0.335 nm, except when studying the effect of inter-tube distance, for which larger values were used. Quasi-static simulations were performed as follows: For each value of pressure, a random displacement of 0.002 nm, was applied on each atom in order to break all symmetries. Atomic positions and cell vectors were optimized until the magnitude of all forces became smaller than 10^{-4} Ha/Bohr. The applied pressure was increased in steps of 0.2 GPa up to 30 GPa or until collapse. The collapse of the tubes is abrupt in the large majority of the cases and was identified by a discontinuity in the enthalpy, that corresponds to the transformation to a peanut-like geometry. In some rare cases this discontinuity was not found and the collapse pressure was determined by inspection, i.e., we assigned the collapse to the first peanut-like geometry found. According to this method the obtained collapse pressure corresponds to the end of the collapse process.

5.2.2 Experimental setup and sample characterization

Prof. San-Miguel, Dr. Alencar and Dr. Torres-Dias performed the experiment at Institut Lumière Matière (Lyon).

Samples were prepared by catalytic chemical vapor deposition. A detailed description of the synthesis methodology can be found in Ref. [176]. The histograms in Fig. 5.1(a) and b show the distribution of the number of walls and diameters for the double-wall CNTs studied in this work. A large majority of the tubes (80%) has been observed with an average diameter of 1.5 nm and 2.0 nm for the inner and outer tubes, respectively. Therefore, the signal originated from these tubes is expected to dominate the resonant Raman spectra [176].

High pressure experiments were carried out using a diamond anvil-cell device, with low-fluorescence diamond anvils, having culet sizes of 600 μm. The sample was loaded in a cylindrical pressure chamber with a diameter of 250 μm and thickness of $\sim$90 μm drilled in a pre-indented stainless steel gasket. In-situ Raman measurements were performed using an Acton 300i system, with the excitation energy provided by a 2.41 eV (514.5 nm) laser, having the output power controlled to avoid temperature effects. NaCl was used as pressure transmitting medium to avoid any accidental filling of the tubes [15]. A small ruby chip was loaded with the sample to calibrate the pressure by using the standard ruby luminescence R1 line [177].

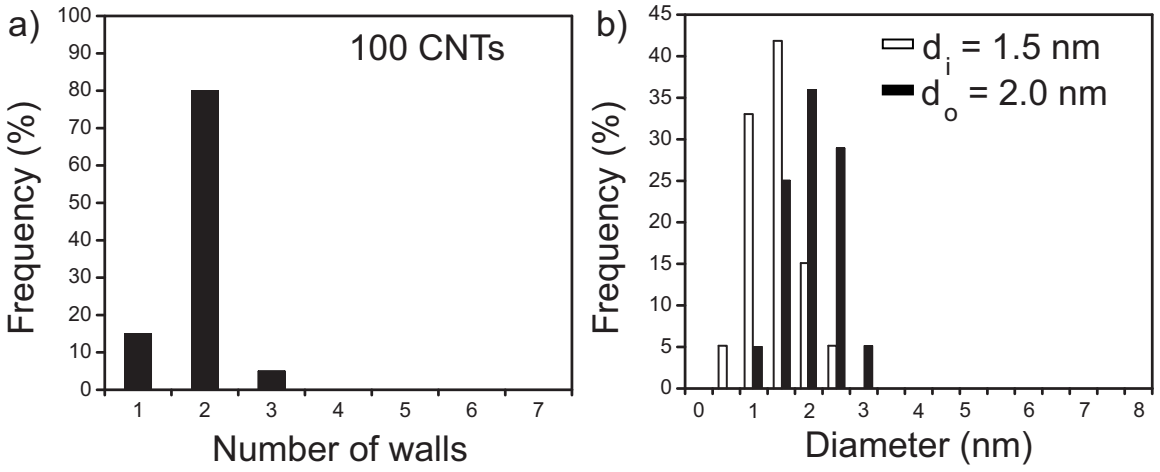

Figure 5.1 Distribution of the (a) number of wall and (b) the inner d_{in} and outer d_{out} diameters in the samples used in Raman experiments. These distributions were obtained from HRTEM image analysis on 100 observed tubes. Numbers given in the label of b) correspond to mean values.

5.3 Results and discussion

5.3.1 Numerical simulations

To clarify the role of the diameter on the collapse in few-walled CNTs we performed DFTB [106] calculations for a selection of armchair (n,n) CNTs. Figure 5.2 shows the calculated normalized collapse pressures, as function of the inner tube diameter, for the single-wall (green triangles), double-wall (blue circles), and triple-wall (red squares) CNTs. This normalized collapse pressure, P_N, corresponds to $P_N = P_c d_{in}^3$ allowing then to better observe deviations from the Lévy-Carrier law which in then represented by a horizontal line. As discussed above, our calculated values correspond to the end of the tube collapse process. Figure 5.2 puts into evidence deviations from the Lévy-Carrier behavior in practically all the domain of explored diameters. We can nevertheless distinguish two clearly different regions. First of all we consider the region for $d_{\text{in}} \lesssim 1.5$ nm. In this region the collapse pressure appears to evolve with independence of the number of tube walls and can be fitted with a same model already proposed for SWCNT[164]:

$$P_{\text{N}} = P_{\text{c}} d_{\text{in}}^3 = \alpha \left(1 - \frac{\beta^2}{d_{\text{in}}^2}\right) \quad \text{GPa nm}^3\,, \tag{5.1}$$

This model corrects from deviations from continuum mechanics by introducing a value of $\beta \neq 0$ which accounts for the discretization of compliances for low tube diameters[164]. The value of β can be also interpreted as the lowest diameter self-sustained stable carbon

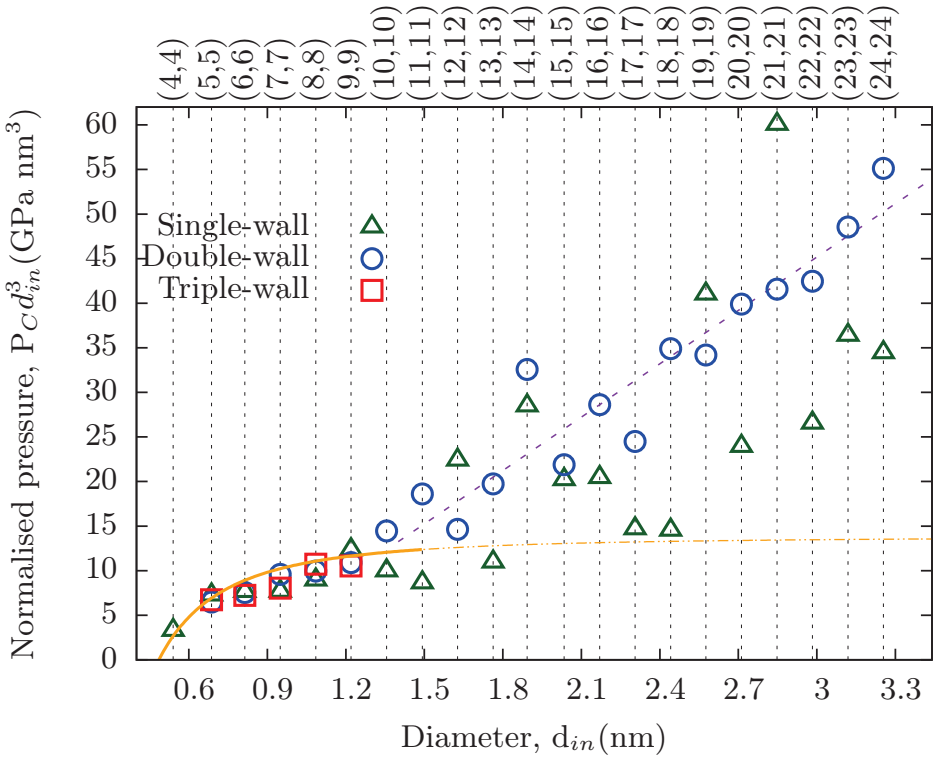

Figure 5.2 Calculated normalized collapse pressure as a function of the diameter (SWCNT) or inner diameter (for double and triple-wall tubes) of bundled few-wall CNTs. All tubes are armchair, i.e.(n,n). The corresponding (n,n) indexes for the innermost tube is given in the upper scale. The continuous line corresponds to the fit using the modified Lévy-Carrier formula in Eq. (5.1) on the calculated data up to $\sim$ 1.5 nm. The dotted line is its extrapolation for larger diameters. The dashed line (in blue) is the linear fit to the deviations from the Lévy-Carrier formula for the double-wall tubes data given by $P_N = a + bd_{in}$ with $a = -15 \pm 5$GPa nm^3 and $b = 20 \pm 2$GPa nm^2.

nanotube which of course has no lower limit in a continuum medium theory. The value of α on its side is related to the bending rigidity, D, of the tube material in the continuum mechanics model and to the one of a graphene foil for SWCNT[164]. We obtain when fitting altogether the data of one- two- and three-walled tubes values of $\alpha = 13.8 \pm 1.2$ GPa nm^3 and $\beta = 0.48 \pm 0.03$ nm. The obtained value of β is in very good agreement with the published result for SWCNT on individualized tubes $\beta = 0.44 \pm 0.04$ nm obtained combining experiments and models[164]. The α value will correspond to associated bending rigidities of the tube-walls of 2.1, 2.5 and 2.1 eV when fitting independently the data for one- two- and three-walled tubes respectively. Those values do not correspond to a logical progression and we prefer then just consider here the average value of α as a fitting parameter.

We may consider now the second region in Fig. 5.2, corresponding to internal tube diameters beyond $\sim$ 1.5 nm. In this regions deviations from the extrapolated curve from Eq. (5.1) become very significant. Even if there is a strong scattering in the calculated values, they increasingly differ to the expected extrapolation of the the values given by Eq. (5.1) (discontinuous line in Fig. 5.2) which in that region correspond well to the Lévy-Carrier expectations. These deviations appear to be linear with pressure in the case of DWCNT but are much more scattered for SWCNT. To explain such deviation, there is a need for a stabilizing energy contribution which is not included in a continuum medium models or even in Eq. (5.1) - which only corrects that model for low diameter tubes. The collapse process involves the modification of the tube curvature leading in the case of an isolated tube to a transition structure having important regions with zero curvature [178]. In the case of carbon nanotube bundles, the hexagonal symmetry can lead to the observation of tube hexagonalized cross-section due to pressure application as it has been proposed from neutron diffraction experiments [78]. The contribution of tube-tube interaction between deformed tubes will increase linearly with their diameter and can be proposed as a possible explanation for the observed deviations from the Lévy-Carrier law for bundled tubes having internal diameters larger than $\sim$ 1.3 nm. In fact, as it is shown in Fig. 5.3 we do observe such polygonization even for internal tube diameters of 1.1 nm in both double-wall or triple-wall tubes.

In Fig. 5.4(a) we show the collapse process as a function of the number of walls for the case of a $(8,8)$ single-wall tube (green curve), a $(8,8)@(13,13)$ double-wall tube (blue curve), and a $(8,8)@(13,13)@(18,18)$ triple-wall tube (red curve). For single-wall CNTs our calculations show a collapse transition usually quite abrupt [65], with a sharp transition to a peanut shape following a (small) compression of the tube. For double- and triple-walls there is a greater reduction of the volume before the collapse (see Fig. 5.4(a)), with the outer (larger) tube starting to deform at lower pressures, but being supported by the innermost (smaller) tube (see Fig. 5.3). The cross-section modification of the outermost tube causes an

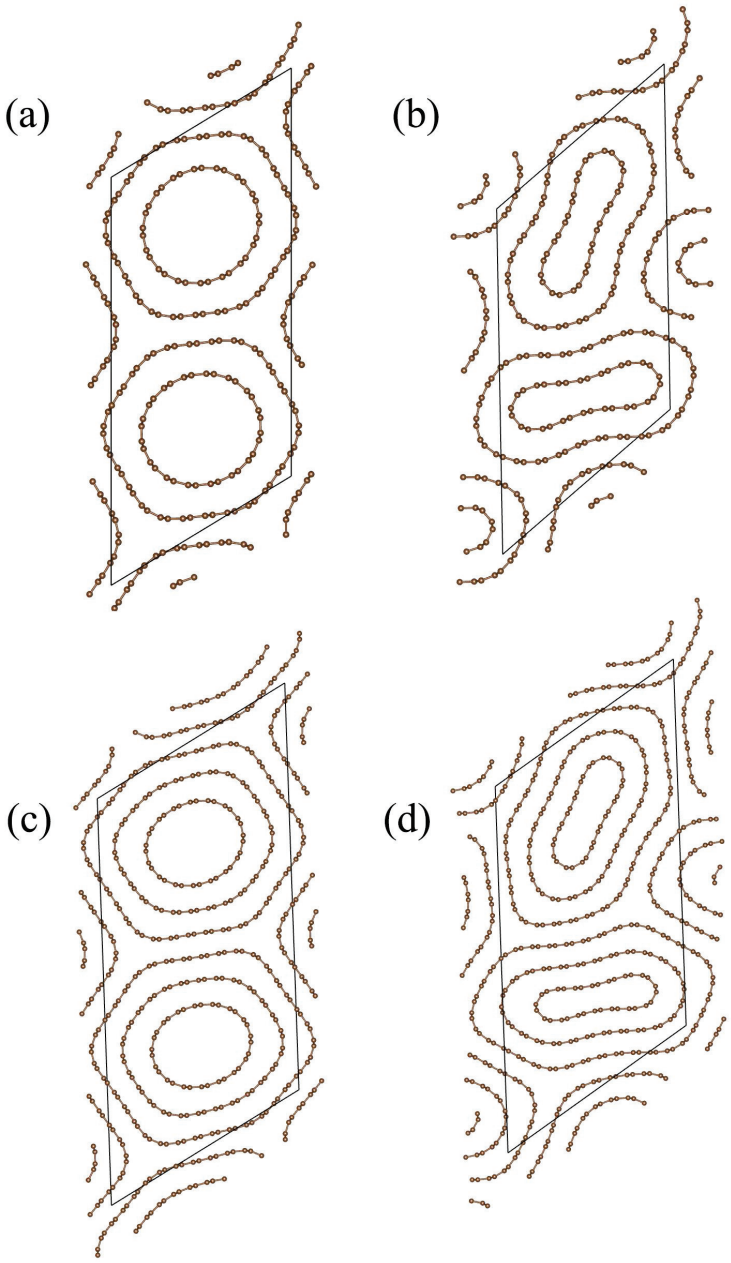

Figure 5.3 Snapshots before and after collapse. (a) and (b) are for (8,8)@(13,13) tubes. (c) and (d) are the (8,8)@(13,13)@(18,18) before and after collapse, respectively. The polygonization of the structure before the collapse can be clearly appreciated.

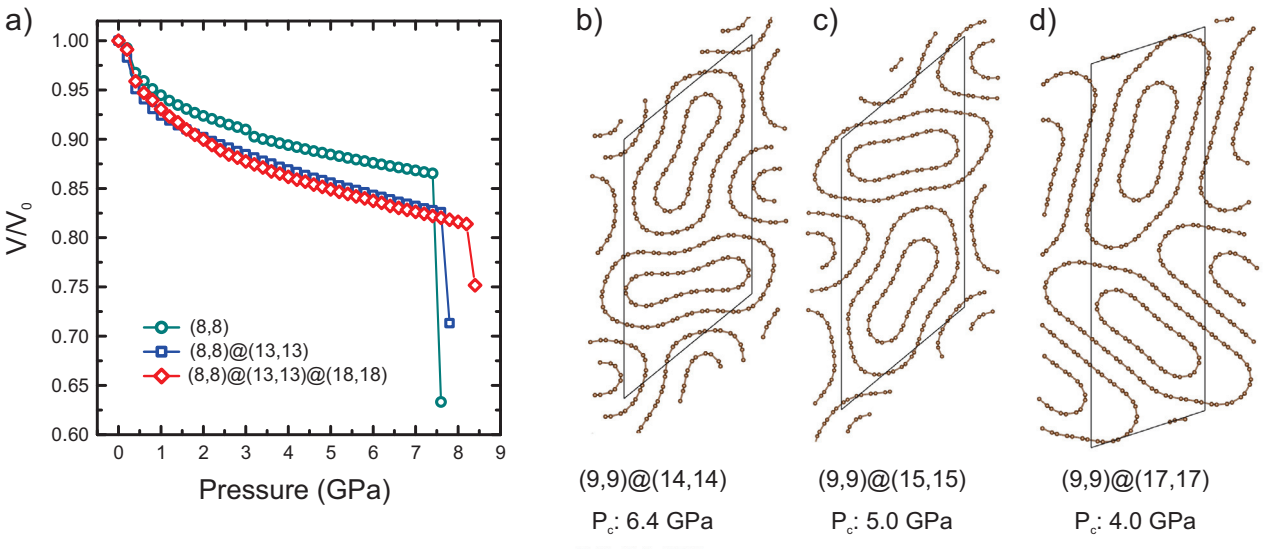

Figure 5.4 (a) Collapse pressure as function of the number of walls. DFTB calculated volume variation up to the onset of the collapse for $(8,8)$ single-wall tube (green curve), a $(8,8)@(13,13)$ double-wall tube (blue curve), and a $(8,8)@(13,13)@(18,18)$ triple-wall tube (red curve). (b)-(d) Collapse pressure as function of the tube-tube interwall distance. Calculated collapsed configurations and respective collapse pressures (labeled at the bottom) of double-wall tubes having a (9,9) inner tube, but three different larger outer tubes.

inhomogeneous strain on the innermost tube, which can then favor the collapse process with respect to the single-wall nanotube case.

Finally, we investigated the collapse of a double-wall CNT as a function of the distance between the inner and the outer tube. We chose as the inner tube a $(9,9)$ CNT with a diameter of 1.22 nm, and for the outer tubes a $(14,14)$, a $(15,15)$, and a $(17,17)$ CNT, leading to a inter-tube spacing of 0.34, 0.41, and 0.54 nm. The calculated collapse pressures for the three cases were 6.4, 5.0, and 4.0 GPa respectively, and the geometry of the collapsed tubes are depicted in Figs. 5.4 (b)-(d). As we can see, there is a considerable decrease of the collapse pressure with increasing inter-wall separation. This observation can again be explained by the larger ovalization of the outer tube, leading to an inhomogeneous compression of the inner tube favoring collapse.

The different elements arising from the discussion of Fig. 5.4 illustrate a more complicate image of the tube collapse process when increasing the number of walls which justifies then that the α parameter in Eq. (5.1) deviates from a simple association to a tube bending rigidity interpretation.

Finally, in Fig. 5.5 we compare experimental collapse pressures for double-wall CNTs with the theoretical curves obtained by fitting our DFTB results. In the graph is represented

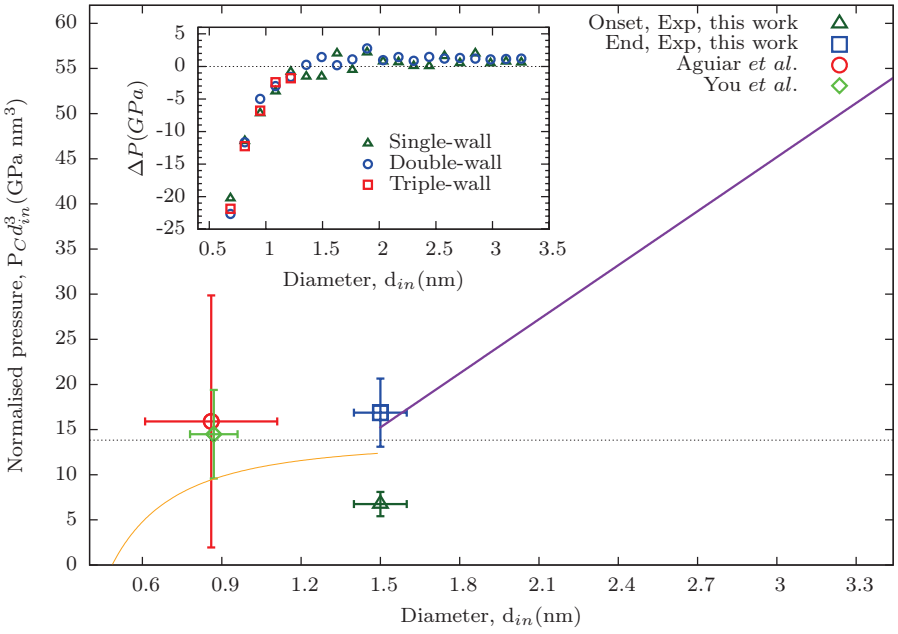

Figure 5.5 DWCNT normalized collapse pressure as a function of the inner diameter. Symbols correspond to our experimental data as well as data from A. Aguiar *et al.* (Ref. [168]) and S. You *et al.* (Ref. [19]). The solid red line is a fit of Eq. (5.1) (α =13.8 GPa nm^3 and β =0.48 nm) and the solid blue line is the linear fit shown in Fig. 5.2 calculated in this work. The dashed black line corresponds to the continuum mechanics prediction by taking $\beta = 0$. The solid lines from our DFTB calculations correspond to the end of collapse. The onset of collapse obtained from our experiments is also shown for comparison. The inset shows the difference in collapse pressure between the the calculated DFTB data and the continuum medium model.

the normalized collapse pressure as function of the inner tube diameter. It is included in continuous line the modified Lévy-Carrier law following Eq. (5.1), as well as the linear variation found from the high diameter deviations shown in Fig. 5.2. The continuous lines represent then our prediction for the collapse pressure dependence on tube diameter. The collapse pressures obtained experimentally in our work and in Refs. [168] and [19] are also included in the graph. The large incertitudes in the experimental points at low diameters arise both from incertitudes in the collapse pressure and on the tube diameter determination. We should remind the reader that the experiment of Ref. [19] was performed on double-wall CNTs solubilised in sodium-cholate water solution (not bundles) which also worked as the pressure-transmitting medium. It is also important to remark that open single-wall CNTs having diameters as small as 0.55 nm become filled with water in surfactant-water solutions [16]. Also, a study on empty and water-filled single-wall CNTs showed that the collapse pressure increases significantly upon water filling [15]. Therefore, the higher values of the collapse pressure in Fig. 5.5 of Ref. [19] could be explained by an unintentional filling of the CNTs. At such high pressures, the non-hydrostaticity of the pressure transmitting medium can also have an effect in the values of the collapse pressures, making more difficult the comparison between experimental and calculated values. In all cases, Fig. 5.5 makes clear that the present precision on the study of the collapse of DWCNT does not allow to discriminate between the predictions of continuum mechanics (horizontal line in Fig. 5.5) and the corrections introduced either by atomic discretization or intertube interactions. The inset in Fig. 5.5 shows the difference in collapse pressure between the continuum mechanics model and our calculations. These differences clearly indicate that very precise measurements are needed to be able to discriminate between models. The study of samples with selected diameters or chiralities - in a similar way as was done in SWCNT[164] - or the study of well characterized individual tubes appears then as the most promising strategy.

In Fig. 5.5 we have also included the pressure corresponding to the onset of the collapse in our Raman experiment (triangle symbol). The recent analytic solution for the collapse of the simple elastic ring under pressure [179, 180] showed a progressive process starting at P_c and finishing at 1.5 P_c. Our experimental results for double-wall carbon nanotubes having inner and outer diameters averaging 1.5 nm and 2.0 nm, respectively show a progressive collapse extending between 2 and 5 GPa which corresponds to an extension up to 2.5 P_c, i.e., significantly more important than the predictions of continuum mechanics. This difference could be attributed to the sequential process of the pressure induced collapse in double-wall CNT[168] related to the non continuum nature of their structure.

5.4 Conclusions

We performed a combined experimental and theoretical study on the collapse of few-wall carbon nanotubes bundles under pressure. Calculations show that the collapse pressure does not follow a simple $1/d_{in}^3$ law, corresponding to the Lévy-Carrier continuous medium prediction. Deviations of distinct origin and opposite directions have been found both in the low diameter regime, due to atomic discretization effects[164] (collapse pressure reduction) and for diameters higher than $\sim$ 1.5 nm, attributed to inter-tube interactions (collapse pressure enhancement) . The collapse process is, however, more complex for the case of few-wall tubes (with respect to their single-wall counterparts), as the outer tube cross-section can be modified at lower pressures, leading then to an inhomogeneous compression of the inner tubes. This can, in turn, reduce the mechanical stability of the few-walled tube. This effect seems to be particularly important when the distance between inner and outer walls increases. Experimentally we have determined the onset and end of collapse of DWCNT having 1.5 nm internal diameter and graphite-like distance between the tubes. Our experimental values of the collapse pressure as well as others find in the literature for smaller tubes do agree with our findings but can also be compatible with a continuum mechanics model. Experiments in samples with well characterized single diameters will be needed to observe the predicted deviations from the predictions of continuum mechanics. All these results appear of particular importance in view of an engineering of composite materials or devices through strain engineering.

Chapter 6

Magnetism and contact properties of the ML MoS_2/Ni(111) interface

6.1 Introduction

Transition-metal dichalcogenides (TMDs) such as MoS_2 (as illustrated in Fig. 6.1) crystallize in layered hexagonal structures, with strong in-plane covalent bonds and weak inter-plane interaction due to Van der Waals forces. Each slab is composed of a single plane of transition metal sandwiched between two chalcogen layers. Similarly to the case of graphene and hexagonal boron nitride (hBN), these materials can be easily exfoliated through micromechanical cleavage [29], or produced by chemical vapor deposition [30], leading to the fabrication of single- and multi-layer structures. If compared with the zero-bandgap graphene and the large indirect bandgap hBN sheet (E_g= 5.995 eV) [181], the monolayer (ML) of MoS_2 appears more interesting for applications in multifunctional electronics and optics thanks to its direct band gap of about 1.9 eV [27], its high quantum efficiency [28] and good electron mobilities [31]. When bulk MoS_2 is thinned down to the monolayer, the appearance of strong photoluminescence [27, 28] marks the transition from the bulk indirect band gap (1.2 eV) to the monolayer direct band gap, with six-fold degenerate band edges in two non-equivalent valleys K^+ and K^-. More generally, ML TMDs like MoS_2, WS_2, $MoSe_2$, WSe_2, $MoTe_2$ are proposed to be used in electronics as transistors, and in optics emitters or detectors. ML MoS_2 transistors have already been demonstrated, with a high mobility 200 cm^2/(V s) and a room-temperature current on /off ratio 1×10^8 [182]. Single-layer MoS_2 phototransistor have also shown unique properties, with an improved photoresponsivity in comparison with graphene-based devices [26]. Moreover, the main advantage of MoS_2 with respect to graphene, is that electron valleys and spin-states can be selectively excited by

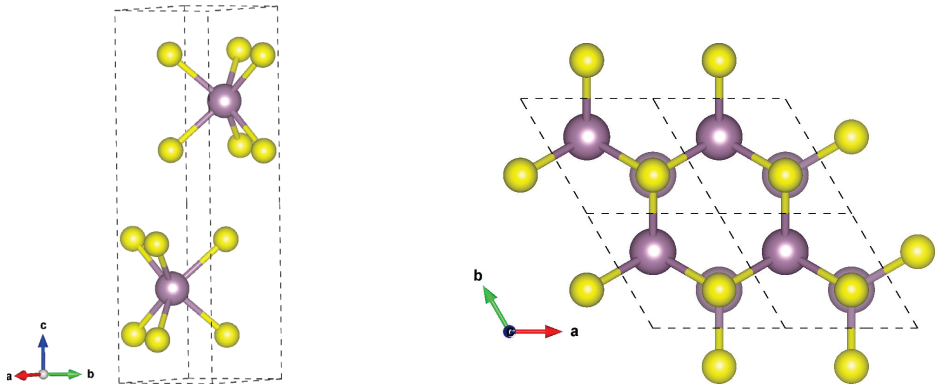

(a) (b)

Figure 6.1 Geometry of MoS_2 (space group $P6_3/mmc$). (a) Side view of a bulk unit cell (dash line). (b) Top view of a monolayer of MoS_2 (2×2 unit cells). The Mo and S atoms are shown with magenta and yellow color, respectively.

a laser of specific circular polarization and energy, thanks to the valley dependent optical selection rules imposed by the crystal symmetry, together with the strong spin-orbit splitting of the top valence band. The K-valley index becomes therefore a new controllable degree of freedom for the charge carriers, opening the way to the new field of valleytronics [183–185], while the spin-orbit splitting allows control of the electron spin, as proposed by spintronics, by tuning the excitation laser photon energy.

In consideration of importance of inducing and manipulating the magnetism in two-dimensional materials for their applications in low-dimensional spintronic devices, the effects of strain and defects have been already considered in literature [186–188]. Doping with transition metals (Mn, Fe, Co, and Zn) [189] can produce two-dimensional diluted magnetic semiconductors, however the predicted Curie temperatures are below room temperature, and the introduction of dopants raises issues of physical and chemical stability. We will therefore explore a different approach to inject spin-polarzied charge in MoS_2, through growth or deposition of the ML TMD on a magnetic substrate.

Another important technological issue that needs to be considered for spintronic applications, is the difficulty to establish low resistance metal contacts with 2D TMDs and metal electrodes, especially when the device architecture requires to build top contacts, i.e. 2D semiconductor metal interfaces. In fact, when 2D materials are interfaced to metals a large Schottky barrier height (SBH) can form at the interface [190–195], hindering the transport of charge and spin carriers. Low-resistance metal contacts are therefore a key challenge to enable the full potential of devices based on 2D TMDs. This explains why several calculations using density functional theory on specific metal-TMD contacts have recently appeared in literature. Transport properties of MoS_2 contacts with Ti and Au were calculated using

DFT without including van der Waals interactions [196]. The physics of contact between Ti, In, Al, Ag and monolayer WSe_2 is discussed in Ref. [197], combining experiments and DFT calculations. The results indicate that the *d*-orbitals of the contact metal play a key role in forming low resistance ohmic contacts with the 2D TMD. Experiments proved also excellent performances for Sc contacts with multilayer MoS_2 [191] and chemically-doped Pd contacts with single-layer WSe_2 [198]. In terms of process robustness and electrical reliability, bulk metals appear still the best option to obtain (quasi) Ohmic contacts with 2D TMDs, compared to the 2D metals proposed by Gan and coworkers [199]. The elementary metals that are usually considered for their excellent physical properties (melting point, electrical conductivity, thermal conductivity) and physical properties (oxidation, stability, toxicity) are Al, Ti, Cr, Ni, Cu, Pd, Ag, In, Pt, and Au. Some of them (In, Pd, Ti, Au) have been thoroughly investigated as contacts for 2D MoS_2 and WS_2 in a recent complete computational study by Kang and coworkers [200].

Going back to the magnetic properties of this family of interfaces, recent studies have shown that a strong interfacial hybridization in $MoS_2/Fe_4N(111)$ [201] and MoS_2/Gd(0001) [202] leads to magnetic moments on the Mo atoms. Using x-ray magnetic circular dichroism, it was also proved that a magnetic moment can be induced in carbon atoms at the graphene/Ni(111) interface due to strong hybridization between C π and Ni 3*d* orbital [203], while DFT calculations [204] predicted magnetic moments on carbon atoms of 0.021 μ_B/atom and 0.027 μ_B/atom for the up and down spin states, respectively. Zhang *et al*. [205] also calculated the induced magnetism of graphene/Ni interfaces, considering different interface configurations with very similar total energies. They obtained similar values for the induced magnetic moments on carbon, with however a significant effect due to the different configurations.

In this context, nickel (Ni), a room-temperature ferromagnetic metals, appears as a particularly promising candidate electrode for high-temperature spintronics devices made of TMDs. In fact, it can combine good electric properties to be used as an electrode with ferromagnetic behavior at high temperatures. Some recent studies have indeed pointed to the use of Ni, among other metals, as a contact for MoS_2 [206, 207]. However, the large lattice mismatch between Ni and MoS_2 (9.1%) [206] has to be taken cautions. Moreover, the magnetic properties of this interface have not been addressed yet.

In this work we investigate thoroughly the electronic and spin properties of ML $MoS_2/Ni(111)$ interfaces using density functional theory including van der Waals interactions. Our results point to the opportunity to investigate further the use Ni contacts for spintronic applications.

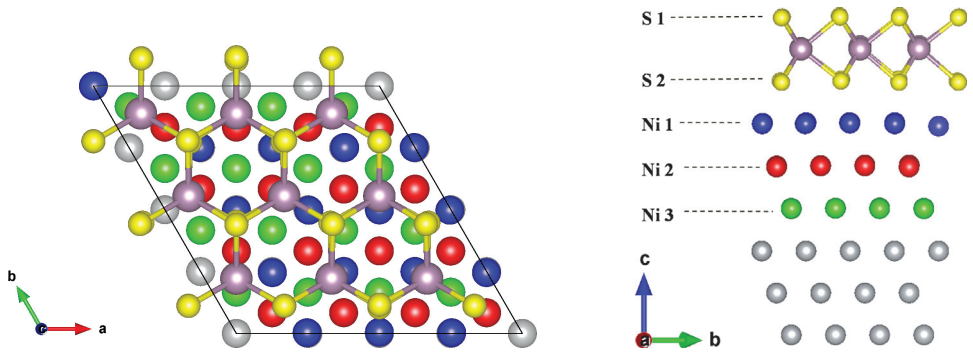

(a) (b)

Figure 6.2 Top (a) and side view (b) of the MoS_2/Ni(111) interface. The three uppermost nickel layers are shown with blue (Ni 1), red (Ni 2) and green balls (Ni 3). Mo atoms are magenta and S atoms (S 1 and S 2) are yellow.

6.2 Computational Details

We performed spin-polarized density functional theory calculations (DFT) using the Vienna *ab initio* simulation package (VASP) [111] within the projector augmented-wave (PAW) method [208, 209]. Bulk MoS_2 has a layered hexagonal structure with space group $P6_3/mmc$ (see Fig. 6.1). The single layer of MoS_2 is composed of a plane of Mo, sandwiched between two planes of S, maintaining the prismatic coordination of the bulk. The symmetry of the monolayer is reduced to $P\bar{6}m2$ due to the loss of the inversion symmetry. Nickel crystallized in a closed-packed face-centered cubic crystal structure. We simulate the contact between the mono-layer of MoS_2 and the (111) Ni surface using a 4×4 Ni surface supercell and a 3×3 MoS_2 supercell with 123 atoms (including 9 Mo atoms, 18 S atoms and 96 Ni atoms). We considered a Ni slab made of six atomic layers. The interface model is depicted in Fig. 6.2. This choice gives the acceptable lattice mismatch of 3.8% at a reasonable supercell size.

A plane-wave basis set with a cutoff of 450 eV and a $4\times4\times1$ Monkhorst-Pack **k**-point grid were used for the geometry optimizations of the interface supercell with a force tolerance of 0.01 eV/Å. The vacuum space along the z direction was taken to be larger than 15 Å and the convergence criterion in the self-consistency process set to 10^{-4} eV. It is well known that traditional DFT exchange-correlation functionals, namely in the local density approximation (LDA) [90] or in the general gradient approximations (GGA) [95], can give reliable structural parameters when covalent and ionic bonding are involved. However these functional fail to describe layers that are weakly bound by van der Waals forces. As van der Waals interaction are expected to play a crucial role in the adhesion of MoS_2 on the metallic surface [207], we applied the optB88-vdW functional [101, 102], designed for dispersion bonded systems. Furthermore, we compared with calculations performed using a GGA exchange-correlation

potential, the Perdew-Burke-Ernzerhof (PBE) functional [207], and with the van der Waals interaction [205, 206]. The optimized lattice parameters of bulk Ni and the free monolayer MoS_2 are 3.52 Å and 3.186 Å using PBE, consistently with previous work [202, 205, 207]. During the optimization, only the top three layers of Ni are free to move, while the three bottom layers are fixed [196, 206]. In the final relaxed geometry (see Fig. 6.2 three S and three Mo atoms composing an hexagon sit on top of six Ni atoms, arranged on the (111) surface in an hexagonal pattern. The distance with PBE and opt88-vdW is 9.83 Å and 9.75 Å, resulting in the MoS_2 a small 3% and 2% lattice strain, respectively which is even better than the initial unrelaxed structure construction.

We calculate the binding energy per S surface atom, between the Ni surface and the monolayer of MoS_2, as $E_b = 1/N_S(E_I - E_{Ni} - E_{MoS_2})$, where N_S is the number of S atoms at the interface, while E_I, E_{Ni}, and E_{MoS_2} represent the total energies of the Ni/MoS_2 interfaces, the Ni(111) slab, and the ML MoS_2, respectively. A negative E_b indicates that the interface is stable.

6.3 Results and Discussion

We discuss now the quality of the Ni/MoS_2 contact, analyzing several criteria.

First of all we consider the metal-adsorbant binding distance and binding energy. A good description of these quantities is essential to obtain an accurate interface potential profile. We will therefore compare thoroughly results obtained with different functionals. As we can see in Table 6.1, PBE and the vdW functional give very similar binding distances, defined as the length separating bottom S atoms from the topmost Ni atoms, while LDA underestimate this length by almost 10%. The calculated interlayer distance in bulk MoS_2 defined by Mo-Mo interlayer separation is 6.11 Å consistent with previous theoretical work [210]. The distance between Ni and MoS_2 defined by the distance of the first top layer Ni atoms and Mo atoms is 3.61 Å , which is much smaller than the MoS_2-MoS_2 distance in the bulk, confirming that there is not only vdW interaction between the layers, but also some covalent bonding.

However, the situation is reversed if we consider binding energies E_b: in this case LDA is closer to the value obtained with the opt88-vdW functional, while PBE accounts only for less than half of the binding energy. These results indicate that it is essential to include van der Waals interactions in these calculations. The binding energy including van der Waals interaction is of -0.38 eV per S atoms, which indicates a relatively strong adhesion of the ML on the Ni surface. We can compare this result with the binding energy of -0.14 eV per atom of graphene on a Ni(111) surface, using the same Van der Waals functional [205]. We

observe that the binding energy is significantly smaller for graphene, consistently with the fact that the graphene monolayer is even less chemically reactive than MoS_2.

We observe that the values of $d_{S\text{-}Ni}$ and E_b are also sensitive to the choice of the supercell, which determines the strain. In fact, we can see in Table 6.1 the comparison with previous calculations that consider different supercells from Refs. [206] and [207]. Note that in the case of Ref. [206], the mismatch is as high as 9.1%. We have to note that, in Ref. [207] the equilibrium distance is chosen from the initially constructed structure in a way to minimalize binding energy. After optimization, the distance is slightly modified. Sulfur atom and nickel atoms thus have an average displacement 0.017 and 0.089 Å, respectively. The comparison with results in literature gives in any case the same qualitative picture, with a clear confirmation of the importance of including van der Waals interaction.

We can conclude that we can expect a significant orbital overlap, and therefore a small or vanishing tunneling barrier. We can be sure that the tunneling barrier will be thin, thanks to the small MoS_2-Ni binding distance. For comparison sake, we remember that the binding distance (see Table. 6.1, d_{S-Ni}, 2.09 Å) that we have calculated is smaller than the one of ML MoS_2 with Au (d_{S-Au} >2.5 Å) [196].

Table 6.1 calculated binding energy (E_b) per surface S atom, the equilibrium distance $d_{S\text{-}Ni}$ in the stable structure of MoS_2/Ni(111) system using different methods.

	LDA	PBE	opt88-vdW	vdW-DF(PW91)
$d_{S\text{-}Ni}$ Å	1.91	2.06 2.2 [207]	2.05 2.2 [207]	2.09 [206]
E_b (eV)	-0.33	-0.18 -0.125 [207]	-0.38 -0.255 [207]	0.83 [206]

We discuss now the calculations of band structures performed with the van der Waals functional. The ML of MoS_2 is a semiconductor, according to our PBE calculations, with a direct band gap of 1.7 eV at K. This value compares well with reported PBE values (1.7 eV) [186], and it is only slightly underestimated with respect to experimental values (1.88 eV from Ref. [27] and 1.85 eV from Ref. [28]. Ni is a metal, with a marked spin asymmetry of the DOS between majority and minority spin channels. We consider now the electronic states at the interface, comparing the density of states (DOS) projected on Mo, S, and Ni orbitals of the MoS_2/Ni(111) supercell with the projected DOS of ML MoS_2 and the projected DOS of the Ni surface in vacuum. The results are shown in Fig. 6.3.

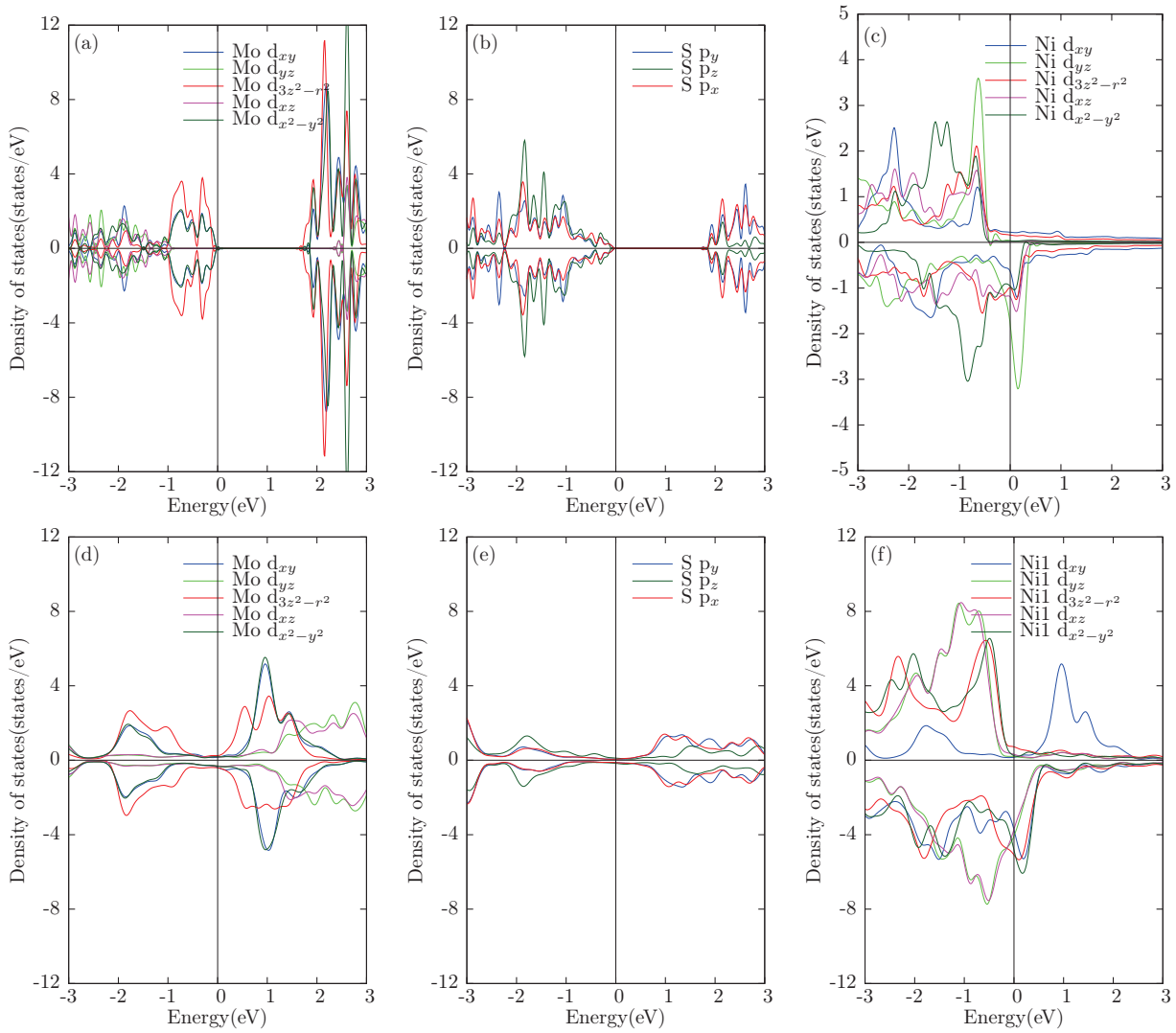

Figure 6.3 Spin-dependent DOS projected on the Mo (a) and S (b) atoms for free-standing ML MoS_2. (c) Spin-dependent DOS projected on the Ni atoms for bulk Ni. DOS of the MoS_2/Ni(111) interface projected on: (d) Mo atoms, (e) S atoms, (f) the topmost layer of Ni atoms. The zero is set at the Fermi energy.

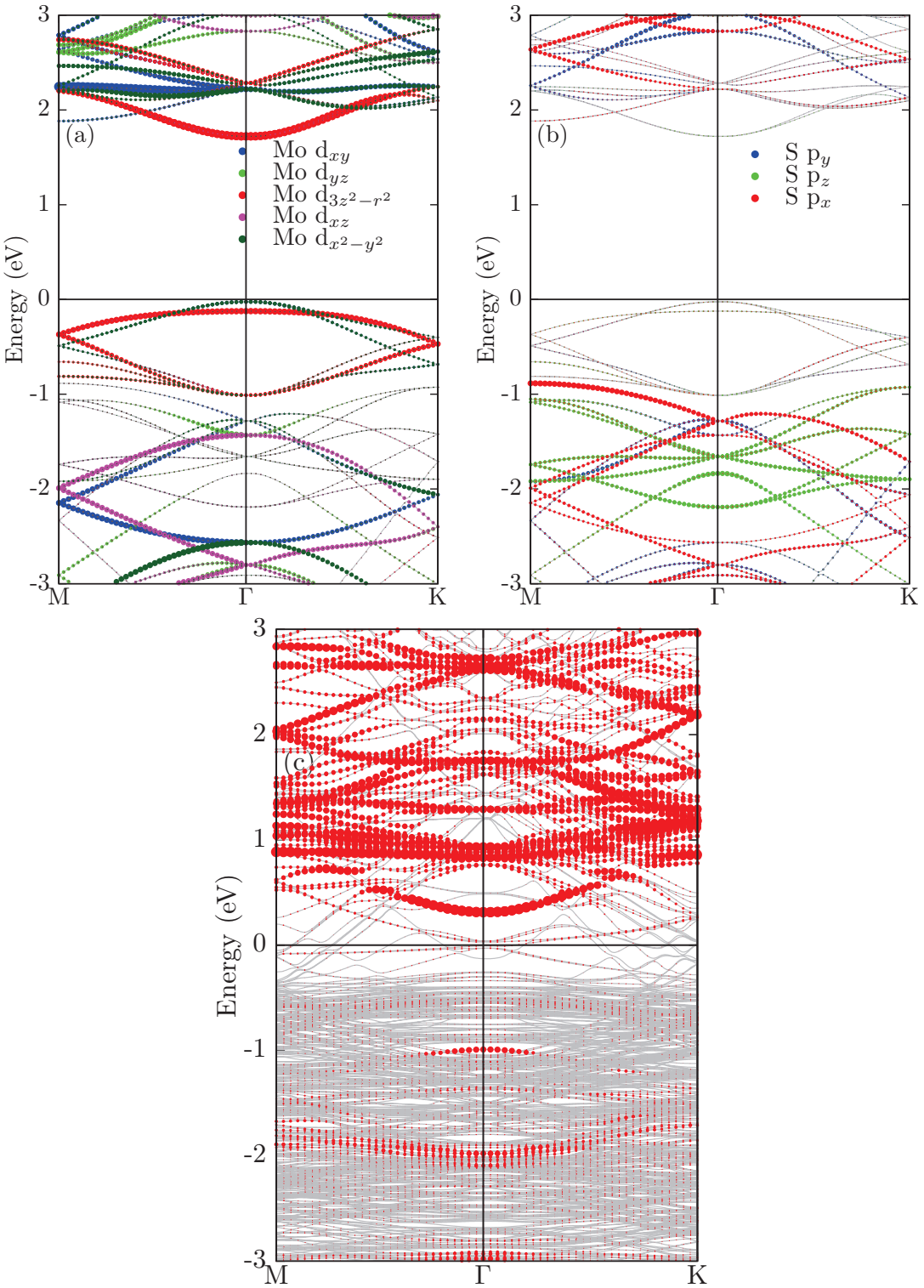

Figure 6.4 Band structure of free-standing ML MoS_2 (3×3) projected on Mo *d*-states (a) and S *p*-states (b), with circle sizes proportional to the projection weights. Band structure of the MoS_2/Ni interface (c). The red circle indicates the states coming mainly from MoS_2. The zero of energy is set at the Fermi level.

The *d* orbitals of Ni change largely when we compare the free surface and the junction. This is true especially for occupied d_{xy} and d_{yz} orbitals at the Fermi level.

In Fig. 6.4, we plot the band structure of the pristine ML MoS_2 in the (3×3) supercell. The panel (a) shows the projection of the bands on Mo *d*-states, while panel (b) show the projection on S *p*-states. Panel (c) displays the band structure of the MoS_2/Ni interface. The bands of MoS_2 are still recognizable, even if there is a strong hybridization with Ni *d*-states. This is very different from the case of the weakly hybridized MoS_2/Au interface [196].

We can observe that the MoS_2/Ni junction is metallic, with a significant amount of Mo, S, and Ni states extending in the band gap of MoS_2. The fact that also Mo and S states appear in the band gap is a clear indication of the hybridization of these states with the ones of Ni. The orbital overlap is particularly relevant between *d* states, as suggested by the projected DOS. We note that a high electron density at the interface is a necessary requirement for a good injection of charge into the MoS_2 layer. In order to explore the possible charge transfer between the interface and isolated Ni and MoS_2 subsystems, we show the charge density difference in Fig. 6.5 (a). We can find a depletion of charge density in Ni 3*d*-states of the topmost layers of nickel atoms and an increase of charge density in *p*-states of the closest S atoms, which implies that the electrons transfer from the substrate to adsorbed ML MoS_2. That also can be concluded by the quantum analysis of Bader charge [211] shown in Table 6.2. The S 1 and S 2 do not gain the same electrons, while the S 2 accepts an extra ~ 0.10 electron charge from the first layer of Ni atoms. This fact is explained by the Ni-S covalent interaction. The excess electrons populate the majority spin channel, resulting in the enhanced Mo 4*d* and S 2*p* magnetic moments shown in Fig. 6.5 (b).

Table 6.2 Average bader Charges for MoS_2/Ni(111) system. Negative (positive) sign indicates an electron loss (gain) for the particular atom. S1 and S2 are atoms far and close to the the first nickel layer (Ni 1), respectively (see Fig. 6.2(b)).

Atoms	Original charge value (e)	$\delta(e)$
Mo	6.0	-1.0416
S 1	6.0	+0.5441
S 2	6.0	+0.6244
Ni 1	10.0	-0.9792
Ni 2	10.0	-0.01224
Ni 3	10.0	-0.00087

We further focus on the magnetic properties of the MoS_2/Ni(111) interface using different functional (see Table 6.3). Due to the underestimation of the magnetism of bulk Ni in LDA calculations (0.557 μ_B) compared with experimental value (0.6 μ_B) [212], we focus on PBE

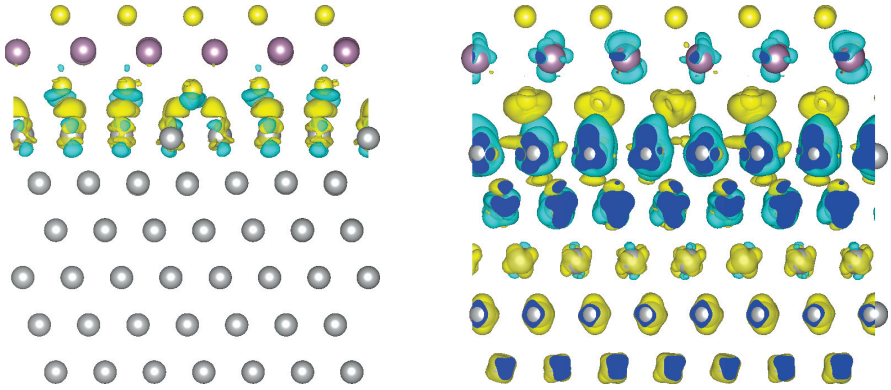

(a) (b)

Figure 6.5 (a) Side view of the charge density difference due to the interaction of Mo_2/Ni(111) interface. The yellow and cyan isosurfaces (2.96×10^{-3} e/Å^3)indicate the electron gain and loss, respectively. (b) Side view spin density difference for the Mo_2/Ni(111) interface with isosurfaces value $5.37\times\ 10^{-3}$ e/Å^3 . Blue color indicated the cross section through the isosurface.

and optB88-vdW results, which are in agreement with experiment for bulk Ni. Mo and S atoms on the surface gain a small magnetic moments, while the substrate nickel atoms reduce their magnetic moments. As shown in Table 6.3 from optB88-vdw (PBE) calculations, Mo and S 2 (close to Ni atoms) atoms carry the magnetic moments ∼-0.019 (-0.022) μ_B and 0.018 (-0.015) μ_B per atom, respectively , where -(+) represents for antiparallel (parallel) orientation of the magnetic moment with respect to the magnetic moments in the Ni-slab. The topmost S (S 1) layers are not influenced due to lack of hybridization with Ni atoms, which further demonstrated that the hybridization induced the magnetic moments on Mo and S atoms. On the other hand, Ni atoms carry average magnetic spin moments per atom of 0.434 (0.5) μ_B and 0.567 (0.625) μ_B for the 1st (Ni 1) and 2nd (Ni 2) Ni layers, compared with the value of 0.632 (0.666) μ_B for the clean Ni surface. It is also noteworthy that the magnetic moments of the Ni clean surface are larger by about 4% using the opt88-vdW functional than the bulk.

We conclude that the magnetic moments are due to the hybridization between Mo 3*d* and Ni 3*d* valence band states. The observed magnetism in the MoS_2 layer induced by a ferromagnetic substrate is of crucial importance for the design of new spintronic devices. Also in C/Ni [205] it was observed strong hybridization of graphene π and Ni 3*d* valence band states with partial charge transfer of the spin-polarized electrons on the graphene π^* unoccupied states.

To conclude, we focus on the quality of the contact. When the interface is created, due to the high work function of Ni (5.04-5.335 eV), electronic charge is transferred from the

Table 6.3 calculated average Magnetic moment ($\mu_B/atom$) of Mo and surface Ni atoms in the stable structure of MoS_2/Ni(111) system using different methods.

Atoms	LDA	PBE	optB88-vdw
Mo	-0.02	-0.022	-0.019
S 1	0.001	0.002	0.001
S 2	0.011	0.015	0.018
Ni 1	0.349	0.500	0.434
Ni 2	0.524	0.625	0.567
clean (Ni 1)	-	0.666	0.632 (0.645 [205])
bulk	0.557	0.603	0.606
bulk		0.6 [212]	

metal to the MoS_2 layer. These electrons populate the interface states, which pin the Fermi level inside the band gap, close to the bottom of the conduction band of MoS_2. In this way, a Schottky barrier Φ_B forms at the interface, i.e. a potential energy barrier for electrons at the metal-semiconductor junction. For many applications an ohmic contact, and therefore $\Phi_B = 0$, is desired, so that the electrical charge can be transported easily between the active region of a transistor and the external circuitry. Several authors have considered how to decrease the Schottky barrier by destroying the interface states, without reducing the overlap of the orbitals, which is essential to remove the tunneling barrier and facilitate charge carrier injection. The proposed solution is to insert a monolayer of graphene or BN [213, 214]. We will not consider here this possibility, because the analysis of previous works can be applied directly *a posteriori* to our case.

We move now to the evaluation of the band alignment, which determines the height of the Schottky barrier Φ_B. This is a key factor to determine a contact resistances in semiconductor MOSFETs, especially for the MoS_2 transistors [215]. The vertical *n*-type (or *p*-type) Schottky barrier for the medium (Ni) can be obtained by measuring the energy difference between E_F and original conducting band minimum (CBM) (or VBM (valence band maximum)) of ML MoS_2 [200]. To calculate the Schottky barrier, we have to align the band structures of ML MoS_2 and MoS_2/Ni(111) interface via the vacuum level E_{vac}. The aligned band structures of MoS_2 and MoS_2/Ni(111) are shown in Fig. 6.6. The Schottky barrier Φ_B is about 0.2 eV. If we directly calculate the difference from Fig. 6.4 (c) between E_F and the identifiable CBM of ML MoS_2, as some previous work did [206, 207, 214], the Schottky barrier is about 0.1 eV larger. Now compare with other examples [196], the small 0.2-0.3 eV Schottky barrier is small and good for spintronic devices design.

Finally, we evaluate the tunnel barrier at the contact, plotting in Fig. 6.7 the effective potential averaged in the plane perpendicular to the interface V_{eff} as a function of the position

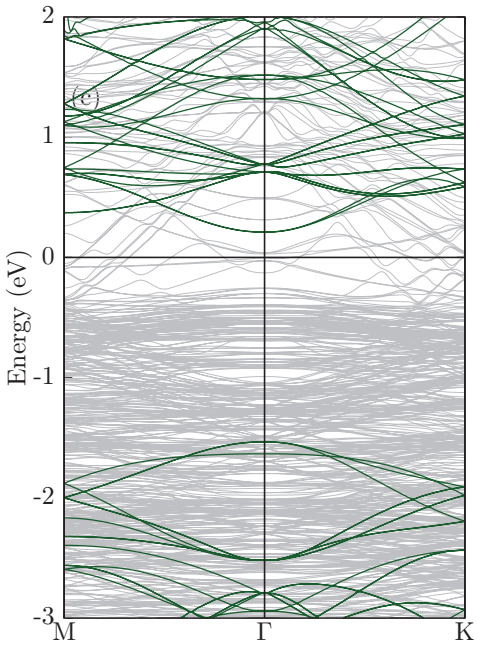

Figure 6.6 The band structure of Mo-MoS_2 system with gray curve. Original band structure of MoS_2 without contact is also plotted for reference(green curves) which is aligned via vacuum level.

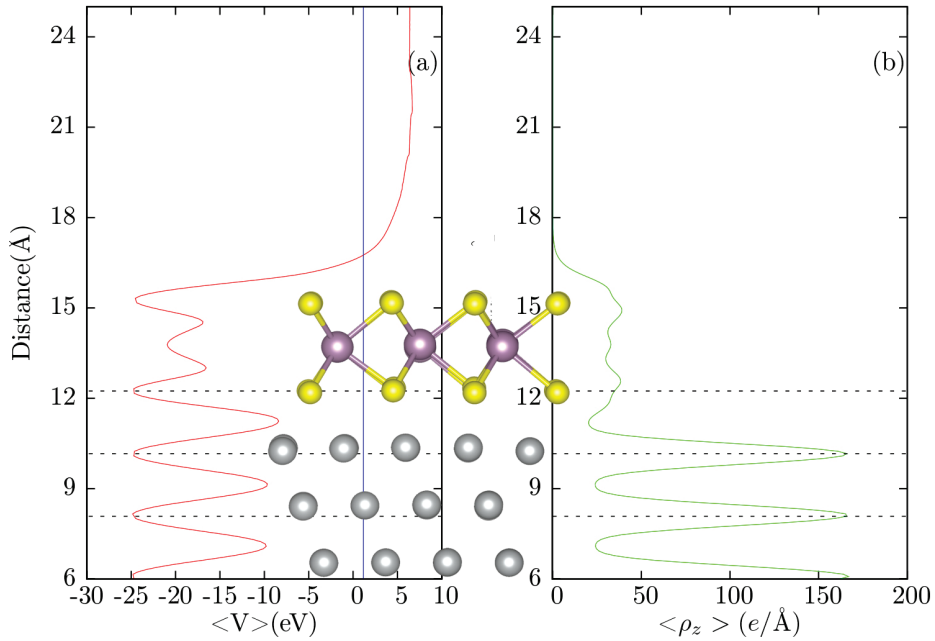

Figure 6.7 (a) and (b) are the average electronic potential and charge along the z direction, respectively. The dot lines indicate the location of Ni and Sulfur layer position at the interface. The blue line indicates the Fermi level

coordinate z in the direction across the interface. The electron density profile is also shown. The higher the electron density at the interface, the higher can be the electron injection. If we define the tunneling barrier as the potential energy above the Fermi energy between the MoS_2 and metal surfaces, we deduce that as expected by the previous analysis, our contact does not present any tunneling barrier.

6.4 Conclusion

In summary, we have investigated systematically the electronic and magnetic properties of ML MoS_2 absorbed on a Ni(111) surface from first principles using density functional theory and accounting for vdW interactions. The van der Waals interaction plays an essential role in stabilizing the interface. The induced magnetism of Mo and S atoms are observed meanwhile reducing magnetic moments of Nickel surface. The small Schottky barrier and tunneling barrier make the MoS_2/Ni(111) interface a low resistance contact, with interesting potential for spintronic applications.

Our study may provide an opportunity for the design of new type of memory-switching or logic devices by using earth-rich nonmagnetic materials MoS_2.

Chapter 7

Summary and conclusions

In this thesis, we investigated the radial collapse under high pressure of carbon nanotubes using the density functional tight-binding method. We considered many different scenarios : individual nanotubes and bundles, single-wall and few-wall nanotubes, different transmitting medium (water, CO_2 and argon) and also the effect of filling of the tubes . We also studied the electronic and magnetic properties of a 2D material: the monolayer of MoS_2/Ni(111) interface using density functional theory, including van der Waals interactions. In the following, we will present the summary of these work.

Filling and PTM effect on carbon nanotubes collapse We investigated the effect of filling and pressure transmitting medium on collapse of carbon nanotubes with density functional tight-binding method. For filled CTNs, we find the collapsing/collapsed nanotubes can serve as active nanoanvils. By tuning the density of filling factor and external hydrostatic pressure, one dimensional molecular chains, two-dimensional nanoribbons, and even nanotube-like molecules. Moreover, depending on the details of confined molecular nanostructures, they can either favor the deformation of the carbon nanotubes cross-section with pressure or, on the contrary, provide mechanical support. For the empty tubes, the collapse behavior is barely affected by the pressure transmitting medium environment but mainly by the tubes diameter, which further confirmed the underlying Lévy-Carrier $d^{-}3$ dependence of the collapse pressure with a progressive deviation for smaller diameters ($\sim$ 1 nm).

Radial collapse in few-wall carbon nanotubes In a combined experimental and theoretical study, we investigated the collapse of few-wall carbon nanotubes bundles under pressure. Calculations show that the collapse pressure does not follow a simple $1/d_{in}^3$ law, corresponding to the Lévy-Carrier continuous medium prediction. Deviations of distinct

origin and opposite directions have been found both in the low diameter regime, due to atomic discretization effects [164] (collapse pressure reduction) and for diameters higher than $\sim$ 1.5 nm, attributed to inter-tube interactions (collapse pressure enhancement) . The collapse process is, however, more complex for the case of few-wall tubes (with respect to their single-wall counterparts), as the outer tube cross-section can be modified at lower pressures, leading then to an inhomogeneous compression of the inner tubes. This can, in turn, reduce the mechanical stability of the few-walled tube. This effect seems to be particularly important when the distance between inner and outer walls increases. Experimentally we have determined the onset and end of collapse of double wall carbon nanotubes having 1.5 nm internal diameter and graphite-like distance between the tubes. Our experimental values of the collapse pressure as well as others studies in the literature for smaller tubes do agree with our findings but can also be compatible with a continuum mechanics model. Experiments in samples with well characterized single diameters will be needed to observe the predicted deviations from the predictions of continuum mechanics. All these results appear of particular importance in view of an engineering of composite materials or devices through strain engineering.

Magetism and contact properties of the ML MoS_2/Ni(111) interface We investigated systematically the electronic and magnetic properties of monolayer MoS_2 absorbed on a Ni(111) surface from first principles, using density functional theory and accounting for vdW interactions. The van der Waals interaction plays an essential role in stabilizing the interface. The induced magnetism of Mo and S atoms are observed, with a concomitant reduction of the magnetic moments on the Ni surface. The small Schottky barrier and tunneling barrier make the MoS_2/Ni(111) interface the low resistance contact. Our study may provide an opportunity for the design of new type of memory-switching or logic devices by using earth-rich nonmagnetic materials MoS_2 .

Acknowledgements

Firstly, I would like to express my sincere gratitude to my dedicated supervisors, Prof. Alfonso San Miguel, Prof. Miguel Marques and Prof. Silvana Botti, for providing me the opportunity to work on this thesis project, for their patient guidance and fruitful discussions, and for the careful corrections on my manuscript.

I am very grateful for the help from Dr. Tiago Cerqueira, who gave me a lot of advice and explanations for the theoretical calculations about this research work.

I acknowledge Dr. Rafael Alencar and Dr. Abraao Torres Dias for their collaboration on performing the experiment work. I would like to thank Prof. David Dunstan for the helpful suggestions and discussions.

My thanks are also devoted to Dr. Sabine Korbel, Pedro Borlido, Sun Lin, Dr. Claudia Rödl, Ivan Guilhon Mitoso Rocha, Valerio Armuzza, Christoph Otzen, Thomas Bischoff, Dr. Aude Stolz, Silio Domingos Siva Santos and Ophelliam Loiselet for their accompany and friendship. I also appreciate the help from the technical staff Ms. Marion Fiedler and Sylvia Hennig.

I would also like to thank Biwen Zhu, Zonglong Yang and Dan Yi for their treatments before I find my own appartment.

I would like to thank Prof. Yanming Ma who advised me to apply for the Scholarship provided by China Scholarship Coucil and helped me to contact Prof. Alfonso San Miguel. I also express my acknowledgements to Institut Lumière Matière, Université Claude Bernard Lyon 1 (UCBL) and China Scholarship Council. They offered me this great opportunity to study and work in France.

Finally particular thanks to my boyfriend Jinming Shi who helps me a lot either on daily life and work. I would also like to thank my parents who always stand with me and support me spiritually for these years.

List of Publications

• W. Cui, T. F. T. Cerqueira, S. Botti, M. A. L. Marques, and A. San- Miguel. Nanostructured water and carbon dioxide inside collapsing carbon nanotubes at high pressure, Phys. Chem. Chem. Phys. 2016, 18, 19926–19932

• W. Cui, J. Shi, S. Botti, and M. A. L. Marques. Magnetism and contact properties of the ML MoS_2 interface, 2017 (ready to submit)

• J. Shi, W. Cui, J. Flores-Livas, S. Botti, and M. A. L. Marques. New phases in the Ba-Si phase diagram under high pressure by ab initio structural search, Phys. Chem. Chem. Phys. 2016, 18, 8108-8114

• J. Shi, T. F. T. Cerqueira, W. Cui, S. Botti, and M. A. L. Marques. High-throughput search of ternary chalcogenides for p-type transparent electrodes, Sci. Rep. 2017, 7, 43179

• J. Shi, W. Cui, S. Botti, and M. A. L. Marques. Ternary phase diagram of the N–H–O system: new phases at high pressure, 2017 (submited to J. Phys. Chem. Lett.)

• A. C. Torres-Dias, T. F. T. Cerqueira, W. Cui, S. Cambie, M. Marques, S. Botti, W. Wenseleers, D. Machon, M. A. Hartmann, Y. W. Sun, D. J. Dunstan, and A. San-Miguel. From mesoscale to nanoscale mechanics in single-wall carbon nanotubes, Carbon, 2017, 123, 145-150

• R. S. Alencar, W. Cui, A. C. Torres-Dias, T. F. T. Cerqueira, S. Botti, and M. A. L. Marques, O. P. Ferreira, Ch. Laurent, A. Weibel, D. Machon, D.J. Dunstan, A. G. Souza Filho, A. G. Souza Filho, A. San-Miguel. Pressure-induced radial collapse in few-wall carbon nanotubes: A combined theoretical and experimental study, 2017 (submitted to Carbon)

Bibliography

[1] Kroto, H.; Heath, J.; O'Brien, S.; Curl, R.; Smalley, R. C_{60} Buckminsterfuler. *Nature* **1985**, *162*, 318–320.

[2] Iijima, S. Helical microtubules of graphitic carbon. *Nature* **1991**, *354*, 56–58.

[3] Novoselov, K. S.; Geim, A. K.; Morozov, S. V.; Jiang, D.; Zhang, Y.; Dubonos, S. V.; Grigorieva, I. V.; Firsov, A. A. Electric field effect in atomically thin carbon films. *Science* **2004**, *306*, 666–669.

[4] Lu, J. P. Elastic properties of carbon nanotubes and nanoropes. *Phys. Rev. Lett.* **1997**, *79*, 1297.

[5] De Volder, M. F. L.; Tawfick, S. H.; Baughman, R. H.; Hart, A. J. Carbon Nanotubes: Present and Future Commercial Applications. *Science* **2013**, *339*, 535–539.

[6] Holt, J. K.; Park, H. G.; Wang, Y.; Stadermann, M.; Artyukhin, A. B.; Grigoropoulos, C. P.; Noy, A.; Bakajin, O. Fast mass transport through sub-2-nanometer carbon nanotubes. *Science* **2006**, *312*, 1034–1037.

[7] Sparreboom, W. v.; Van Den Berg, A.; Eijkel, J. Principles and applications of nanofluidic transport. *Nat. Nanotechnol.* **2009**, *4*, 713–720.

[8] Zambrano, H. A.; Walther, J. H.; Koumoutsakos, P.; Sbalzarini, I. Thermophoretic motion of water nanodroplets confined inside carbon nanotubes. *Nano Lett.* **2009**, *9*, 66–71.

[9] Shanavas, K.; Sharma, S. M. Molecular dynamics simulations of phase transitions in argon-filled single-walled carbon nanotube bundles under high pressure. *Phys. Rev. B* **2009**, *79*, 155425.

[10] Alvarez, L.; Bantignies, J.-L.; Le Parc, R.; Aznar, R.; Sauvajol, J.-L.; Merlen, A.; Machon, D.; San Miguel, A. High-pressure behavior of polyiodides confined into single-walled carbon nanotubes: A Raman study. *Phys. Rev. B* **2010**, *82*, 205403.

[11] Kawasaki, S.; Matsuoka, Y.; Yokomae, T.; Nojima, Y.; Okino, F.; Touhara, H.; Kataura, H. Effect of a liquid pressure-transmitting medium on the high pressure behavior of open- and closed-end single-walled carbon nanotubes and of C_{60}-peapods. *Phys. Status Solidi B* **2004**, *241*, 3512–3516.

[12] Hernandez, E.; Meunier, V.; Smith, B.; Rurali, R.; Terrones, H.; Buongiorno Nardelli, M.; Terrones, M.; Luzzi, D. E.; Charlier, J.-C. Fullerene coalescence in nanopeapods: a path to novel tubular carbon. *Nano Lett.* **2003**, *3*, 1037–1042.

[13] Álvarez-Murga, M.; Hodeau, J. Structural phase transitions of C_{60} under high-pressure and high-temperature. *Carbon* **2015**, *82*, 381–407.

[14] Caillier, C.; Machon, D.; San-Miguel, A.; Arenal, R.; Montagnac, G.; Cardon, H.; Kalbac, M.; Zukalova, M.; Kavan, L. Probing high-pressure properties of single-wall carbon nanotubes through fullerene encapsulation. *Phys. Rev. B* **2008**, *77*, 125418.

[15] Torres-Dias, A. C.; Cambré, S.; Wenseleers, W.; Machon, D.; San-Miguel, A. Chirality-dependent mechanical response of empty and water-filled single-wall carbon nanotubes at high pressure. *Carbon* **2015**, *95*, 442–451.

[16] Cambré, S.; Schoeters, B.; Luyckx, S.; Goovaerts, E.; Wenseleers, W. Experimental observation of single-file water filling of thin single-wall carbon nanotubes down to chiral index (5, 3). *Phys. Rev. Lett.* **2010**, *104*, 207401.

[17] Maniwa, Y.; Kataura, H.; Abe, M.; Udaka, A.; Suzuki, S.; Achiba, Y.; Kira, H.; Matsuda, K.; Kadowaki, H.; Okabe, Y. Ordered water inside carbon nanotubes: formation of pentagonal to octagonal ice-nanotubes. *Chem. Phys. Lett.* **2005**, *401*, 534–538.

[18] Aguiar, A.; Barros, E.; Capaz, R.; Souza Filho, A.; Freire, P.; Filho, J. M.; Machon, D.; Caillier, C.; Kim, Y.; Muramatsu, H.; San-Miguel, A. Pressure-induced collapse in double-walled carbon nanotubes: chemical and mechanical screening effects. *J. Phys. Chem. C* **2011**, *115*, 5378–5384.

[19] You, S.; Mases, M.; Dobryden, I.; Green, A. A.; Hersam, M. C.; Soldatov, A. V. Probing structural stability of double-walled carbon nanotubes at high non-hydrostatic pressure by Raman spectroscopy. *High Pressure Res.* **2011**, *31*, 186–190.

[20] Byl, O.; Liu, J.-C.; Wang, Y.; Yim, W.-L.; Johnson, J. K.; Yates, J. T. Unusual hydrogen bonding in water-filled carbon nanotubes. *J. Am. Chem. Soc.* **2006**, *128*, 12090–12097.

[21] Koga, K.; Gao, G.; Tanaka, H.; Zeng, X. C. Formation of ordered ice nanotubes inside carbon nanotubes. *Nature* **2001**, *412*, 802–805.

[22] Noon, W. H.; Ausman, K. D.; Smalley, R. E.; Ma, J. Helical ice-sheets inside carbon nanotubes in the physiological condition. *Chem. Phys. Lett.* **2002**, *355*, 445–448.

[23] Sun, F.; Li, H. Torsional strain energy evolution of carbon nanotubes and their stability with encapsulated helical copper nanowires. *Carbon* **2011**, *49*, 1408–1415.

[24] Elliott, J. A.; Sandler, J. K. W.; Windle, A. H.; Young, R. J.; Shaffer, M. S. P. Collapse of Single-Wall Carbon Nanotubes is Diameter Dependent. *Phys. Rev. Lett.* **2004**, *92*, 095501.

[25] Charlier, J.-C.; Lambin, P.; Ebbesen, T. Electronic properties of carbon nanotubes with polygonized cross sections. *Phys. Rev. B* **1996**, *54*, R8377.

[26] Yin, Z.; Li, H.; Li, H.; Jiang, L.; Shi, Y.; Sun, Y.; Lu, G.; Zhang, Q.; Chen, X.; Zhang, H. Single-layer MoS_2 phototransistors. *ACS nano* **2011**, *6*, 74–80.

[27] Mak, K. F.; Lee, C.; Hone, J.; Shan, J.; Heinz, T. F. Atomically thin MoS_2: a new direct-gap semiconductor. *Phys. Rev. Lett.* **2010**, *105*, 136805.

[28] Splendiani, A.; Sun, L.; Zhang, Y.; Li, T.; Kim, J.; Chim, C.-Y.; Galli, G.; Wang, F. Emerging photoluminescence in monolayer MoS_2. *Nano Lett.* **2010**, *10*, 1271–1275.

[29] Geim, A. K.; Grigorieva, I. V. Van der Waals heterostructures. *Nature* **2013**, *499*, 419–425.

[30] Lee, Y.-H.; Zhang, X.-Q.; Zhang, W.; Chang, M.-T.; Lin, C.-T.; Chang, K.-D.; Yu, Y.-C.; Wang, J. T.-W.; Chang, C.-S.; Li, L.-J.; Others, Synthesis of Large-Area MoS_2 Atomic Layers with Chemical Vapor Deposition. *Adv. Mater.* **2012**, *24*, 2320–2325.

[31] Baugher, B. W.; Churchill, H. O.; Yang, Y.; Jarillo-Herrero, P. Intrinsic electronic transport properties of high-quality monolayer and bilayer MoS_2. *Nano Lett.* **2013**, *13*, 4212–4216.

[32] Iijima, S.; Ichihashi, T. Single-shell carbon nanotubes of 1-nm diameter. *Nature* **1993**,

[33] Hamada, N.; Sawada, S.-i.; Oshiyama, A. New one-dimensional conductors: graphitic microtubules. *Phys. Rev. Lett.* **1992**, *68*, 1579.

[34] Saito, R.; Fujita, M.; Dresselhaus, G.; Dresselhaus, u. M. Electronic structure of chiral graphene tubules. *Appl. Phys. Lett.* **1992**, *60*, 2204–2206.

[35] Wilder, J. W.; Venema, L. C.; Rinzler, A. G.; Smalley, R. E.; Dekker, C. Electronic structure of atomically resolved carbon nanotubes. *Nature* **1998**, *391*, 59–62.

[36] Odom, T. W.; Huang, J.-L.; Kim, P.; Lieber, C. M. Atomic structure and electronic properties of single-walled carbon nanotubes. *Nature* **1998**, *391*, 62–64.

[37] Olk, C. H.; Heremans, J. P. Scanning tunneling spectroscopy of carbon nanotubes. *J. Mater. Res.* **1994**, *9*, 259–262.

[38] Li, W.; Zhao, M.; Zhao, X.; Xia, Y.; Mu, Y. Hydrogen saturation stabilizes vacancy-induced ferromagnetic ordering in graphene. *Phys. Chem. Chem. Phys.* **2010**, *12*, 13699–13706.

[39] Maffucci, A.; Miano, G. Electrical Properties of Graphene for Interconnect Applications. *Appl. Sci.* **2014**, *4*, 305–317.

[40] Saito, R.; Dresselhaus, G.; Dresselhaus, M. S. *Physical properties of carbon nanotubes*; World scientific, 1998.

[41] Fuchs, J.-N.; Goerbig, M. O. Introduction to the physical properties of graphene. *Lect. Notes* **2008**,

[42] Franklin, A. D.; Luisier, M.; Han, S.-J.; Tulevski, G.; Breslin, C. M.; Gignac, L.; Lundstrom, M. S.; Haensch, W. Sub-10 nm carbon nanotube transistor. *Nano Lett.* **2012**, *12*, 758–762.

[43] Dubois, S.-M.; Zanolli, Z.; Declerck, X.; Charlier, J.-C. Electronic properties and quantum transport in Graphene-based nanostructures. *Eur. Phys. J. B* **2009**, *72*, 1–24.

[44] White, C.; Mintmire, J. Density of states reflects diameter in nanotubes. *Nature* **1998**, *394*, 29–30.

[45] Kim, P.; Odom, T. W.; Huang, J.-L.; Lieber, C. M. Electronic density of states of atomically resolved single-walled carbon nanotubes: Van Hove singularities and end states. *Phys. Rev. Lett.* **1999**, *82*, 1225.

[46] Yorikawa, H.; Muramatsu, S. Energy gaps of semiconducting nanotubules. *Phys. Rev. B* **1995**, *52*, 2723.

[47] Venema, L. C.; Wildöer, J. W.; Janssen, J. W.; Tans, S. J.; Tuinstra, H. L. T.; Kouwenhoven, L. P.; Dekker, C. Imaging electron wave functions of quantized energy levels in carbon nanotubes. *Science* **1999**, *283*, 52–55.

[48] Jorio, A.; Souza Filho, A.; Dresselhaus, G.; Dresselhaus, M.; Saito, R.; Hafner, J.; Lieber, C.; Matinaga, F.; Dantas, M.; Pimenta, M. Joint density of electronic states for one isolated single-wall carbon nanotube studied by resonant Raman scattering. *Phys. Rev. B* **2001**, *63*, 245416.

[49] O'connell, M. J.; Bachilo, S. M.; Huffman, C. B.; Moore, V. C.; Strano, M. S.; Haroz, E. H.; Rialon, K. L.; Boul, P. J.; Noon, W. H.; Kittrell, C.; Others, Band gap fluorescence from individual single-walled carbon nanotubes. *Science* **2002**, *297*, 593–596.

[50] Bachilo, S. M.; Strano, M. S.; Kittrell, C.; Hauge, R. H.; Smalley, R. E.; Weisman, R. B. Structure-assigned optical spectra of single-walled carbon nanotubes. *Science* **2002**, *298*, 2361–2366.

[51] Dresselhaus, M. S.; Dresselhaus, G.; Saito, R.; Jorio, A. Raman spectroscopy of carbon nanotubes. *Phys. Rep.* **2005**, *409*, 47–99.

[52] Popov, V.; Van Doren, V.; Balkanski, M. Elastic properties of single-walled carbon nanotubes. *Phys. Rev. B* **2000**, *61*, 3078.

[53] Dresselhaus, M.; Eklund, P. Phonons in carbon nanotubes. *Adv. Phys.*

[54] Nanot, S.; Thompson, N. A.; Kim, J.-H.; Wang, X.; Rice, W. D.; Hßroz, E. H.; Ganesan, Y.; Pint, C. L.; Kono, J. single-walled carbon nanotubes. In *Springer Handbook of Nanomaterials*; Springer, 2013; pp 105–146.

[55] Ferrari, A. C. Raman spectroscopy of graphene and graphite: disorder, electron–phonon coupling, doping and nonadiabatic effects. *Solid State Commun.* **2007**, *143*, 47–57.

[56] Rao, A.; Richter, E.; Bandow, S.; Chase, B.; Eklund, P.; Williams, K.; Fang, S.; Subbaswamy, K.; Menon, M.; Thess, A.; Others, Diameter-selective Raman scattering from vibrational modes in carbon nanotubes. *Science* **1997**, *275*, 187–191.

[57] Maultzsch, J.; Telg, H.; Reich, S.; Thomsen, C. Radial breathing mode of single-walled carbon nanotubes: Optical transition energies and chiral-index assignment. *Phys. Rev. B* **2005**, *72*, 205438.

[58] Dresselhaus, M.; Jorio, A.; Saito, R. Characterizing graphene, graphite, and carbon nanotubes by Raman spectroscopy. *Annu. Rev. Condens. Matter Phys.* **2010**, *1*, 89–108.

[59] Srivastava, D.; Wei, C.; Cho, K. Nanomechanics of carbon nanotubes and composites. *Appl. Mech. Rev.* **2003**, *56*, 215–230.

[60] Liu, C.; Fan, Y.; Liu, M.; Cong, H.; Cheng, H.; Dresselhaus, M. S. Hydrogen storage in single-walled carbon nanotubes at room temperature. *Science* **1999**, *286*, 1127–1129.

[61] Kong, J.; Franklin, N. R.; Zhou, C.; Chapline, M. G.; Peng, S.; Cho, K.; Dai, H. Nanotube molecular wires as chemical sensors. *science* **2000**, *287*, 622–625.

[62] Kim, P.; Lieber, C. M. Nanotube nanotweezers. *Science* **1999**, *286*, 2148–2150.

[63] San-Miguel, A. Nanomaterials under high-pressure. *Chem. Soc. Rev.* **2006**, *35*, 876–889.

[64] Hasegawa, M.; Nishidate, K. Radial deformation and stability of single-wall carbon nanotubes under hydrostatic pressure. *Phys. Rev. B* **2006**, *74*, 115401.

[65] Cerqueira, T. F.; Botti, S.; San-Miguel, A.; Marques, M. A. Density-functional tight-binding study of the collapse of carbon nanotubes under hydrostatic pressure. *Carbon* **2014**, *69*, 355–360.

[66] Elliott, J. A.; Sandler, J. K.; Windle, A. H.; Young, R. J.; Shaffer, M. S. Collapse of single-wall carbon nanotubes is diameter dependent. *Phys. Rev. Lett.* **2004**, *92*, 095501.

[67] Lammert, P. E.; Zhang, P.; Crespi, V. H. Gapping by squashing: Metal-insulator and insulator-metal transitions in collapsed carbon nanotubes. *Phys. Rev. Lett.* **2000**, *84*, 2453.

[68] Lu, J.-Q.; Wu, J.; Duan, W.; Liu, F.; Zhu, B.-F.; Gu, B.-L. Metal-to-semiconductor transition in squashed armchair carbon nanotubes. *Phys. Rev. Lett.* **2003**, *90*, 156601.

[69] Yang, L.; Han, J. Electronic structure of deformed carbon nanotubes. *Phys. Rev. Lett.* **2000**, *85*, 154.

[70] Gülseren, O.; Yildirim, T.; Ciraci, S.; Kılıç, Ç. Reversible band-gap engineering in carbon nanotubes by radial deformation. *Phys. Rev. B* **2002**, *65*, 155410.

[71] Tang, J.; Qin, L.-C.; Sasaki, T.; Yudasaka, M.; Matsushita, A.; Iijima, S. Compressibility and polygonization of single-walled carbon nanotubes under hydrostatic pressure. *Phys. Rev. Lett.* **2000**, *85*, 1887.

[72] Sharma, S. M.; Karmakar, S.; Sikka, S.; Teredesai, P. V.; Sood, A.; Govindaraj, A.; Rao, C. Pressure-induced phase transformation and structural resilience of single-wall carbon nanotube bundles. *Phys. Rev. B* **2001**, *63*, 205417.

[73] Motta, M.; Moisala, A.; Kinloch, I. A.; Windle, A. H. High Performance Fibres from "Dog Bone" Carbon Nanotubes. *Adv. Mater.* **2007**, *19*, 3721–3726.

[74] Venkateswaran, U.; Rao, A.; Richter, E.; Menon, M.; Rinzler, A.; Smalley, R.; Eklund, P. Probing the single-wall carbon nanotube bundle: Raman scattering under high pressure. *Phys. Rev. B* **1999**, *59*, 10928.

[75] Loa, I. Raman spectroscopy on carbon nanotubes at high pressure. *J. Raman Spectrosc.* **2003**, *34*, 611–627.

[76] San-Miguel, A.; Cailler, C.; Machon, D.; Barros, E. B.; Aguiar, A. L.; Souza Filho, A. G. Carbon nanotubes under high pressure probed by resonance raman scattering. In *High-Pressure Crystallography*; Springer, 2010; pp 435–446.

[77] Merlen, A.; Bendiab, N.; Toulemonde, P.; Aouizerat, A.; San Miguel, A.; Sauvajol, J. L.; Montagnac, G.; Cardon, H.; Petit, P. Resonant Raman spectroscopy of single-wall carbon nanotubes under pressure. *Phys. Rev. B* **2005**, *72*, 035409.

[78] Rols, S.; Goncharenko, I. N.; Almairac, R.; Sauvajol, J. L.; Mirebeau, I. Polygonization of single-wall carbon nanotube bundles under high pressure. *Phys. Rev. B* **2001**, *64*, 153401.

[79] Peters, M. J.; McNeil, L. E.; Lu, J. P.; Kahn, D. Structural phase transition in carbon nanotube bundles under pressure. *Phys. Rev. B* **2000**, *61*, 5939–5944.

[80] Yao, M.; Wang, Z.; Liu, B.; Zou, Y.; Yu, S.; Lin, W.; Hou, Y.; Pan, S.; Jin, M.; Zou, B.; Cui, T.; Zou, G.; Sundqvist, B. Raman signature to identify the structural transition of single-wall carbon nanotubes under high pressure. *Phys. Rev. B* **2008**, *78*, 205411.

[81] Aguiar, A.; San-Miguel, A.; Barros, E.; Kalbáč, M.; Machon, D.; Kim, Y.; Muramatsu, H.; Endo, M.; Souza Filho, A. Effects of intercalation and inhomogeneous filling on the collapse pressure of double-wall carbon nanotubes. *Phys. Rev. B* **2012**, *86*, 195410.

[82] Aguiar, A. L.; Capaz, R. B.; Souza Filho, A.; San-Miguel, A. Structural and phonon properties of bundled single-and double-wall carbon nanotubes under pressure. *J. Phys. Chem. C* **2012**, *116*, 22637–22645.

[83] Gadagkar, V.; Maiti, P. K.; Lansac, Y.; Jagota, A.; Sood, A. Collapse of double-walled carbon nanotube bundles under hydrostatic pressure. *Phys. Rev. B* **2006**, *73*, 085402.

[84] Ye, X.; Sun, D. Y.; Gong, X. G. Pressure-induced structural transition of double-walled carbon nanotubes. *Phys. Rev. B* **2005**, *72*, 035454.

[85] Mases, M.; Milyavskiy, V. V.; Waldbock, J.; Dossot, M.; Devaux, X.; McRae, E.; Soldatov, A. V. The effect of shock wave compression on double wall carbon nanotubes. *Phys. Status Solidi B* **2012**, *249*, 2378–2381.

[86] Alvarez, L.; Bantignies, J.-L.; Le Parc, R.; Aznar, R.; Sauvajol, J.-L.; Merlen, A.; Machon, D.; San Miguel, A. High-pressure behavior of polyiodides confined into single-walled carbon nanotubes: a Raman study. *Phys. Rev. B* **2010**, *82*, 205403.

[87] Szabo, A. NS Ostlund Modern quantum chemistry. *McMillan, New York* **1982**,

[88] Hohenberg, P.; Kohn, W. Inhomogeneous electron gas. *Phys. Rev.* **1964**, *136*, B864.

[89] Kohn, W.; Sham, L. J. Self-consistent equations including exchange and correlation effects. *Phys. Rev.* **1965**, *140*, A1133.

[90] Perdew, J. P.; Zunger, A. Self-interaction correction to density-functional approximations for many-electron systems. *Phys. Rev. B* **1981**, *23*, 5048.

[91] Dirac, P. A. Quantised singularities in the electromagnetic field. Proceedings of the Royal Society of London A: Mathematical, Physical and Engineering Sciences. 1931; pp 60–72.

[92] Ceperley, D. M.; Alder, B. Ground state of the electron gas by a stochastic method. *Phys. Rev. Lett.* **1980**, *45*, 566.

[93] Capelle, K. A bird's-eye view of density-functional theory. *Braz. J. Phys.* **2006**, *36*, 1318–1343.

[94] Gross, E. K.; Runge, E. Many-particle theory. **1986**,

[95] Perdew, J. P.; Burke, K.; Ernzerhof, M. Generalized gradient approximation made simple. *Phys. Rev. Lett.* **1996**, *77*, 3865.

[96] Becke, A. D. Density-functional exchange-energy approximation with correct asymptotic behavior. *Phys. Rev. A* **1988**, *38*, 3098.

[97] Hasnip, P. J.; Refson, K.; Probert, M. I.; Yates, J. R.; Clark, S. J.; Pickard, C. J. Density functional theory in the solid state. *Phil. Trans. R. Soc. A* **2014**, *372*, 20130270.

[98] Dion, M.; Rydberg, H.; Schröder, E.; Langreth, D. C.; Lundqvist, B. I. Van der Waals density functional for general geometries. *Phys. Rev. Lett.* **2004**, *92*, 246401.

[99] Rydberg, H.; Lundqvist, B. I.; Langreth, D. C.; Dion, M. Tractable nonlocal correlation density functionals for flat surfaces and slabs. *Phys. Rev. B* **2000**, *62*, 6997.

[100] Langreth, D. C.; Vosko, S. Response functions and nonlocal approximations. *Adv. Quantum Chem.* **1990**, *21*, 175–199.

[101] Klimeš, J.; Bowler, D. R.; Michaelides, A. Chemical accuracy for the van der Waals density functional. *J. Phys.: Condens. Matter* **2009**, *22*, 022201.

[102] Klimeš, J.; Bowler, D. R.; Michaelides, A. Van der Waals density functionals applied to solids. *Phys. Rev. B* **2011**, *83*, 195131.

[103] Thonhauser, T.; Cooper, V. R.; Li, S.; Puzder, A.; Hyldgaard, P.; Langreth, D. C. Van der Waals density functional: Self-consistent potential and the nature of the van der Waals bond. *Phys. Rev. B* **2007**, *76*, 125112.

[104] Román-Pérez, G.; Soler, J. M. Efficient implementation of a van der Waals density functional: application to double-wall carbon nanotubes. *Phys. Rev. Lett.* **2009**, *103*, 096102.

[105] Jurečka, P.; Šponer, J.; Černỳ, J.; Hobza, P. Benchmark database of accurate (MP2 and CCSD (T) complete basis set limit) interaction energies of small model complexes, DNA base pairs, and amino acid pairs. *Phys. Chem. Chem. Phys.* **2006**, *8*, 1985–1993.

[106] Porezag, D.; Frauenheim, T.; Köhler, T.; Seifert, G.; Kaschner, R. Construction of tight-binding-like potentials on the basis of density-functional theory: Application to carbon. *Phys. Rev. B* **1995**, *51*, 12947.

[107] Seifert, G.; Porezag, D.; Frauenheim, T. Calculations of molecules, clusters, and solids with a simplified LCAO-DFT-LDA scheme. *Int. J. Quantum Chem.* **1996**, *58*, 185–192.

[108] Elstner, M.; Porezag, D.; Jungnickel, G.; Elsner, J.; Haugk, M.; Frauenheim, T.; Suhai, S.; Seifert, G. Self-consistent-charge density-functional tight-binding method for simulations of complex materials properties. *Phys. Rev. B* **1998**, *58*, 7260.

[109] Koskinen, P.; Mäkinen, V. Density-functional tight-binding for beginners. *Comp. Mater. Sci.* **2009**, *47*, 237–253.

[110] Aradi, B.; Hourahine, B.; Frauenheim, T. DFTB+, a sparse matrix-based implementation of the DFTB method. *J. Phys. Chem. A* **2007**, *111*, 5678–5684.

[111] Kresse, G.; Furthmüller, J. Efficient iterative schemes for ab initio total-energy calculations using a plane-wave basis set. *Phys. Rev. B* **1996**, *54*, 11169.

[112] Zhang, M.; Li, J. Carbon nanotube in different shapes. *Mater. Today* **2009**, *12*, 12–18.

[113] Thess, A.; Lee, R.; Nikolaev, P.; Dai, H.; Petit, P.; Robert, J.; Xu, C.; Lee, Y. H.; Kim, S. G.; Rinzler, A. G. Crystalline ropes of metallic carbon nanotubes. *Science* **1996**, *273*, 483–487.

[114] Zang, J.; Treibergs, A.; Han, Y.; Liu, F. Geometric constant defining shape transitions of carbon nanotubes under pressure. *Phys. Rev. Lett.* **2004**, *92*, 105501.

[115] Thomsen, C.; Reich, S. Raman scattering in carbon nanotubes. In *Light Scattering in Solid IX*; Springer, 2007; pp 115–234.

[116] Mazzoni, M. S.; Chacham, H. Bandgap closure of a flattened semiconductor carbon nanotube: a first-principles study. *Appl. Phys. Lett.* **2000**, *76*, 1561–1563.

[117] Lammert, P. E.; Zhang, P.; Crespi, V. H. Gapping by Squashing: Metal-Insulator and Insulator-Metal Transitions in Collapsed Carbon Nanotubes. *Phys. Rev. Lett.* **2000**, *84*, 2453–2456.

[118] Charlier, A.; McRae, E.; Heyd, R.; Charlier, M.-F. Metal–semiconductor transitions under uniaxial stress for single-and double-walled carbon nanotubes. *J. Phys. Chem. Solids* **2001**, *62*, 439–444.

[119] Gülseren, O.; Yildirim, T.; Ciraci, S.; Kılıç, Ç. Reversible band-gap engineering in carbon nanotubes by radial deformation. *Phys. Rev.B* **2002**, *65*, 155410.

[120] Chen, D.; Sasaki, T.; Tang, J.; Qin, L.-C. Effects of deformation on the electronic structure of a single-walled carbon nanotube bundle. *Phys. Rev. B* **2008**, *77*, 125412.

[121] Giusca, C. E.; Tison, Y.; Silva, S. R. P. Evidence for Metal-Semiconductor Transitions in Twisted and Collapsed Double-Walled Carbon Nanotubes by Scanning Tunneling Microscopy. *Nano Lett.* **2008**, *8*, 3350–3356.

[122] Okuno, Y.; Saito, Y.; Kawata, S.; Verma, P. Tip-Enhanced Raman Investigation of Extremely Localized Semiconductor-to-Metal Transition of a Carbon Nanotube. *Phys. Rev. Lett.* **2013**, *111*, 216101.

[123] Blancon, J.-C.; Ayari, A.; Marty, L.; Bendiab, N.; San-Miguel, A. Electronic transport in individual carbon nanotube bundles under pressure. *J. Appl. Phys* **2013**, *114*, 143704.

[124] Hertel, T.; Walkup, R. E.; Avouris, P. Deformation of carbon nanotubes by surface van der Waals forces. *Phys. Rev. B* **1998**, *58*, 13870–13873.

[125] Blancon, J.-C.; Paillet, M.; Tran, H. N.; Than, X. T.; Guebrou, S. A.; Ayari, A.; Miguel, A. S.; Phan, N.-M.; Zahab, A.-A.; Sauvajol, J.-L.; Fatti, N. D.; Vallée, F. Direct measurement of the absolute absorption spectrum of individual semiconducting single-wall carbon nanotubes. *Nat. Commun.* **2013**, *4*.

[126] Soares, J. S. et al. Modulating the Electronic Properties along Carbon Nanotubes via Tube-Substrate Interaction. *Nano Lett.* **2010**, *10*, 5043–5048.

[127] Zheng, G.; Irle, S.; Morokuma, K. Performance of the DFTB method in comparison to DFT and semiempirical methods for geometries and energies of C_{20}-C_{60} fullerene isomers. *Chem. Phys. Lett.* **2005**, *412*, 210 – 216.

[128] Botti, S.; Amsler, M.; Flores-Livas, J. A.; Ceria, P.; Goedecker, S.; Marques, M. A. L. Carbon structures and defect planes in diamond at high pressure. *Phys. Rev. B* **2013**, *88*, 014102.

[129] Malola, S.; Häkkinen, H.; Koskinen, P. Raman spectra of single-walled carbon nanotubes with vacancies. *Phys. Rev. B* **2008**, *77*, 155412.

[130] Tang, W.; Advani, S. G. Drag on a nanotube in uniform liquid argon flow. *J. Chem. Phys.* **2006**, *125*, 174706.

[131] Cannon, J.; Kim, D.; Hess, O. The initial flow dynamics of light atoms through carbon nanotubes. *Fluid Dyn. Res.* **2011**, *43*, 025507.

[132] Tuzun, R. E.; Noid, D. W.; Sumpter, B. G.; Merkle, R. C. Dynamics of flow inside carbon nanotubes. *Nanotechnology* **1997**, *8*, 112.

[133] Liu, Y.-C.; Moore, J. D.; Roussel, T. J.; Gubbins, K. E. Dual diffusion mechanism of argon confined in single-walled carbon nanotube bundles. *Phys. Chem. Chem. Phys.* **2010**, *12*, 6632–6640.

[134] Ackerman, D. M.; Skoulidas, A. I.; Sholl, D. S.; Karl Johnson, J. Diffusivities of Ar and Ne in carbon nanotubes. *Mol. Simul.* **2003**, *29*, 677–684.

[135] Ling, C.-c.; Xue, Q.-z.; Xia, D.; Shan, M.-x.; Han, Z.-d. Fullerene filling modulates carbon nanotube radial elasticity and resistance to high pressure. *RSC Adv.* **2014**, *4*, 1107–1115.

[136] Algara-Siller, G.; Lehtinen, O.; Wang, F.; Nair, R.; Kaiser, U.; Wu, H.; Geim, A.; Grigorieva, I. Square ice in graphene nanocapillaries. *Nature* **2015**, *519*, 443–445.

[137] Benoit, M.; Bernasconi, M.; Focher, P.; Parrinello, M. New high-pressure phase of ice. *Phys. Rev. Lett.* **1996**, *76*, 2934.

[138] Gogotsi, Y.; Libera, J. A.; Güvenç-Yazicioglu, A.; Megaridis, C. M. In situ multiphase fluid experiments in hydrothermal carbon nanotubes. *Appl. Phys. Lett.* **2001**, *79*, 1021–1023.

[139] Gordillo, M.; Martı, J. Hydrogen bond structure of liquid water confined in nanotubes. *Chem. Phys. Lett.* **2000**, *329*, 341–345.

[140] Liu, Y.; Wilcox, J. CO_2 adsorption on carbon models of organic constituents of gas shale and coal. *Environ. Sci. Technol.* **2010**, *45*, 809–814.

[141] Liu, Y.; Wang, Q.; Wu, T.; Zhang, L. Fluid structure and transport properties of water inside carbon nanotubes. *J. Chem. Phys.* **2005**, *123*, 234701.

[142] Luzar, A.; Chandler, D. Hydrogen-bond kinetics in liquid water. *Nature* **1996**, *379*, 55–57.

[143] Mashl, R. J.; Joseph, S.; Aluru, N.; Jakobsson, E. Anomalously immobilized water: a new water phase induced by confinement in nanotubes. *Nano Lett.* **2003**, *3*, 589–592.

[144] Quintilla, A.; Hennrich, F.; Lebedkin, S.; Kappes, M. M.; Wenzel, W. Influence of endohedral water on diameter sorting of single-walled carbon nanotubes by density gradient centrifugation. *Phys. Chem. Chem. Phys.* **2010**, *12*, 902–908.

[145] Rivera, J. L.; Starr, F. W. Rapid transport of water via a carbon nanotube syringe. *J. Phys. Chem. C* **2010**, *114*, 3737–3742.

[146] Singh, S. K.; Saha, A. K.; Singh, J. K. *J. Phys. Chem. B* **2010**, *114*, 4283–4292.

[147] Wang, J.; Zhu, Y.; Zhou, J.; Lu, X.-H. Diameter and helicity effects on static properties of water molecules confined in carbon nanotubes. *Phys. Chem. Chem. Phys.* **2004**, *6*, 829–835.

[148] Wang, L.; Zhao, J.; Li, F.; Fang, H.; Lu, J. P. First-principles study of water chains encapsulated in single-walled carbon nanotube. *J. Phys. Chem. C* **2009**, *113*, 5368–5375.

[149] Yim, W.-L.; Byl, O.; Yates Jr, J. T.; Johnson, J. K. Vibrational behavior of adsorbed CO_2 on single-walled carbon nanotubes. *J. Chem. Phys.* **2004**, *120*, 5377–5386.

[150] Alexiadis, A.; Kassinos, S. The density of water in carbon nanotubes. *Chem. Eng. Sci.* **2008**, *63*, 2047–2056.

[151] Chorro, M.; Cambedouzou, J.; Iwasiewicz-Wabnig, A.; Noé, L.; Rols, S.; Monthioux, M.; Sundqvist, B.; Launois, P. Discriminated structural behaviour of C_{60} and C_{70} peapods under extreme conditions. *Europhys. Lett.* **2007**, *79*, 56003.

[152] Alexiadis, A.; Kassinos, S. Molecular simulation of water in carbon nanotubes. *Chem. Rev.* **2008**, *108*, 5014–5034, and references therein.

[153] Shiomi, J.; Kimura, T.; Maruyama, S. Molecular dynamics of ice-nanotube formation inside carbon nanotubes. *J. Phys. Chem. C* **2007**, *111*, 12188–12193.

[154] Paineau, E.; Albouy, P.-A.; Rouzière, S.; Orecchini, A.; Rols, S.; Launois, P. X-ray scattering determination of the structure of water during carbon nanotube filling. *Nano Lett.* **2013**, *13*, 1751–1756, and references therein.

[155] Zhou, W.; Yin, K.; Wang, C.; Zhang, Y.; Xu, T.; Borisevich, A.; Sun, L.; Idrobo, J. C.; Chisholm, M. F.; Pantelides, S. T.; Others, The observation of square ice in graphene questioned. *Nature* **2015**, *528*, E1–E2.

[156] Frenzel, J.; Oliveira, A. F.; Duarte, H. A.; Heine, T.; Seifert, G. Structural and electronic properties of bulk gibbsite and gibbsite surfaces. *Z. Anorg. Allg. Chem* **2005**, *631*, 1267–1271.

[157] Peralta-Inga, Z.; Boyd, S.; Murray, J. S.; O'Connor, C. J.; Politzer, P. Density functional tight-binding studies of carbon nanotube structures. *Struct. Chem.* **2003**, *14*, 431–443.

[158] Goyal, P.; Elstner, M.; Cui, Q. Application of the SCC-DFTB method to neutral and protonated water clusters and bulk water. *J. Phys. Chem. B* **2011**, *115*, 6790–6805.

[159] Jahangiri, S.; Cai, L.; Peslherbe, G. H. Performance of density-functional tight-binding models in describing hydrogen-bonded anionic-water clusters. *J. Comput. Chem.* **2014**, *35*, 1707–1715.

[160] Wei, C.; Srivastava, D.; Cho, K. Molecular dynamics study of temperature dependent plastic collapse of carbon nanotubes under axial compression. *Comput. Modeling Engrg. Sci* **2002**, *3*, 255–261.

[161] Arvanitidis, J.; Christofilos, D.; Papagelis, K.; Andrikopoulos, K.; Takenobu, T.; Iwasa, Y.; Kataura, H.; Ves, S.; Kourouklis, G. Pressure screening in the interior of primary shells in double-wall carbon nanotubes. *Phys. Rev. B* **2005**, *71*, 125404.

[162] Merlen, A.; Toulemonde, P.; Bendiab, N.; Aouizerat, A.; Sauvajol, J.-L.; Montagnac, G.; Cardon, H.; Petit, P.; San Miguel, A. Raman spectroscopy of open-ended Single Wall Carbon Nanotubes under pressure: effect of the pressure transmitting medium. *Phys. Status Solidi B* **2006**, *243*, 690–699.

[163] Chopra, N. G.; Benedict, L. X.; Crespi, V. H.; Cohen, M. L.; Louie, S. G.; Zettl, A. Fully collapsed carbon nanotubes. *Nature* **1995**, *377*, 135–138.

[164] Torres-Dias, A.; Cerqueira, T. F. T.; Cambie, S.; Marques, M.; Botti, S.; Wenseleers, W.; Machon, D.; Hartmann, M. A.; Sun, Y. W.; Dunstan, D.; San-Miguel, A. From mesoscale to nanoscale mechanics in single-wall carbon nanotubes. *Carbon* **2017**, *XX*.

[165] Lévy, M. Mémoire sur un nouveau cas intégrable du probleme de l'élastique et l'une de ses applications. *Journal de Mathématiques Pures et Appliquées* **1884**, *3*, 5–42.

[166] Carman, A. P. Resistance of Tubes to Collapse. *Phys. Rev.* **1905**, *XXI*, 381–387.

[167] Cui, W.; Cerqueira, T. F.; Botti, S.; Marques, M. A.; San-Miguel, A. Nanostructured water and carbon dioxide inside collapsing carbon nanotubes at high pressure. *Phys. Chem. Chem. Phys.* **2016**, *18*, 19926–19932.

[168] Aguiar, A. L.; Barros, E. B.; Capaz, R. B.; Souza Filho, A. G.; Freire, P. T. C.; Mendes Filho, J.; Machon, D.; Caillier, C.; Kim, Y. A.; Muramatsu, H.; Endo, M.; San-Miguel, A. Pressure-Induced Collapse in Double-Walled Carbon Nanotubes: Chemical and Mechanical Screening Effects. *J. Phys. Chem. C* **2011**, *115*, 5378–5384.

[169] Puech, P.; Hubel, H.; Dunstan, D. J.; Bacsa, R. R.; Laurent, C.; Bacsa, W. S. Discontinuous Tangential Stress in Double Wall Carbon Nanotubes. *Phys. Rev. Lett.* **2004**, *93*, 095506.

[170] Yang, X.; Wu, G.; Dong, J. Structural transformations of double-walled carbon nanotube bundle under hydrostatic pressure. *Appl. Phys. Lett.* **2006**, *89*, 113101.

[171] Puech, P.; Hubel, H.; Dunstan, D.; Bassil, A.; Bacsa, R.; Peigney, A.; Flahaut, E.; Laurent, C.; Bacsa, W. Light scattering of double wall carbon nanotubes under hydrostatic pressure: pressure effects on the internal and external tubes. *Phys. Status Solidi B* **2004**, *241*, 3360–3366.

[172] del Corro, E.; González, J.; Taravillo, M.; Flahaut, E.; Baonza, V. G. Raman Spectra of Double-Wall Carbon Nanotubes under Extreme Uniaxial Stress. *Nano Lett.* **2008**, *8*, 2215–2218.

[173] Aguiar, A. L.; Capaz, R. B.; Souza Filho, A. G.; San-Miguel, A. Structural and Phonon Properties of Bundled Single- and Double-Wall Carbon Nanotubes Under Pressure. *J. Phys. Chem. C* **2012**, *116*, 22637–22645.

[174] Anis, B.; Haubner, K.; Börrnert, F.; Dunsch, L.; Rümmeli, M. H.; Kuntscher, C. A. Stabilization of carbon nanotubes by filling with inner tubes: An optical spectroscopy study on double-walled carbon nanotubes under hydrostatic pressure. *Phys. Rev. B* 155454.

[175] Frenzel, J.; Oliveira, A. F.; Jardillier, N.; Heine, T.; Seifert, G. Semi-relativistic, self-consistent charge Slater-Koster tables for density-functional based tight-binding (DFTB) for materials science simulations. 2004–2009.

[176] Flahaut, E.; Laurent, C.; Peigney, A. Catalytic {CVD} synthesis of double and triple-walled carbon nanotubes by the control of the catalyst preparation. *Carbon* **2005**, *43*, 375–383.

[177] Mao, H.; Xu, J.; Bell, P. Calibration of the ruby pressure gauge to 800-kbar under quasi-hydrostatic conditions. *J. Geophys. Res.* **1986**, *91*, 4673–4676.

[178] Zang, J.; Treibergs, A.; Han, Y.; Liu, F. Geometric Constant Defining Shape Transitions of Carbon Nanotubes under Pressure. *Phys. Rev. Lett.* **2004**, *92*, 105501.

[179] Djondjorov, P.; Vassilev, V.; Mladenov, I. Analytic description and explicit parametrisation of the equilibrium shapes of elastic rings and tubes under uniform hydrostatic pressure. *Int. J. Mech. Sci* **2011**, *53*, 355–364.

[180] Vassilev, V.; Djondjorov, P.; Mladenov, I. Comment on "Shape transition of unstrained flattest single-walled carbon nanotubes under pressure" [J. Appl. Phys. 115, 044512 (2014)]. *J. Appl. Phys.* **2015**, *117*, 196101.

[181] Cassabois, G.; Valvin, P.; Gil, B. Hexagonal boron nitride is an indirect bandgap semiconductor. *Nat. Photonics* **2016**, *10*.

[182] Radisavljevic, B.; Radenovic, A.; Brivio, J.; Giacometti, i. V.; Kis, A. Single-layer MoS_2 transistors. *Nat. Nanotechnol.* **2011**, *6*, 147–150.

[183] Ross, J. S.; Klement, P.; Jones, A. M.; Ghimire, N. J.; Yan, J.; Mandrus, D.; Taniguchi, T.; Watanabe, K.; Kitamura, K.; Yao, W.; Others, Electrically tunable excitonic light-emitting diodes based on monolayer WSe_2 pn junctions. *Nat. Nanotechnol.* **2014**, *9*, 268–272.

[184] Cao, T.; Wang, G.; Han, W.; Ye, H.; Zhu, C.; Shi, J.; Niu, Q.; Tan, P.; Wang, E.; Liu, B.; Others, Valley-selective circular dichroism of monolayer molybdenum disulphide. *Nat. Commun.* **2012**, *3*, 887.

[185] Mak, K. F.; He, K.; Shan, J.; Heinz, T. F. Control of valley polarization in monolayer MoS_2 by optical helicity. *Nat. Nanotechnol.* **2012**, *7*, 494–498.

[186] Yun, W. S.; Lee, J. Strain-Induced Magnetism in Single-Layer MoS_2: Origin and Manipulation. *J. Phys. Chem. C* **2015**, *119*, 2822–2827.

[187] Tao, P.; Guo, H.; Yang, T.; Zhang, Z. Strain-induced magnetism in MoS_2 monolayer with defects. *J. Appl. Phys.* **2014**, *115*, 054305.

[188] Zheng, H.; Yang, B.; Wang, H.; Chen, Z.; Yan, Y. Strain induced modulation to the magnetism of antisite defects doped monolayer MoS_2. *J. Magn. Magn. Mater.* **2015**, *386*, 155–160.

[189] Cheng, Y.; Zhu, Z.; Mi, W.; Guo, Z.; Schwingenschlögl, U. Prediction of two-dimensional diluted magnetic semiconductors: doped monolayer MoS_2 systems. *Phys. Rev. B* **2013**, *87*, 100401.

[190] Liu, H.; Neal, A. T.; Ye, P. D. Channel length scaling of MoS_2 MOSFETs. *ACS nano* **2012**, *6*, 8563–8569.

[191] Das, S.; Chen, H.-Y.; Penumatcha, A. V.; Appenzeller, J. High performance multilayer MoS_2 transistors with scandium contacts. *Nano Lett.* **2012**, *13*, 100–105.

[192] Chen, J.-R.; Odenthal, P. M.; Swartz, A. G.; Floyd, G. C.; Wen, H.; Luo, K. Y.; Kawakami, R. K. Control of Schottky barriers in single layer MoS_2 transistors with ferromagnetic contacts. *Nano Lett.* **2013**, *13*, 3106–3110.

[193] Tosun, M.; Fu, D.; Desai, S. B.; Ko, C.; Kang, J. S.; Lien, D.-H.; Najmzadeh, M.; Tongay, S.; Wu, J.; Javey, A. MoS_2 Heterojunctions by Thickness Modulation. *Sci. Rep.* **2015**, *5*.

[194] Kaushik, N.; Nipane, A.; Basheer, F.; Dubey, S.; Grover, S.; Deshmukh, M. M.; Lodha, S. Schottky barrier heights for Au and Pd contacts to MoS_2. *Appl. Phys. Lett.* **2014**, *105*, 113505.

[195] Kang, J.; Liu, W.; Banerjee, K. High-performance MoS_2 transistors with low-resistance molybdenum contacts. *Appl. Phys. Lett.* **2014**, *104*, 093106.

[196] Popov, I.; Seifert, G.; Tománek, D. Designing electrical contacts to MoS_2 monolayers: a computational study. *Phys. Rev. Lett.* **2012**, *108*, 156802.

[197] Liu, W.; Kang, J.; Sarkar, D.; Khatami, Y.; Jena, D.; Banerjee, K. Role of metal contacts in designing high-performance monolayer n-type WSe_2 field effect transistors. *Nano Lett.* **2013**, *13*, 1983–1990.

[198] Fang, H.; Chuang, S.; Chang, T. C.; Takei, K.; Takahashi, T.; Javey, A. High-performance single layered WSe_2 p-FETs with chemically doped contacts. *Nano Lett.* **2012**, *12*, 3788–3792.

[199] Gan, L.-Y.; Zhao, Y.-J.; Huang, D.; Schwingenschlögl, U. First-principles analysis of MoS_2/Ti_2C and MoS_2/Ti_2CY_2 (Y= F and OH) all-2D semiconductor/metal contacts. *Phys. Rev. B* **2013**, *87*, 245307.

[200] Kang, J.; Liu, W.; Sarkar, D.; Jena, D.; Banerjee, K. Computational study of metal contacts to monolayer transition-metal dichalcogenide semiconductors. *Phys. Rev. X* **2014**, *4*, 031005.

[201] Feng, N.; Mi, W.; Cheng, Y.; Guo, Z.; Schwingenschlogl, U.; Bai, H. Magnetism by interfacial hybridization and p-type doping of MoS_2 in Fe_4N/MoS_2 superlattices: a first-principles study. *ACS Appl. Mater. Interfaces* **2014**, *6*, 4587–4594.

[202] Zhang, X.; Mi, W.; Wang, X.; Cheng, Y.; Schwingenschlögl, U. The interface between Gd and Monolayer MoS_2: a first-principles study. *Sci. Rep.* **2014**, *4*, 7368.

[203] Weser, M.; Rehder, Y.; Horn, K.; Sicot, M.; Fonin, M.; Preobrajenski, A. B.; Voloshina, E. N.; Goering, E.; Dedkov, Y. S. Induced magnetism of carbon atoms at the graphene/Ni (111) interface. *Appl. Phys. Lett.* **2010**, *96*, 012504.

[204] Sawada, K.; Ishii, F.; Saito, M. Magnetism in graphene nanoribbons on Ni (111): first-principles density functional study. *Phys. Rev. B* **2010**, *82*, 245426.

[205] Zhang, W.-B.; Chen, C.; Tang, P.-Y. First-principles study for stability and binding mechanism of graphene/Ni (111) interface: Role of vdW interaction. *J. Chem. Phys.* **2014**, *141*, 044708.

[206] Zhong, H.; Ni, Z.; Wang, Y.; Ye, M.; Song, Z.; Pan, Y.; Quhe, R.; Yang, J.; Yang, L.; Shi, J.; Others, Interfacial Properties of Monolayer and Bilayer MoS_2 Contacts with Metals: Beyond the Energy Band Calculations. *Sci. Rep.* **2016**, *6*, 21786.

[207] Farmanbar, M.; Brocks, G. First-principles study of van der Waals interactions and lattice mismatch at MoS_2/metal interfaces. *Phys. Rev. B* **2016**, *93*, 085304.

[208] Blöchl, P. E. Projector augmented-wave method. *Phys. Rev. B* **1994**, *50*, 17953.

[209] Kresse, G.; Joubert, D. From ultrasoft pseudopotentials to the projector augmented-wave method. *Phys. Rev. B* **1999**, *59*, 1758.

[210] Liu, K.; Zhang, L.; Cao, T.; Jin, C.; Qiu, D.; Zhou, Q.; Zettl, A.; Yang, P.; Louie, S. G.; Wang, F. Evolution of interlayer coupling in twisted molybdenum disulfide bilayers. *Nat. Commun.* **2014**, *5*.

[211] Bader, R. F. *Atoms in molecules*; Wiley Online Library, 1990.

[212] Vogel, J.; Sacchi, M. Polarization and angular dependence of the $L_{2,3}$ absorption edges in Ni (110). *Phys. Rev. B* **1994**, *49*, 3230.

[213] Farmanbar, M.; Brocks, G. Controlling the Schottky barrier at MoS_2/metal contacts by inserting a BN monolayer. *Phys. Rev. B* **2015**, *91*, 161304.

[214] Leong, W. S.; Luo, X.; Li, Y.; Khoo, K. H.; Quek, S. Y.; Thong, J. T. Low resistance metal contacts to MoS_2 devices with nickel-etched-graphene electrodes. *ACS nano* **2014**, *9*, 869–877.

[215] Das, S.; Appenzeller, J. Where does the current flow in two-dimensional layered systems? *Nano Lett.* **2013**, *13*, 3396–3402.